Microstructural and Magnetic Properties of Polycrystalline and Epitaxial Permalloy ($Ni_{80}Fe_{20}$) Multilayered Thin Films

Thesis by

Imran Hashim

In Partial Fulfillment of the Requirements

for the Degree of Doctor of Philosophy

California Institute of Technology

Pasadena, California

1994

(Defended May 19, 1994)

Acknowledgments

It would be extremely difficult for me to give due credit to all the stimulating people I have come across during the course of my graduate studies at Caltech. I feel I have benefited enormously from interaction with various members of the Caltech community, which range from my undergrad students from A.Ph.9 to lab technicians and machinists, fellow graduate students and of course, members of the faculty.

The energy and enthusiasm for science of the Caltech undergrads in A.Ph.9, the Solid State Electronics Lab, which I was a TA for, was infectious. Also, I enjoyed working with the undergraduates who worked in our research group, especially Wurzel Keir who wrote the software for data acquisition of my experiment. I would also like to thank Carol Garland for teaching me the operation of electron microscopes, TEM sample preparation, and the importance of being honest and responsible when working in a multiuser lab facility. It's also a pleasure to acknowledge Joe Fontana, the machinist in Keck, who helped me enormously with machining and design of various parts of my experiment. Without his help, my experiment would not have survived a day. I would also like to acknowledge Reynold Johnson, the technician for A.Ph.9 lab, for teaching me how to maintain a sense of humor when things in lab are not going your way. I would also like to acknowledge the secretary for our research group, Rosalie Rowe, for being extremely helpful and patient while helping me out with various paperwork. Also, it is a pleasure to acknowledge Paula Samazan, the librarian of Electrical Engineering and Applied Physics, for technical assistance with library research

as well as always providing a welcome break from work by lending advice on all sorts of worldly matters. Thanks, Paula!

I also enjoyed enormously interaction with various Research Fellows in our research group, including Winston Saunders, Channing Ahn, Shouleh Nikzad, Byungwoo Park and Hyun Sung Joo, who taught me how much fun scientific research can be. I would also like to thank Ruth Brain, Renato Camata, Heather Frase, Gang He, Ramana Murty, Kirill Schgelov, Pete Sercel, Jung Shin, Maggie Taylor, Cho-Jen Tsai, Selmer Wong, and Jimmy Yang, for providing companionship and help during the course of my graduate career (especially Selmer for proofreading the thesis and reminding me of all the punctuation and grammar rules that I had forgotten, and Ramana Murty for help with AFM measurements). I would like to thank Tab Stephens for helping me setup the Inel power supply for small angle x-ray diffractometer. I would like to thank Jason Reid and Donald Lie for introducing me to "friendly" GSC basketball as well as help with backscattering and channeling. I would also like to thank Bruce Gurney of IBM Almaden Research Center for warning me of the perils I would encounter while setting up the magneto-optic Kerr system and also for making magnetostriction measurements for some of my samples. I would also like to acknowledge Romney Katti of Jet Propulsion Laboratory for introducing me to magnetism as applied to magnetic recording.

I would like to thank Prof. Fultz for introducing me to diffraction from materials, especially x-ray diffraction, Prof. Nicolet for teaching me backscattering spectrometry and workings of semiconductor devices, and Prof. Corngold for making the subject of statistical mechanics and thermodynamics

most interesting as well as intriguing. Finally, I would like to thank my research advisor, Prof. Atwater, for being a great friend, counselor and mentor at the same time. Not only did I learn most of what I know about electronic materials and thin film microstructure from him, but he also taught me how to be innovative in scientific research, how to communicate scientific results more effectively, and the hookshot in basketball which I'm still working on. He always seemed to have time to talk to me whether it was related to research, instrumentation, problems in my personal life or job search. It was a great pleasure to work under his supervision. Thanks, Harry!

Last but not least, I would like to acknowledge my parents for their support and patience during the course of my thesis. I would not have been here at Caltech if not for the attention they paid to my education all my life.

Abstract

Permalloy ($Ni_{80}Fe_{20}$) thin films are of great scientific and technological interest because of their unique soft magnetic properties, and applications to magnetic recording. Chapter 1 provides an introduction to magnetic and magnetotransport properties of $Ni_{80}Fe_{20}$ thin films, and how the film microstructure affects these properties. Chapter 2 discusses the instrumentation used for thin film fabrication, and for magnetic and structural characterization. Further details of instrumentation are discussed in Appendix A.

Typically, the $Ni_{80}Fe_{20}$ films for magnetoresistive applications are capped with a refractory metal thin film such as Ta to prevent its oxidation and corrosion. We investigated the interdiffusion kinetics of polycrystalline $Ta/Ni_{80}Fe_{20}$ thin films and found that for $400 \leq T \leq 600°C$, there was significant grain-boundary interdiffusion which drastically affected soft magnetic properties of $Ni_{80}Fe_{20}$. In Chapter 3, we present details of the microstructural evolution of these multilayers and the subsequent effects on their magnetic properties.

An alternate method for reducing grain-boundary scattering would be to fabricate grain-boundary free epitaxial $Ni_{80}Fe_{20}$ films. The epitaxy of $Ni_{80}Fe_{20}$ on MgO, NaCl and Cu had been demonstrated by investigators as early as the 60s. However, none of these substrates are available with as good atomic flatness as Si wafers. Following reports of epitaxial growth of Cu on Si[1], we proposed using it as a seed layer for growing $Ni_{80}Fe_{20}$ epitaxially on Si. However, there were conflicting reports of Cu epitaxy on Si, as some investigators claimed that Cu epitaxy on Si in UHV was not possible[2]. We were able to resolve some of these controversies (see Chapter 4 for details)

and thus fabricate epitaxial $Ni_{80}Fe_{20}$ films on Cu/Si.

Chapter 5 examines the effect of the lattice mismatch between Cu and $Ni_{80}Fe_{20}$ and the subsequent strain, on the soft magnetic properties of $Ni_{80}Fe_{20}$. To explain these experimentally observed magnetic properties, a micromagnetic model was developed taking into account domain wall interaction with misfit dislocations and film surface roughness especially during the initial stages of epitaxial growth. Finally, epitaxial growth of $Ni_{80}Fe_{20}$/Cu on Si suggests the possibility of growing grain-boundary free atomically sharp $Ni_{80}Fe_{20}$/Cu multilayers which exhibit recently-discovered "giant" magnetoresistance.

[1] C.A. Chang, Appl. Phys. Lett. **55**, 2754 (1989).

[2] B.P. Tonner, J. Zhang, X. Chen, Z-L. Han, G.R. Harp, and D.K. Saldin, J. Vac. Sci. Technol. **B10**, 2082 (1992).

List of Publications

Parts of this thesis have been, or will be published under the following titles.

1. "Interdiffusion Kinetics and Magnetic Properties of Ta-Permalloy Multilayers," I. Hashim, H.A. Atwater, K.T.Y. Kung, and R.M. Valletta, Mat. Res. Soc. Proc. Vol. **232**, 1991.
2. "Evolution of Structural and Magnetic Properties of Ta-$Ni_{80}Fe_{20}$ Multilayer Thin Films," I. Hashim, H.A. Atwater, K.T.Y. Kung, and R.M. Valletta, J. Appl. Phys. **77**, 458 (1993).
3. "Orientational and Microstructural Evolution During Epitaxy of Cu on Si(100)," I. Hashim, B. Park, and H.A. Atwater, Mat. Res. Soc. Proc. Vol. **280**, 1992.
4. "Epitaxial Growth of Cu(001) on Si(001): Mechanisms and Defect Morphology," I. Hashim, B. Park, and H.A. Atwater, Appl. Phys. Lett. **63**, 2833, 1993.
5. "*In situ* Analysis of Structural and Magnetic Properties of Epitaxial and Polycrystalline $Ni_{80}Fe_{20}$ Thin Films," I. Hashim and H.A. Atwater, Mat. Res. Soc. Proc. Vol. **313**, 1993.
6. "Epitaxial $Ni_{80}Fe_{20}$/Cu Films for Spin-Valve Heterostructures," I. Hashim and H.A. Atwater, J. Appl. Phys. **75**, 6516 (1994).
7. "Magnetoresistance of Epitaxial NiFe/Cu Spin-Valve Heterostructures," H.S. Joo, I. Hashim, and H.A. Atwater, in preparation.

Contents

List of Figures

List of Tables

Chapter 1

Introduction

1.1 Introduction to Soft Magnetic Materials

Humans have been fascinated with magnetic materials since "ancient times" when the ore magnetite was first discovered. The name of the ore, and hence that of the whole science of magnetism, is said to be derived from the Greek province of Magnesia in Thessaly, where magnetite was found as a natural mineral[1]. The wide variety of magnetic materials can be sharply divided into two categories, the magnetically soft (easy to magnetize and demagnetize) and the magnetically hard (hard to magnetize and demagnetize). The former category is distinguished by high permeability and low saturating fields, and typically find applications as core materials for transformers and magnetic recording heads. On the other hand, the figure of merit for hard magnetic materials is high coercivity, which is the field required to reduce the magnetization to zero, so as to be able to resist the demagnetization action of stray fields as well as its own. Hard magnetic materials are used as permanent magnets and also as the medium for information storage.

The last few decades have witnessed enormous progress in engineering the microstructure of magnetic materials for appropriate applications. The coercivity H_c spans an enormous range varying from a few tenths of an Oersted for 78 Permalloy ($Ni_{78}Fe_{22}$) to 24,000 Oersteds for SmCo. A famous example of control of magnetic properties through microstructure is soft Fe-3%Si used in tranformer cores, whose coercivity was reduced by two orders of magnitude by control of its microstructure. In 1900, some investigators stumbled upon the fact that the addition of 3% Si to Fe increases its electrical resistance and reduced its coercivity, making it suitable for use in transformer cores[1]. Further progress was made in the 1930s when it was discovered that cold-rolling and annealing yielded (100)-textured sheets which had lower coercivity. Even lower H_c was obtained in the 1970s by having the sheets made of large-grained (100)-oriented Fe-Si. As a consequence, there were fewer defects in the material and its magnetic properties approached those of single-crystal (100) Fe whiskers[2]. In soft magnetic materials, defects act as pinning sites for domain walls, and cause higher coercivity[3].

Another extremely important soft magnetic material is Permalloy ($Ni_{80}Fe_{20}$) which is used in magnetic recording heads because of its high permeability and low coercivity. Also, because of its magnetoresistance (change in resistance upon application of a magnetic field[4]) at low fields, it has been the material of choice in magnetoresistive sensors. Some of the relevant magnetic and magnetotransport properties of $Ni_{80}Fe_{20}$ are reviewed in the next section.

1.2 Magnetic and Magnetotransport Properties of $Ni_{80}Fe_{20}$

Of all the soft magnetic materials, $Ni_{80}Fe_{20}$, also known as Permalloy, is probably the most widely studied. This is owing to the fact that for this composition of Ni and Fe, the magnetocrystalline anisotropy and the magnetostriction are near zero[3]. Magnetocrystalline anisotropy refers to the fact that for a a single crystal ferromagnetic material, the path to magnetic saturation in a magnetic field is not the same along different crystallographic directions. Thus, Ni saturates most easily along $< 111 >$ directions whereas for Fe, $< 100 >$ are the easy axes. However, for $Ni_{80}Fe_{20}$, the magnetocrystalline anisotropy energy E_k reduces to 3×10^3 ergs/cm^3 as compared to $\sim 10^5$ ergs/cm^3 for elemental Ni and Fe[3]. Similarly, the magnetostriction (which is the fractional change $\Delta L/L$ in the dimensions of a magnetic sample when it is fully magnetized) for Ni and Fe is typically 10^{-5}, whereas for NiFe alloys, it is in the range 10^{-6}, and goes to zero near the composition 81-19[3, 5]. As a consequence, around this composition, the magnetic properties of NiFe alloys are relatively insensitive to stress. The fundamental origin of both magnetocrystalline anisotropy and magnetostriction is due to spin-orbit coupling[3] (see Chapter 5 for more discussion on magnetostriction in thin films). Hence, it is not surprising that both of them vary in an analogous fashion with NiFe composition.

As a consequence of the above properties, Permalloy has a relatively high permeablity (hence the name) and is easy to magnetize. Furthermore, even though it is a random face-centered cubic substitutional alloy, it can

possess directional order amongst nearest neighbors due to the interaction of different magnetic moments of Ni and Fe with the external field present during deposition[6]. Directional order implies a preferred orientation of the axes of like-atom pairs[3]. Usually, an external field of $\geq$ 20 Oe is sufficient to induce this directional order[7]. This results in a uniaxial anisotropy such that along one axis (*easy* axis) the hysteresis loop is square whereas along an orthogonal axis (*hard* axis), the magnetization is almost linear and has very little coercivity. Figure 1.1 shows typical Kerr hysteresis loops along easy and hard axes for a 20.0 nm thick $Ni_{80}Fe_{20}$ film deposited on SiO_2/Si. The coercivity for random polycrystalline films along hard and easy axes is typically $\sim$ 0.1 and $\sim$ 1 Oe respectively, whereas the uniaxial anisotropy H_k is $\sim$ 5 Oe. In general, the above parameters, coercivity in particular, depend sensitively on sample cleanliness and film deposition conditions[7].

NiFe alloys and thin films are also of interest because they exhibit anisotropic magnetoresistance (AMR)[4] which is different from the Hall effect magnetoresistance exhibited by most nonferromagnetic materials. The latter is caused by the deflection of the conduction electrons or holes in a solid by the Lorentz force due to an applied magnetic field. On the other hand, most ferromagnetic materials have different resistivities $\rho_{||}$ or $\rho_{\perp}$ depending upon whether the current $\vec{J}$ is parallel or perpendicular to the magnetization $\vec{M}$ of the material. Thus, when the magnetization vector of a ferromagnetic material is rotated as a single domain with respect to $\vec{J}$, there will be a change in the voltage drop across the sample due to the change in resistivity,

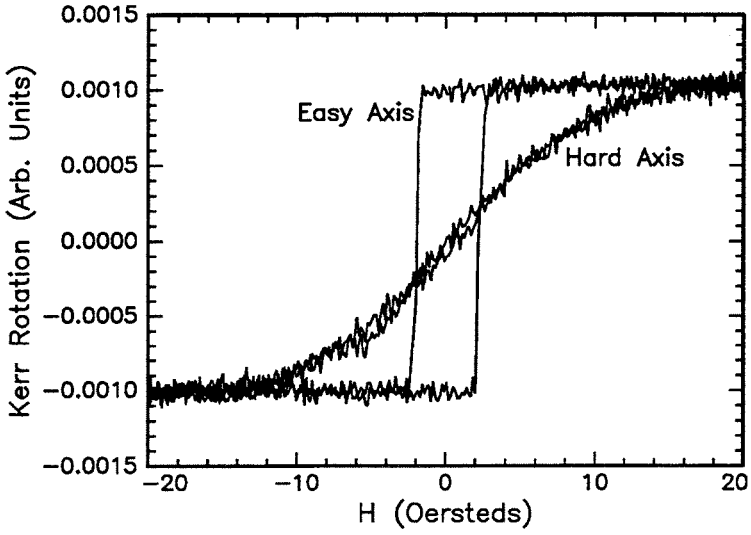

Figure 1.1: Kerr hysteresis loops for 20.0 nm thick $Ni_{80}Fe_{20}$/Cu/Si along easy and hard directions obtained using magneto-optic Kerr effect.

$\Delta\rho = \rho_{\parallel} - \rho_{\perp}$. This anisotropy in the resistivity can be expressed as[4]:

$$\rho(\theta) = \rho_{\perp} + \Delta\rho\cos^2\theta \tag{1.1}$$

where θ is the angle between $\vec{J}$ and $\vec{M}$ as illustrated by Fig. 1.3. The resulting change in the output voltage is proportional to $\Delta\rho/\rho$. For ferromagnetic elements, the AMR is a few tenths of a percent whereas for NiFe and NiCo alloys and thin films, it is a few percent at room temperature. For the composition 80-20, NiFe thin films have 2-3% AMR with a peak value of 5% at 90-10 composition. The origin of AMR has to do with the anisotropy of the Fermi surface for these alloys and the dependence of the scattering probability of conduction s electrons on the magnetic moment orientation of the d orbital[4]. Hence, magnetoresistance is also related to spin-orbit cou-

pling, which may explain its high value near the NiFe composition for which magnetocrystalline anisotropy and the magnetostriction are zero. Because of these properties, $Ni_{80}Fe_{20}$ thin films are ideally suited for magnetoresistive applications such as magnetoresistive read heads for high density magnetic recording and detectors for bubble memories[8]. Typically, in these applications, a Permalloy-coated strip is magnetized at 45° with respect to $\vec{J}$ by a bias field in order to maximize flux sensitiviy. Figure 1.2 shows the magnetoresistive signal at room temperature for a $Ni_{80}Fe_{20}$ film as its magnetization is rotated by 180° due to a field applied along the hard axis.

More recently, even higher magnetoresistance in relatively low fields has been reported for NiFe-based heterostructures[9] (see Chapter 5 for an introduction to giant magnetoresistance (GMR) in NiFe-based multilayers). In particular, spin valves[9], which consist of two ferromagnetic layers (typically NiFe) separated by an interlayer (typically Cu), with one of the ferromagnetic layers exchange-biased by an antiferromagnetic FeMn film[10], are being considered for future magnetoresistive sensors.

1.3 Relationship to Microstructure of Thin Films

Like other electronic properties, magnetic properties of thin films are also very sensitive to their microstructural properties. Deposition conditions such as substrate temperature, and Ar gas pressure in the case of sputtered films, can significantly affect the stress in the growing film. Another possible source of thin-film stress is the lattice mismatch with the substrate in epi-

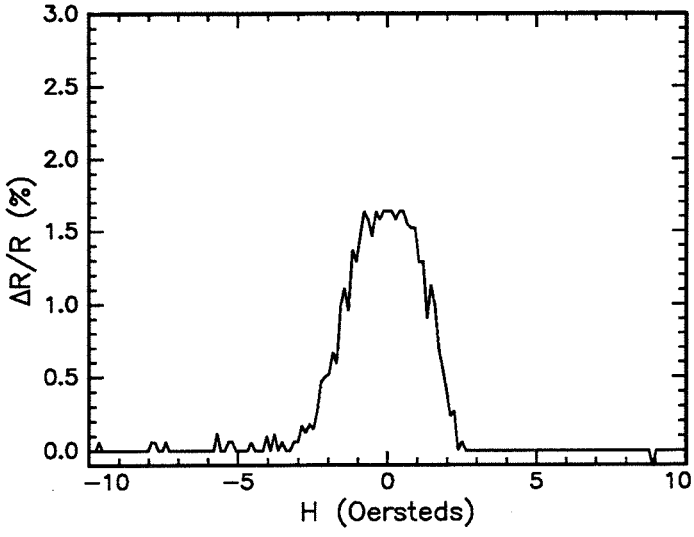

Figure 1.2: Anisotropic magnetoresistance at room temperature of a polycrystalline $Ni_{80}Fe_{20}$ film deposited on glass.

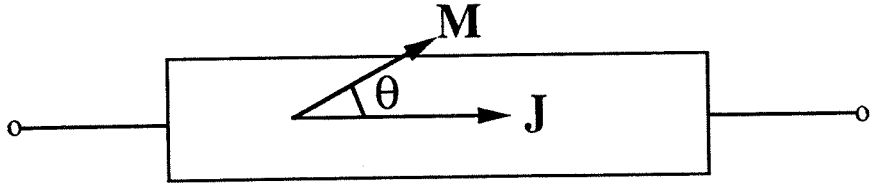

Figure 1.3: Geometry used for measurement of anisotropic magnetoresistance.

taxial growth. Now, the magnetostriction of polycrystalline $Ni_{80}Fe_{20}$ films depends sensitively on its composition and crystallographic texture. If the magnetostriction is nonzero (albeit small), it can adversely affect magnetic properties of thin films by interacting with the strain present in the film due to thermal or lattice mismatch with the substrate. Residual strain may be present in the film also as a consequence of the growth process. Structural defects in the film such as surface roughness and voids can also cause the coercivity to increase by acting as pinning sites for domain walls. Figure 1.4 shows a schematic of a thin polycrystalline film, illustrating the defects in the film which may act as pinning sites for domain walls. The arrows in the figure indicate the crystallographic orientation of the grains whereas $h(x)$ and $e(x)$ refer to the film thickness and film strain, respectively. Furthermore, the uniaxial anisotropy field H_k also is sensitive to annealing at relatively low temperatures. Thus, a field of 2000 Oe maintained at 300°C for 1 hour is sufficient to rotate the easy and hard directions of a uniaxial NiFe thin film[7]. This indicates that H_k depends not only on directional ordering of Ni and Fe atoms but also on relatively mobile structural defects in the film. Furthermore, presence of nonmagnetic atoms at the grain boundaries of $Ni_{80}Fe_{20}$ can exchange decouple the magnetic grains, causing switching behaviour of the film to be similar to that of ferromagnetic particulate arrays. This was found to be the case for $Ni_{80}Fe_{20}$/Ta multilayers annealed at T $>$ 450°C, causing accumulation of Ta at NiFe grain boundaries (more discussion in Chapter 3).

The resistivity of ferromagnetic films can be divided into spin-dependent and spin-independent components. The former, which is also responsible for the magnetoresistive part in NiFe alloy films, originates due to scatter-

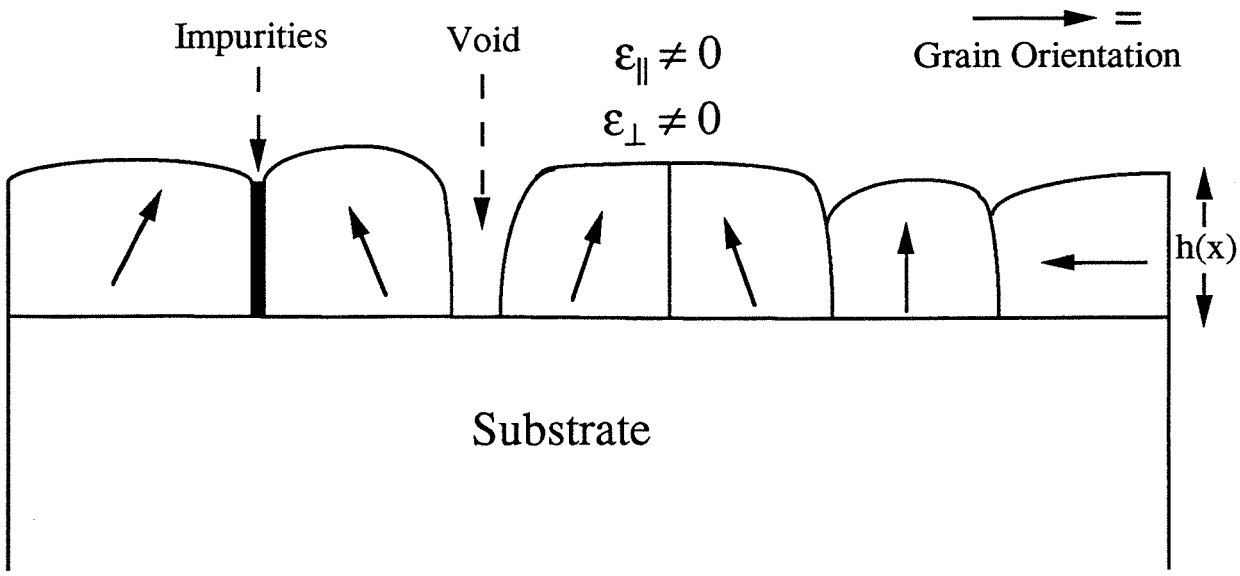

Figure 1.4: Schematic of a polycrystalline thin film illustrating the defects which can interfere with domain wall motion, and hence cause higher H_c.

ing of conduction electrons by magnetic impurity atoms, and is relatively insensitive to film thickness and structural defects. On the other hand, the spin-independent component is very sensitive to the microstructure. As the film thickness h decreases below 20.0 nm, the resistivity increases which was explained by Fuchs[11] in terms of increased interfacial scattering due to h being less than the mean free path of electrons. Grain boundaries can also cause the resistivity of polycrystalline films to be higher than that of epitaxial single-crystal films. The resistivity dependence on grain boundary density is fit well by a model due to Mayadas and Shatzkes[12]. Since the output of a magnetoresistive sensor is proportional to the ratio $\Delta\rho/\rho$, this suggests that epitaxial films may be more suited for those applications in which spin-independent scattering effects of grain boundaries are absent.

Chapter 5 discusses properties of epitaxial $Ni_{80}Fe_{20}$ films grown on Si utilizing an epitaxial Cu seed layer. Epitaxial $Ni_{80}Fe_{20}$ films have been obtained for depositions on MgO, NaCl and Cu substrates[13, 14, 15], respectively. However, none of these substrates are available with as good atomic flatness or are as technologically useful as Si wafers. The lattice mismatch between Cu and $Ni_{80}Fe_{20}$ is 1.85%; the strain due to this mismatch can affect the soft magnetic properties of NiFe films with nonzero magnetostriction. The magnetic and magnetotransport properties of these films are discussed in Chapter 5.

Finally, giant magnetoresistance in multilayers depends extremely sensitively on their microstructure, especially on interfacial roughness, crystallographic texture, and presence of voids and pinholes in the interlayers. The interface roughness is especially more important as the thickness of the nonmagnetic interlayers is typically 1-2 nm[16]. As a consequence, different investigators have reported drastically different GMR for multilayers grown, for example, by sputtering as opposed to thermal evaporation[17]. Epitaxial growth of $Ni_{80}Fe_{20}$/Cu on Si suggests the possibility of growing grain boundary-free, atomically sharp $Ni_{80}Fe_{20}$/Cu multilayers, in particular epitaxial spin-valve heterostructures. To date, these structures have been composed of polycrystalline films with possibly atomically-rough interfaces[9].

Bibliography

[1] U. Enz, "Magnetism and Magnetic Materials," in *Ferromagnetic Materials*, ed. by E.P. Wohlfarth, v.3, p.3, North-Holland, Netherlands, 1982.

[2] H.J. Williams, Phys. Rev. **52**, 747 (1937).

[3] B.D. Cullity, *Introduction to Magnetic Materials* (Addison-Wesley, Philippines, 1972), Ch.13.

[4] T.R. McGuire and R.I. Potter, IEEE Trans. Mag. **MAG-11**, 1018, 1975.

[5] E. Klokholm and J.A. Aboaf, J. Appl. Phys. **52**, 2474 (1981).

[6] M. Takahashi, J. Appl. Phys. **33**, 1101 (1962).

[7] M. Prutton in *Thin Ferromagnetic Films*, Butterworth & Co., England, 1964.

[8] D.A. Thompson, L.T. Romankiw, and A.F. Mayadas, IEEE Trans. Mag. **MAG-11**, 1039, 1975.

[9] B. Dieny, V.S. Speriousu, B.A. Gurney, S.S.P. Parkin, D.R. Wilhoit, K.P. Roche, S. Metin, D.T. Peterson, and S. Nadimi, J. Magn. Magn. Mater. **93**, 101 (1991).

[10] C. Tsang, N. Heiman, and K. Lee, J. Appl. Phys. **52**, 2471 (1981).

[11] K. Fuchs, Proc. Cambridge Phil. Soc. **34**, 100 (1938).

[12] A.F. Mayadas and M. Shatzkes, Phys. Rev. B **1**, 1382 (1970).

[13] M.H. Kryder and F.B. Humphrey, J. Appl. Phys. **42**, 1808 (1971).

[14] R.D. Burbank and R.D. Heidenreich, Phil. Mag. **5**, 373 (1960).

[15] U. Gradmann and J. Muller, J. Appl. Phys. **39**, 1379 (1968).

[16] S.S.P. Parkin, Appl. Phys. Lett. **60**, 512 (1992).

[17] W.F. Egelhoff, Jr. and M.T. Kief, IEEE Trans. Mag. **28**, 2742 (1992).

Chapter 2

Instrumentation for Thin Film Deposition, Structural and Magnetic Characterization

2.1 Introduction to Ion-Beam Sputtering for Deposition of Thin Films

The erosion of material by energetic ions in a plasma has been a known problem for almost a century, since the invention of the light bulb. Currently, this *problem* is utilized extensively in industry for etching materials as well as for depositing thin films, and is known as *sputtering*. Typically, in an industrial sputter-deposition system, a plate of the material which needs to be deposited is connected to a negative voltage supply (dc or rf)[1]. An inert gas, typically Ar, is introduced into the chamber to sustain a plasma. The gas pressure is typically a few millitorr. The substrate as well as the walls of the chamber are kept at ground potential so that the ions in the plasma interact mainly with the target. In rf sputtering, there is some "leakage" of

ions which make it to the substrate and may cause (un)desired modification of the deposited film[1]. To control this leakage flux, the substrate can be biased slightly. In the case of dc sputtering, there is no ion bombardment of the substrate. However, rf sputtering has the advantage that it can be used to sputter insulators as well because at radio frequencies, voltages can still be coupled to them by matching impedance[1]. In *magnetron* sputtering, a magnetic field is used to enhance the plasma interaction with the target surface, which is particularly important for ferromagnetic materials which have very low sputtering rates otherwise[1]. Another method of sputtering materials not used as extensively in industry, but nevertheless quite important, is *ion-beam* sputtering. This method of sputtering was originally developed in 1960 for space propulsion applications as an ion thruster[2]. Since then, it has evolved into an extremely useful research tool for investigating sputtering process as well as obtaining high purity films. The ion gun essentially consists of a discharge chamber filled with Ar gas and a tungsten filament as a source of electrons which are accelerated to the anode. The presence of cylindrical magnets along the walls of the discharge chamber forces the electrons to follow helical orbits, thus increasing their ionization cross section and creating an Ar plasma. A screened grid which has the same potential as the cathode allows some of the ions from the plasma to escape[3]. These ions are further accelerated by a potential of 1-2 kV while exiting, thus forming an ion-beam which can be focused at a target some distance away. Owing to charge repulsion, the ion-beam spreads out with distance and eventually acquires a Gaussian profile[1]. For this reason, the ion gun should be placed as close to the target as possible to avoid possible sputtering of the target

holder and the walls of the chamber. A schematic of the UHV sputtering system utilizing such an ion gun for sputter deposition is shown in Fig. 2.2.

The actual interaction of ions with a target surface which leads to ejection of atoms is a fairly complex process[4]. For the energy range of 0.1-20 keV, the ions generate a collision cascade beneath the target surface. In the course of these collisions, some of the ion energy can be transferred to atoms near the target surface, leading to their ejection. The ratio of ejected target atoms to incoming beam ions is known as the *sputtering yield.* At energies higher than 20 keV, ions penetrate deeper into the solid resulting in a decrease in the sputtering yield. The sputtering yield is also dependent on the angle of incidence of the ions. It increases with angle of incidence away from normal incidence to a maximum which depends on ion and target species and energy[1], then decreases to zero at grazing incidence angles.

The energetic ions, after penetrating the target material, lose energy via Coulombic scattering from the atomic cores and from electronic excitations in the solid[4]. These two types of stopping mechanisms are referred to as nuclear and electronic stopping powers. It is the former type of collisions which leads to ejection of atoms from the target surface, or sputtering. A universal curve for nuclear stopping power was derived by Lindhard, Scharff and Schiott[5]. Sigmund extended this theory to correlate the energy distribution of sputtered atoms with the nuclear stopping power[6]. This theory predicts a log-normal energy distribution with a mean energy of few eV and a small fraction of sputtered atoms possessing energy as high as 30-60 eV. This is found to be in good agreement with experimental results such as those shown in Fig.2.1, which gives the energy distribution of atoms and

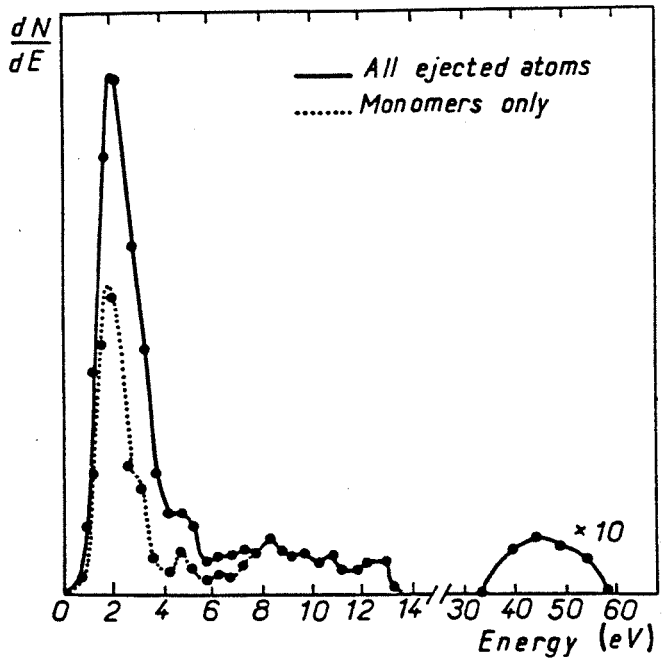

Figure 2.1: The experimentally measured energy distribution of atoms sputtered from a Cu target by 600 eV Ar ions[7].

clusters ejected from a Cu target by 600 eV Ar ions[7]. By comparison, the mean energy of evaporated atoms is of the order of a few tenths of an eV. As a consequence, the structural and electronic properties of evaporated films can be significantly different from those of sputtered films. Furthermore, in sputtering, there can be significant incorporation in the film of the sputtering gas used (up to a few %) which can alter properties of the sputtered films as well[4]. This incorporation is higher for lighter element noble gases such as Ar which can occupy interstitial sites. Finally, high energy neutral atoms of the sputtering gas specularly reflected from the target, can also bombard the substrate during film growth. Their exact fraction depends upon the deposition geometry and can affect properties of the films as well[4].

2.2 UHV Sputtering System

Figure 2.2 shows the schematic of the ultra-high vacuum (UHV) sputtering system used primarily for deposition of metal films in the experiments described in this thesis. It uses a 3 cm ion-beam source manufactured by Ion Tech, with Ar as the sputtering gas. Up to 3 different targets can be mounted on a triangular target assembly as shown in Fig. 2.2. A 300 l/s Balzers turbopump with a mechanical pump as the backing pump is used for achieving UHV in the main chamber. The main chamber is interfaced to a load lock chamber which allows samples to be loaded without breaking vacuum. A separate 60 l/s turbopump is used for pumping the load lock and differentially pumping the reflection high energy electron diffraction (RHEED) gun. A base pressure of 4×10^{-10} torr can be achieved in the main chamber, after a day-long bake-out and if system cleanliness is maintained properly. The Ar flow was 3.0 sccm which resulted in an Ar pressure of 2.5×10^{-4} Torr during sputtering. The purity of the Ar gas was 99.99% which was further improved to impurity levels of $\leq$ 1 ppm by passing the gas through a bakeable Ar filter from Ultrapure Systems. The ion beam was typically operated at a beam voltage of 1200 V, $\leq$ 100 V accelerator voltage, and a discharge voltage of 38.0 V. The cathode current varied from 2.0-4.0 amperes depending upon the filament lifetime. See Appendix A for more details of the instrumentation and operating parameters. The film thickness during deposition was measured using a Inficon thickness monitor which utilizes a piezoelectric quartz crystal. The film thickness thus measured was calibrated for some samples using Rutherford backscattering spectrometry.

The film composition for certain samples was determined after deposition using electron probe microanalysis (EPMA).

The system is also equipped with a 15 keV Vieetech RHEED gun to monitor the crystallographic texture of the growing film. See Sec.2.4 for more details of this tool for *in situ* structural analysis. A horseshoe shaped electromagnet was placed close to the sample outside the sputtering chamber during deposition, to induce uniaxial anisotropy in the $Ni_{80}Fe_{20}$ film. The electromagnet was used instead of a permanent magnet inside the chamber because the strong magnetic field due to the latter interfered with the RHEED measurements. Finally, the system is also interfaced to a quartz tube which allowed *in situ* measurement of magnetic properties of thin films using the magneto-optic Kerr effect (MOKE) as described in the next section.

2.3 *In Situ* Magnetic Characterization using Magneto-Optic Kerr Effect

2.3.1 Theory

The magneto-optic Kerr effect (MOKE) refers to the interaction of the polarization of light reflected from a magnetic thin film. This is due to the inequivalent interactions between the magnetization $\vec{M}$ of the sample and the s & p polarizations of the light where s and p refer to the electric field vectors being perpendicular and parallel to the plane of incidence, respectively. The origin of the effect is due to the spin-orbit interaction within the magnetic medium which gives rise to off-diagonal terms in the dielectric tensor governing the reflectivity[8, 9]. Thus, when plane polarized light containing only s

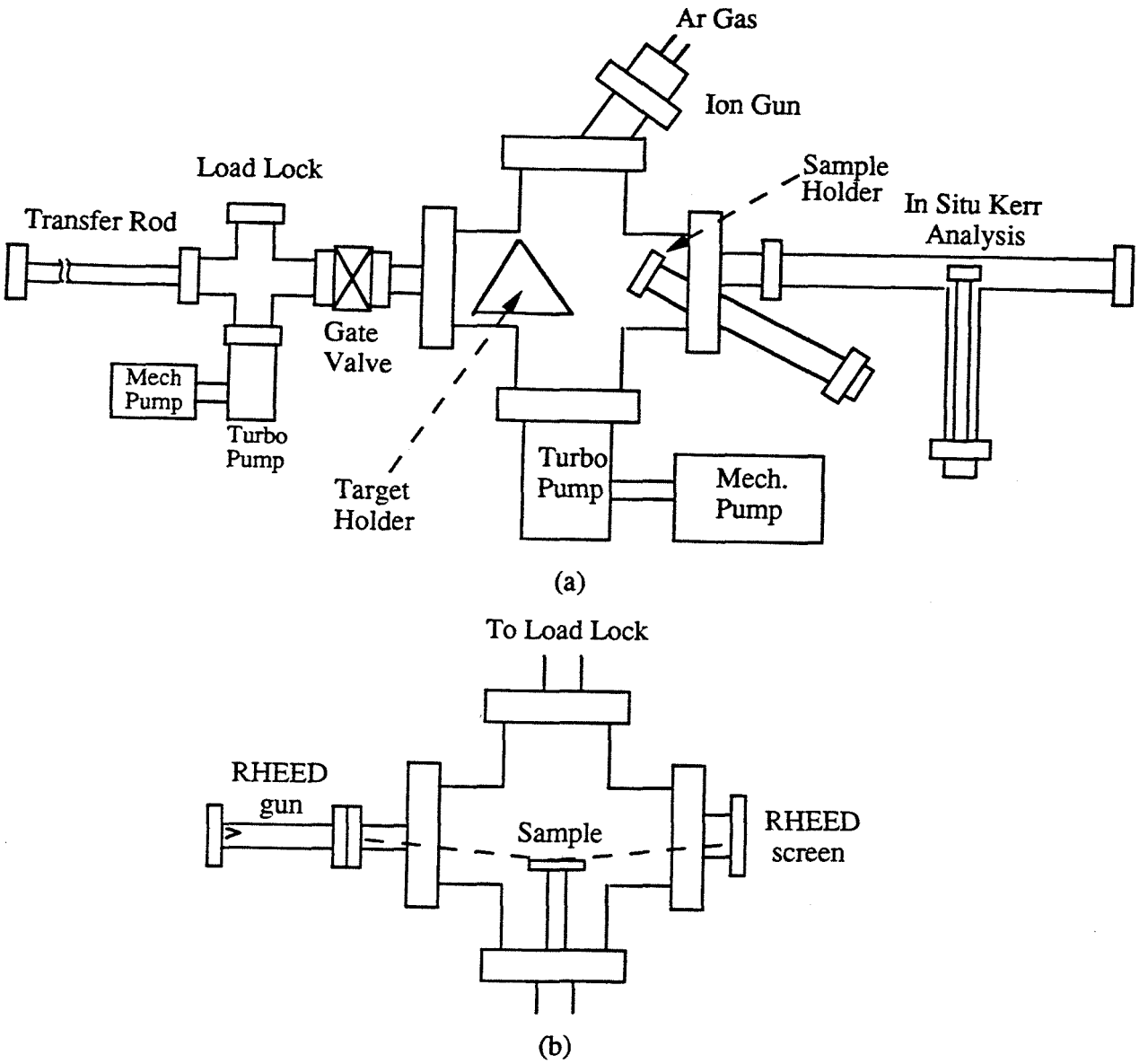

Figure 2.2: Schematic of UHV sputtering system with *in situ* magneto-optic Kerr and reflection electron diffraction analysis. (a) Side view and (b) top view.

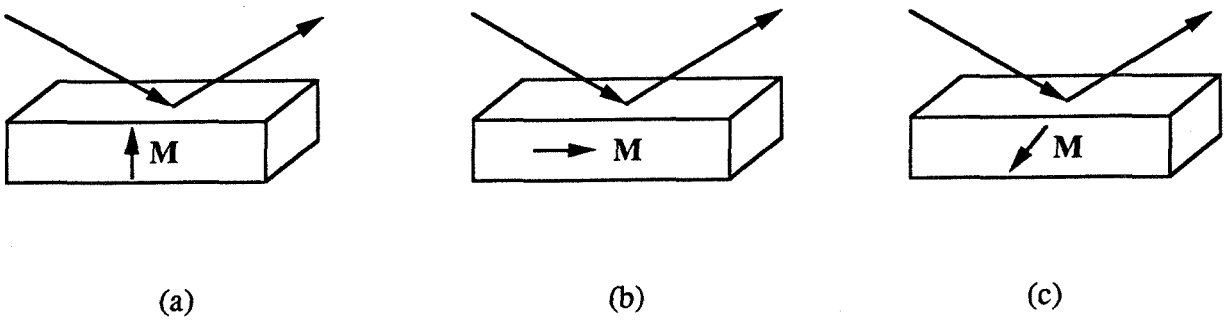

Figure 2.3: Various configurations for observing the magneto-optic Kerr effect. (a) Polar. (b) Longitudinal. (c) Transverse.

or p component, is reflected from a magnetic film, it acquires a component of polarization which was not present in the incident light. This *rotation* of the polarization can be measured using a Wollaston prism which splits the light into its two components. The MOKE measurements are usually carried out in one of the three geometries[10] shown in Fig. 2.3; namely, longitudinal ($\vec{M}$ parallel to the plane of incidence and in-plane), transverse ($\vec{M}$ perpendicular to the plane of incidence and in-plane) and polar ($\vec{M}$ parallel to the plane of incidence and perpendicular to plane of sample).

The reflection of light from a magnetic film can be expressed mathematically as:

$$\begin{pmatrix} E_s^r \\ E_p^r \end{pmatrix} = \begin{pmatrix} \tilde{r}_{ss} & \tilde{r}_{sp} \\ \tilde{r}_{ps} & \tilde{r}_{pp} \end{pmatrix} \begin{pmatrix} E_s^i \\ E_p^i \end{pmatrix} \tag{2.1}$$

where $\tilde{r}_{ss,sp,ps,pp}$ are the Fresnel reflection coefficients coupling $E_{s,p}^r$ and $E_{s,p}^i$,

the reflected and the incident electric field vectors for the two polarizations, respectively. If the incident light is linearly polarized (say s) then Eq. (2.1) reduces to:

$$\begin{pmatrix} E_s^r \\ E_p^r \end{pmatrix} = \begin{pmatrix} \tilde{r}_{ss} E_\circ \\ \tilde{r}_{sp} E_\circ \end{pmatrix} \tag{2.2}$$

where $E_\circ \equiv E_s^i$. The rotation $\theta_{s,p}$ in s or p polarizations after reflection from a ferromagnetic film, known as Kerr rotation, can also be expressed in terms of the Fresnel reflection coefficients introduced above. Thus, for s-polarization, the Kerr rotation is:

$$\theta_s = \mathrm{Re}\frac{\tilde{r}_{sp}}{\tilde{r}_{ss}}. \tag{2.3}$$

Kerr rotation for p-polarization can be similarly expressed. For $Ni_{80}Fe_{20}$, $\theta_{s,p} \sim 0.01°$ which corresponds to a change in polarization of 1 photon out of 10^4. Figure 2.4 shows the variation of $\theta_{s,p}$ with incident angle for various thicknesses of $Ni_{80}Fe_{20}$ film, as computed from expressions for Fresnel coefficients in terms of the dielectric tensor ϵ_{ij} for magneto-optic materials[10] whereas Fig.2.5 shows the variation of Kerr rotation for s polarization with $Ni_{80}Fe_{20}$ film thickness. The minimum in θ_p near 60° corresponds to the strong absorption of that component near Brewster's angle.

The two polarizations of the reflected light can be separated using a Wollaston prism and detected by a photodiode pair each of which gives out a voltage signal proportional to the intensity incident upon it. Besides the Kerr rotation, the reflected light also gets elliptically polarized due to the fact that the s and p components are not in phase after reflection. For s

polarization, this ellipticity, known as Kerr ellipticity, can be defined as

$$\epsilon_s = \mathrm{Im}\frac{\tilde{r}_{sp}}{\tilde{r}_{ss}}. \tag{2.4}$$

This ellipticity can be eradicated by inserting a quarter-wave plate (with proper orientation of its slow and fast axes) before the Wollaston prism[11]. This elimination of the phase difference between the s and p components results in an enhancement of the Kerr rotation. Figure 2.6 shows the schematic of optical components used for Kerr effect magnetometry of thin films. If I_A and I_B correspond to the intensity of the s and p components respectively, then they can be expressed in terms of Fresnel coefficients and E_o as given by:

$$\begin{aligned} I_A &= |E_s^r|^2 = \tilde{r}_{ss}\tilde{r}_{ss}^* E_o^2 \\ I_B &= \left|E_p^r\right|^2 = \tilde{r}_{sp}\tilde{r}_{sp}^* E_o^2. \end{aligned} \tag{2.5}$$

Using Eq. (2.3) & (2.5), it can be shown that the difference of the two intensities, normalized by the total incident intensity, is related to the Kerr rotation as follows:

$$\frac{I_A - I_B}{I_A + I_B} = 2\sin\theta_s\cos\theta_s \tag{2.6}$$

or for small θ_s,

$$\frac{I_A - I_B}{I_A + I_B} \propto \theta_s. \tag{2.7}$$

Now the dependence of $\theta_{s,p}$ on the magnetization $\vec{M}$, although complex, nevertheless is quasilinear as shown by the plot of $\theta_{s,p}$ vs. $Ni_{80}Fe_{20}$ film thickness in Fig.2.5. Hence, the difference between the output voltage signals of the photodiode pair, V_A and V_B normalized by the sum i.e., $\frac{V_A - V_B}{V_A + V_B}$ will

vary quasilinearly with the magnetization $\vec{M}$ of the film. Thus, if this signal is plotted against the applied field H for a ferromagnetic film, a hysteresis loop known as the "Kerr" loop can be obtained with the ordinate being Kerr rotation instead of the magnetization M. Using an appropriate expression for $\theta_{s,p}$ in terms of M or a table of computed values, this "Kerr" loop can be converted to a regular hysteresis loop. Nevertheless, the coercivity H_c and the magnetic anisotropy H_k for the uniaxial magnetic film can be obtained directly from the "Kerr" loop without conversion of $\theta_{s,p}$ to M.

2.3.2 Implementation

Magnetic properties were measured *in situ* using the magneto-optic Kerr effect as described above, after sample transfer to a quartz tube interfaced to the UHV-sputtering system as shown in Fig. 2.2. A 670 nm semiconductor diode laser beam *s*-polarized by a Glan-Thompson polarizer was used as the incident beam with the angle of incidence being approximately 70° from sample normal. This incidence angle was chosen to exploit the maximum in θ_s as shown in Fig.2.4. Two pairs of Helmholtz coils were used to magnetize the sample such that "Kerr" loops could be observed for longitudinal and polar geometry. The rotation in polarization after reflection from the magnetic sample was detected using a Wollaston prism and a photodiode pair. The sum and difference voltage signals from the photodiodes were amplified and acquired on a 386 computer using a Data Translation data acquisition board (Model #2821) and customized software. The computer was also used to control a 20V/10A Kepco power supply which provided the current to the Helmholtz coils. The applied field H can be computed from this current, the

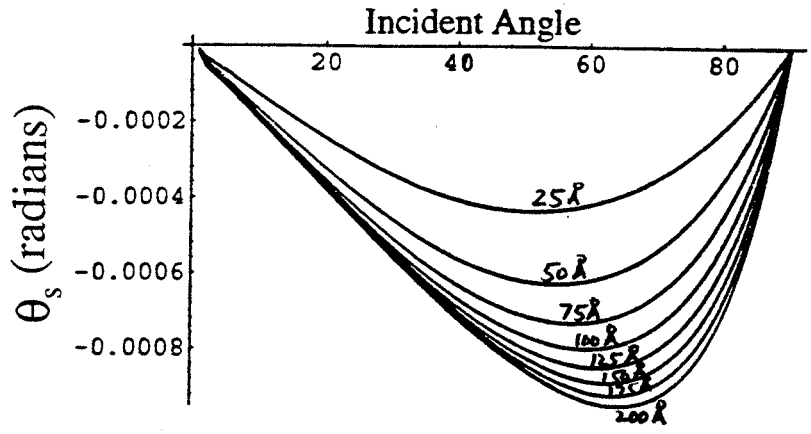

(a)

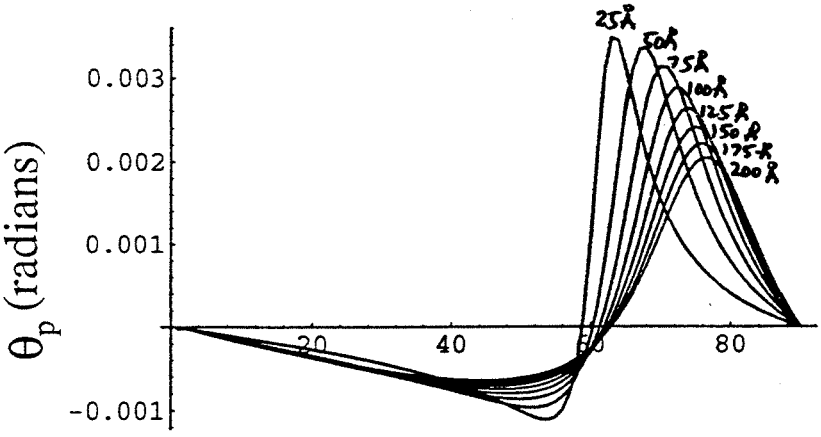

(b)

Figure 2.4: Variation of Kerr rotation with incident angle for (a) s and (b) p polarizations for various NiFe film thicknesses.

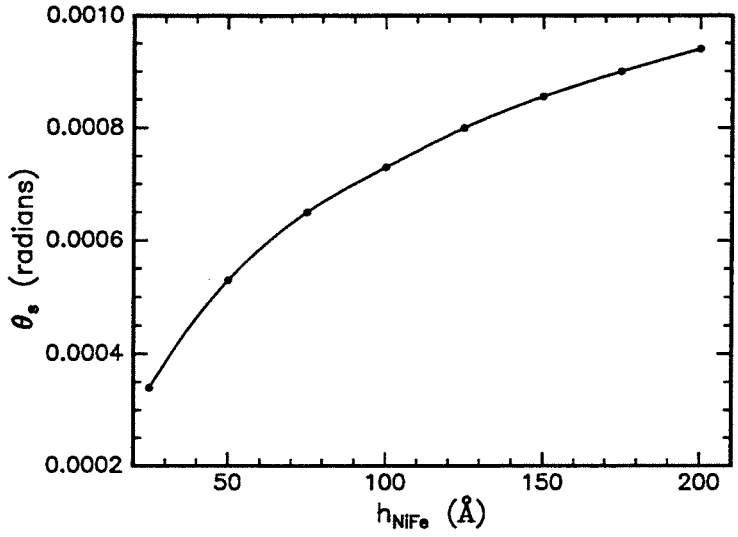

Figure 2.5: Variation of Kerr rotation with NiFe film thickness for s polarization.

number of turns and the geometry of the Helmholtz coil. Thus, by plotting the voltage signal from the photodiodes vs. the ac applied field H, a "Kerr" hysteresis loop can be graphed on the computer. The driving ac frequency was typically 1 Hz; signal-to-noise ratio was improved by averaging over more than one cycle. The sample holder was designed such that the sample could be rotated about its surface normal thus allowing in-plane easy and hard axis longitudinal "Kerr" loops to be measured. Using this setup, "Kerr" loops were obtained for $Ni_{80}Fe_{20}$ films as thin as 2.0 nm. Appendix A lists some suggestions which might improve the resolution of the system further. Figure 1.1 shows such loops obtained for easy and hard axes using this setup for a 20 nm thick $Ni_{80}Fe_{20}$ film on SiO_2/Si. See Appendix A for more details of the software and hardware employed for data acquisition.

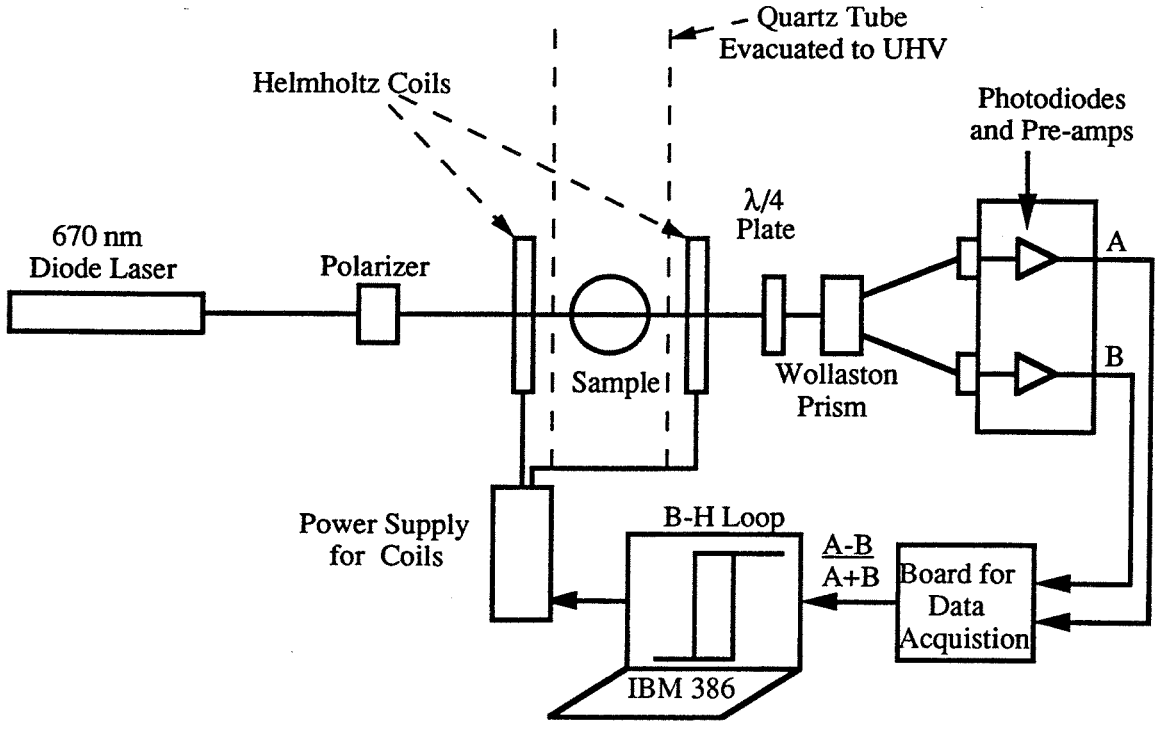

Figure 2.6: Schematic of Kerr effect magnetometer for *in situ* analysis of magnetic thin films.

2.4 *In Situ* Structural Analysis by Reflection Electron Diffraction

2.4.1 Theory

The crystallographic structure of the surface of the substrate or growing film was studied by the technique of reflection high-energy electron diffraction (RHEED). The basis of this analysis technique is the same as that employed by Davisson and Germer who first demonstrated diffraction of low energy electrons from a Ni crystal[12]. The electron diffraction is a consequence of the wave-like behaviour of the electrons and the wavelength λ of the electrons is given by the famous de Broglie relationship. Typically, the electron beam energy E ranges from 10 to 30 keV for RHEED applications. For these energies, the nonrelativistic version of the de Broglie relationship can be used, so that the electron wavelength λ in Å is given by:

$$\lambda = \frac{12.3}{\sqrt{E(\text{eV})}} \tag{2.8}$$

At 15 keV, which was the energy of the RHEED beam utilized in this experiment, $\lambda = 0.1$ Å. Thus, for grazing incidence angles, the wave-vector $\vec{k}$ of the electrons will be comparable to the interatomic spacings in a solid and can be used to obtain information about long range order in a single crystal. Depending upon the RHEED geometry, the elastically scattered electrons penetrate a very short distance into the solid[13]. As a consequence, the diffraction pattern is determined mostly by the two-dimensional surface of the solid and can be used to ascertain whether the crystalline surface is rough or smooth, reconstructed or unreconstructed. In particular, when the sur-

face is ordered and clean, i.e., has atomic steps, and the electron beam is properly oriented with respect to the sample, its diffraction pattern consists of discrete lines, known as Bragg rods. This condition is satisfied when

$$\vec{k} \cdot \vec{d} = 2\pi n \tag{2.9}$$

where n is an integer, and $\vec{d}$ is the lattice vector in the plane of the surface.

Most of the qualitative features of RHEED patterns can be understood using the kinematical theory of diffraction, just as in case of x-ray diffraction and transmission electron microscopy[14]. However, dynamical theory of diffraction is needed to calculate the RHEED intensity and its dependence on the defects in the surface.

2.4.2 Implementation

A Vieetech electron gun operating at 15 keV was used to produce an electron beam with a current of about 20 μA. The reflected beam was allowed to hit a viewport coated with fluorescent material. The angle of incidence of the beam was $\leq 5°$. Using the sample manipulator, the sample geometry can be adjusted such that the desired diffraction pattern is observed for single crystal substrate or film; typically Si substrates are viewed along [100] or [110] azimuths. At an energy of 15 keV and an incidence angle of 5°, the electron penetration depth is about 15 Å from the surface[13]. Hence, a RHEED beam is extremely sensitive to the crystallographic orientation of the surface. Furthermore, for this scattering geometry, the scattering vector $\vec{k}$ of the electron beam is in-plane so that it is sensitive to the in-plane crystallographic orientation and lattice constant of the film.

During film growth, the RHEED gun was differentially pumped by a 60 l/s turbopump to allow its operation at sputtering gas pressures. For certain film growths, the RHEED patterns were recorded using a video camera and then frame-grabbed onto a MacII computer. Great care was taken to ensure that the RHEED camera length did not change during these measurements, i.e., the sample and the RHEED beam position were kept fixed. The resulting images were analyzed using Image software (courtesy of National Institute of Health Sciences) to find the intensity profile across the Bragg rods in the RHEED pattern. These intensity profiles were used to calculate the separation of the Bragg spots or the reciprocal lattice spacing K, which can be related to the surface lattice constant a in the plane of the film or the substrate, as given by:

$$K = \frac{2\pi}{a}. \tag{2.10}$$

The surface lattice constant measurements thus obtained were used to get information about the evolution of the crystallographic texture of the film and the in-plane strain $\epsilon_{||}$ in the film, as defined by:

$$\epsilon_{||} = \frac{a_{\text{film}} - a_{\text{substrate}}}{a_{\text{substrate}}}. \tag{2.11}$$

See Chapter 5 for strain measurements for epitaxial growth of $Ni_{80}Fe_{20}$ films on Cu, and comparison with the strain relaxation as predicted by theory.

2.5 X-ray Diffraction Studies

2.5.1 Small Angle X-ray Diffraction

The diffractometer used for small angle x-ray diffraction (SAXD) consisted of a GE x-ray power supply and tube tower equipped with a Cu source, $\theta - 2\theta$ goniometer, EG&G proportional counter and detector electronics, and a sample holder mounted on high resolution rotation and translation stages to allow accurate alignment of the sample with respect to the main beam (for an introduction to the theoretical basis for SAXD, please refer to Sec.3.2). The last addition was necessary as the higher satellites were quite sensitive to accurate alignment of the sample and the diffractometer. A Ni filter was placed in front of the x-ray detector to absorb Cu-K_β radiation. Later, the GE x-ray power supply was replaced by a 2.5 kW Inel XRG-2500 power supply and a tube tower. The new tube tower was equipped with a graphite monochromator which led to narrower x-ray peakwidths. See Appendix A for more details of hardware and procedures used for maximizing the SAXD satellite intensities.

2.5.2 Large Angle X-ray Diffraction

Crystallographic texture of the thin films on Si was assessed by x-ray diffraction utilizing an Inel Thin Film Diffractometer. Most of the measurements were performed using a Co-K_α x-ray source with fixed incident beam angles in the range from 5°-45° in 5° intervals, along both the [100] and [110] azimuths of the Si(100) substrate. Scattered x-rays were measured using a parallel detection and data acquisition instrument simultaneously over an

angular range of 120° with 0.05° angular resolution. While not a complete pole figure analysis, these measurements do probe a wide range of reciprocal space, and thus provide a more comprehensive picture of film texture than can be obtained from a single $\theta - 2\theta$ diffraction measurement.

2.6 Transmission Electron Microscopy

Transmission electron microscopy was performed on a Phillips EM430 electron microscope. The point resolution of the microscope is 2.3 Å. Also available with the microscope are analytical instrumentation such as an energy dispersive x-ray detector, an electron energy loss spectrometer, and a scanning transmission electron microscopy unit. For cross-sectional transmission electron microscopy (XTEM) analysis, a double-tilt goniometer was used to align the film/substrate interface along the [110] zone axis for Si(100) substrates. Plan view sample preparation was done by back-etching of the Si substrate using HF:HNO_3:H_2O solution. For XTEM analysis, two 2.5 mm by 1.0 mm pieces of the samples were glued together using adhesives which did not require high-temperature curing. These were mechanically lapped and polished and then mounted on a 2.5 mm diameter Cu grid using epoxy. Next, the samples were dimpled until a small hole was made near the film/substrate interface. Finally, the samples were further thinned by ion-milling using 5 keV Ar^+ ions and inserted into the microscope immediately afterwards for analysis.

2.7 Additional Characterization Tools

Besides the above mentioned characterization techniques, electron probe microanalysis was used to determine the composition of the thin films deposited. In particular, the amount of metallic impurities and Ar incorporated in the film, as a consequence of sputter-deposition process, was estimated. The resolution of this technique is approximately 10-20 ppm for 20.0 nm thin films, within a spot size of 1 micron. Rutherford backscattering spectrometry (RBS) was also utilized for composition analysis, as well as for calibrating the thickness and uniformity of some of the samples. Details of this tool for thin film analysis are given in Ref[15]. Atomic force microscopy (AFM) was also used to evaluate the surface roughness of some of the $Ni_{80}Fe_{20}$ epitaxial thin films on Cu/Si(100).

Bibliography

[1] J.L. Vossen and W. Kern, *Thin Film Processes*, (Academic Press, Orlando, 1978) pp. 175-206.

[2] H.R. Kaufman and P.D. Reader, Am. Rocket Soc. [Pap.] No. 1374-60 (1960).

[3] Ion Source Manual, Ion Tech, Inc., Fort Collins, Colorado.

[4] J.C. Pivin, J. Mat. Sci. **18**, 1267 (1983).

[5] J. Lindhard, M. Schraff, and M.E. Schiott, Kgl. Danska Videnskab. Selskab. Mat. Phys. Medd. **33**, (1963).

[6] P. Sigmund, Phys. Rev. **184**, 383 (1969).

[7] B.J. Garrison, N. Winograd, and D.E. Harrison, J. Chem. Phys. (1978).

[8] M.J. Freiser, IEEE Trans. Mag., **MAG-4**, 152 (1968).

[9] T. Yoshino and S. Tanaka, Jap. J. Appl. Phys. **5**, 989 (1966).

[10] J.H. Judy, "Magneto Optics Theory," in *Proceedings, Conference on Advances in Magnetic Recording*, N.Y. Acad. of Science **189**, 239 (1972).

[11] P. Wolniansky, S. Chase, R. Rosenvold, M. Ruane, and M. Mansuripur, J. Appl. Phys. **60**, 346 (1986).

[12] C.J. Davisson and L.H. Germer, Phys. Rev. **30**, 705 (1927).

[13] L.C. Feldman and J.W. Mayer, *Fundamentals of Surface and Thin Film Analysis*, (Elsevier Science, New York, 1986) p. 129.

[14] B. Fultz, *Diffraction Theory with Applications to X-ray Diffraction and Electron Microscopy*, to be published.

[15] W.K. Chu, J.W. Mayer, and M.A. Nicolet, *Backscattering Spectrometry*, Academic Press, Orlando, 1978.

Chapter 3

Structural Stability and Magnetic Properties of $Ni_{80}Fe_{20}$/Ta Multilayers

3.1 Motivation

Thin films of $Ni_{80}Fe_{20}$ are of considerable interest to magnetoresistive sensors owing to their favorable soft magnetic properties such as low magnetocrystalline anisotropy, low magnetostriction, and high permeability. However, these properties depend sensitively on the microstructure of the film which is related to the film deposition conditions, as well as interfacial stability during post-growth thermal annealing. The objective of this study was to relate the evolution of microstructure to soft magnetic properties during thermal annealing of multilayer films which were composed of sequences of $Ni_{80}Fe_{20}$/Ta bilayers. Ta was chosen as it is typically used as an encapsulation material for $Ni_{80}Fe_{20}$ thin films for magnetoresistive sensor applications.

As discussed in Sec.1.2, the magnetoresistance ratio ($\Delta\rho/\rho$) of a thin film

varies inversely with its resistivity ρ which for a polycrystalline $Ni_{80}Fe_{20}$ film is affected by grain boundary and interfacial scattering[1]. Thus, achievement of larger grain sizes compared to the mean free path for electron scattering is desirable. One approach to reducing grain boundary scattering is by thermally induced grain growth. For $Ni_{80}Fe_{20}$ thin films, two activation energies for grain growth have been estimated from changes in resistivity with thermal annealing; they are 0.70 ± 0.05 and 1.86 ± 0.15 eV, accounting for grain growth in two temperature regimes[2]. However, annealing treatments have been reported to adversely affect the soft magnetic properties of $Ni_{80}Fe_{20}$; in particular, the coercivity H_c increases[3]. A possible cause for the increase in coercivity is the phenomenon of thermal grooving which occurs at grain boundaries in polycrystalline films[4]. During thermal annealing, grain boundary grooves deepen and eventually lead to the formation of voids between grains, and the transport of matter away from the grooves often takes place via surface diffusion. However, if the polycrystalline film is encapsulated, groove formation may be significantly retarded, presumably due to inhibition of surface diffusion [5].

In multilayer films, interdiffusion into $Ni_{80}Fe_{20}$ layers from adjacent films during annealing can dramatically affect its magnetic properties. The thermal stability of $Ti/Ni_{80}Fe_{20}$ films has been investigated using diffusion couples and high angle x-ray diffraction[6]. However, quantitative conclusions about kinetics of interdiffusion could not be obtained from that study because of insensitivity of the characterization method used. In this study, we did a detailed analysis of interdiffusion kinetics of $Ta/Ni_{80}Fe_{20}$ using small angle x-ray diffraction (SAXD) from multilayers, which is an extremely sensitive

probe of interdiffusion at low temperatures [7]. From the Ni-Ta phase diagram, it can be observed that Ta has relatively high solubility in Ni (7 at. % at 600°C[8]) whereas solubility of Ni in Ta is much lower (< 0.14 at. % at 600°C). Thus, some Ta solubility in $Ni_{80}Fe_{20}$ is anticipated from thermodynamics upon annealing at sufficiently high temperatures. The kinetics of Ni diffusion into Ta might be expected to be rapid as in case of Ni-Zr system which undergoes a solid-state amorphization reaction[9]. However, at lower temperatures and smaller grain sizes, grain-boundary diffusion, which may not correlate at all with bulk diffusion kinetics, should dominate. The presence of Ta in Ni is known to lead to a reduction in magnetic moment (20 at. % Ta in Ni reduces its magnetic moment to zero [10]). This suggests that the $Ta/Ni_{80}Fe_{20}$ system can be used to investigate very quantitative correlations between interdiffusion and changes in soft magnetic properties of $Ni_{80}Fe_{20}$.

Finally, SAXD has not been used as commonly for detailed analysis of interdiffusion in polycrystalline films as for amorphous or epitaxial films[7]. In view of that, a model to enable the application of SAXD to analyze grain-boundary diffusion with concurrent grain growth in polycrystalline multilayers is discussed in Sec.3.3.

3.2 Small Angle X-ray Diffraction

3.2.1 Introduction

The wavelength of x-rays ($\lambda \sim$ Å) makes them an ideal probe of atomic structure in solids. However, they can also be used to study artificial structures such as periodic multilayers. The Bragg condition for diffraction from

multilayer of period d can be written as:

$$kd = 2\pi m \tag{3.1}$$

where m is an integer and k is the wave vector defined by:

$$k = \frac{4\pi}{\lambda}\sin\theta \tag{3.2}$$

and θ is the incidence angle of the x-ray beam. Using Eq. (3.2.1), it can be shown that for $d \simeq 100$ Å, the Bragg satellites corresponding to the artificial periodic structure would be observed for $0 \leq \theta \leq 5°$. An example of such a diffraction spectrum using Cu K_α radiation is shown in Fig. 3.1(a) for an as-deposited $Ni_{80}Fe_{20}$/Ta multilayer of period $d = 128.7$ Å. The characteristic oscillations superposed on the higher satellites are probably due to an aperiodicity in multilayer which can be observed in the cross-sectional transmission electron microscope (XTEM) images of the multilayer as well. Figure 3.1(b) shows the best fit to the experimentally observed reflectivity using optical multilayer (OM) theory (more details of OM theory are discussed in the next section). The exact position of these higher satellites are obtained by modeling the refractive indices n for individual layers in a bilayered periodic multilayer as

$$n = 1 - \delta - i\beta, \tag{3.3}$$

where δ and β represent the multiple scattering and absorption of the x-rays in matter[12] and are given by:

$$\begin{aligned} \delta &= \frac{Nr_e\lambda^2}{2\pi}(Z + f') \\ \beta &= \frac{Nr_e\lambda^2}{2\pi}f'' \end{aligned} \tag{3.4}$$

with N being the number density of the electrons, r_e the classical radius of the electron, Z the atomic number, and f' & f'' the Honl corrections found in standard x-ray tables[13]. Typically, $\delta, \beta \ll 1$ and furthermore, β is an order of magnitude smaller than δ. Hence, it will be neglected in subsequent analysis. The condition for diffraction of x-rays from such a bilayered periodic multilayer of period $d = d_a + d_b$ becomes

$$m\lambda = 2n_a d_a \sin\theta_a + 2n_b d_b \sin\theta_b. \tag{3.5}$$

Since the difference in δ for the individual layers is small, $\theta_a \approx \theta_b$. As a result, Bragg's law, modified for periodic multilayers, can be written as

$$\left[\frac{m\lambda}{2\sin\theta}\right]^2 = d^2\left[1 - \frac{2 < \delta >}{\sin^2\theta}\right], \tag{3.6}$$

where $< \delta >$ represents a weighted average of the real part of the x-ray refractive index in the multilayer[12]. By doing a linear fit to $(m\lambda/2\sin\theta)^2$ vs. $1/\sin^2\theta$ for the Bragg satellites, the multilayer period d can thus be calculated. Figure 3.2 shows such a plot used to calculate a period of 128.7 Å for the as-deposited $Ni_{80}Fe_{20}$/Ta multilayer. For details of the instrumentation used for SAXD, please refer to Sec.2.5.1.

3.2.2 X-ray Reflectivity From Multilayers and Interface Roughness

The reflectivity of x-rays from a multilayered film can be calculated analogously to that for optical coatings, utilizing the Fresnel reflection coefficients and the refractive indices for x-rays, with the condition of continuity of the parallel component of the electric field vector across the interfaces[14]. This

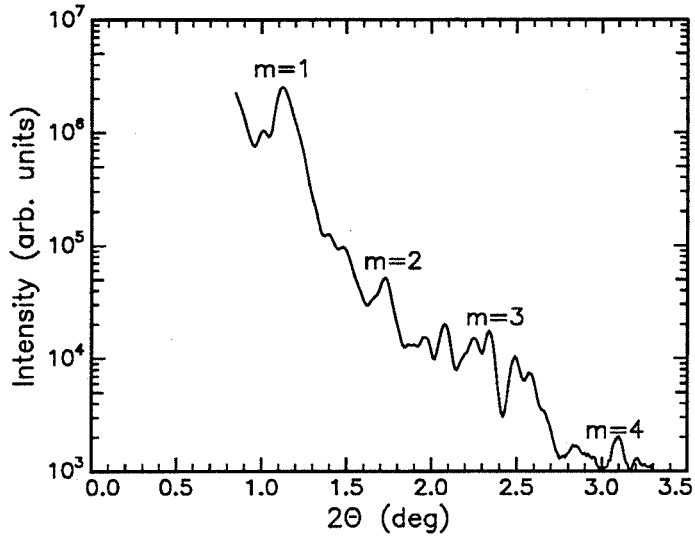

(a)

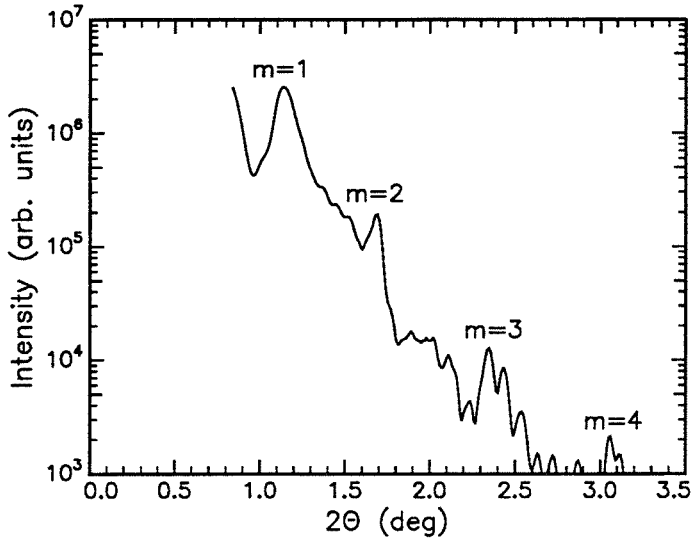

(b)

Figure 3.1: (a) Small angle x-ray reflectivity of as-deposited $Ta/Ni_{80}Fe_{20}$ multilayer (15×128 Å) using Cu K_α radiation. (b) Best fit obtained to the experimentally observed reflectivity using optical multilayer (OM) simulations.

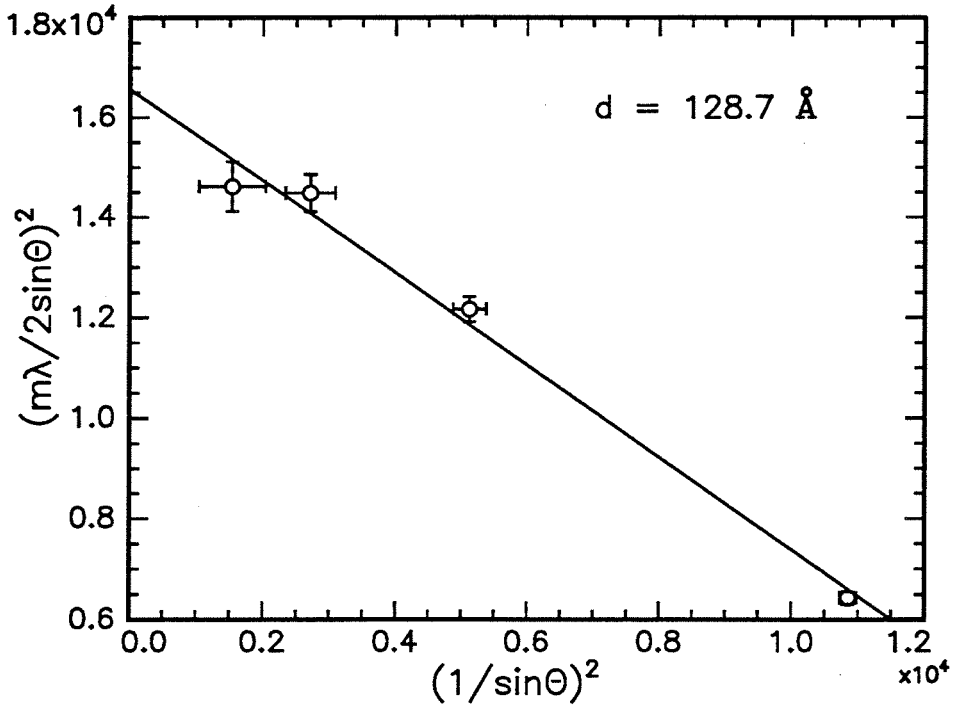

Figure 3.2: Characterization of as-deposited multilayer period from satellites observed in small angle x-ray spectrum.

approach to x-ray reflectivity from multilayered thin films is known as optical multilayer (OM) theory, and is readily adaptable to computation because of its recursive nature. One such version written by Lee Goldman and David Wu of Harvard University[15] was used to calculate the reflectivity of $Ta/Ni_{80}Fe_{20}$ multilayers and compare with the experimentally observed reflectivity (see Fig. 3.1). A comparison of ratio of satellite peak intensities was used to estimate the average thickness of $Ni_{80}Fe_{20}$ and Ta layers, which were found to be 84 ± 12 and 45 ± 9 Å, respectively.

The reflectivity of x-rays from a multilayer can also be used to estimate its interface roughness. The satellites in a periodic multilayer are superimposed on a monotonically decreasing reflectivity background, which depends on its interface roughness σ_i. Assuming σ_i is a random variable (see discussion at the end of this section), the decrease in x-ray reflectivity due to the interface roughness can be modelled by a Debye-Waller factor, analogous to the decrease in diffracted beam intensity due to thermal disorder[16], i.e.,

$$I(k) = I_o(k)\exp(-k^2\sigma_i^2) \tag{3.7}$$

where $I(k)$ and $I_o(k)$ are background reflectivities from a rough and a perfectly smooth multilayer. It can be shown that these reflectivities vary as $1/k^4$[15] where k is the x-ray wave-vector. Thus, if $\log k^4 I(k)$ is plotted versus k^2, the slope of the straight line fit to the background will be σ_i^2. Using this method, the interface roughness of the $Ta/Ni_{80}Fe_{20}$ multilayer was estimated to be 13 Å, as shown in Fig. 3.3. This was in good agreement with the interface roughness estimated from XTEM analysis.

The above analysis is based on the assumption that the interface rough-

ness of multilayers is uncorrelated. However, frequently in short period ($\leq$ 5.0 nm) multilayers, the roughness is cumulative as illustrated by a schematic shown in Fig.3.4. In such cases, σ_i cannot be treated as a random variable. The effects of correlated interface roughness on SAXD spectrum have been modelled by Payne and Clemens[17]. Specifically, their analysis predicts broadening of the diffraction features due to roughness correlations. However, in our $Ni_{80}Fe_{20}$/Ta multilayers, the period is much larger. As a result, correlations in the roughness are unlikely and are not evident in XTEM analysis of as-deposited multilayers. Hence, the above analysis may be justified for estimating the interface roughness of the as-deposited multilayers.

3.2.3 Interdiffusion in Multilayers and Small Angle X-ray Diffraction

Measuring the decay of the satellites in SAXD spectrum as a function of annealing time is one of the most sensitive methods for calculating diffusion coefficients at low temperatures[7]. The electron density $\rho_e(z)$ in a periodic multilayer can be represented as a Fourier series:

$$\rho_e(z) = \sum_{m=0}^{\infty} A_m \sin(k_m z + \phi_m) \tag{3.8}$$

where $k_m = 2\pi m/d$ is the "reciprocal" lattice vector of the artificial periodic multilayer. Now, for Fickian diffusion, the diffusion equation is[20]:

$$\frac{\partial C(z,t)}{\partial t} = D\frac{\partial^2 C(z,t)}{\partial z^2}, \tag{3.9}$$

where $C(z,t)$ is the time-dependent concentration profile of the multilayer and D is the diffusion constant. The standard solution by Fourier decompo-

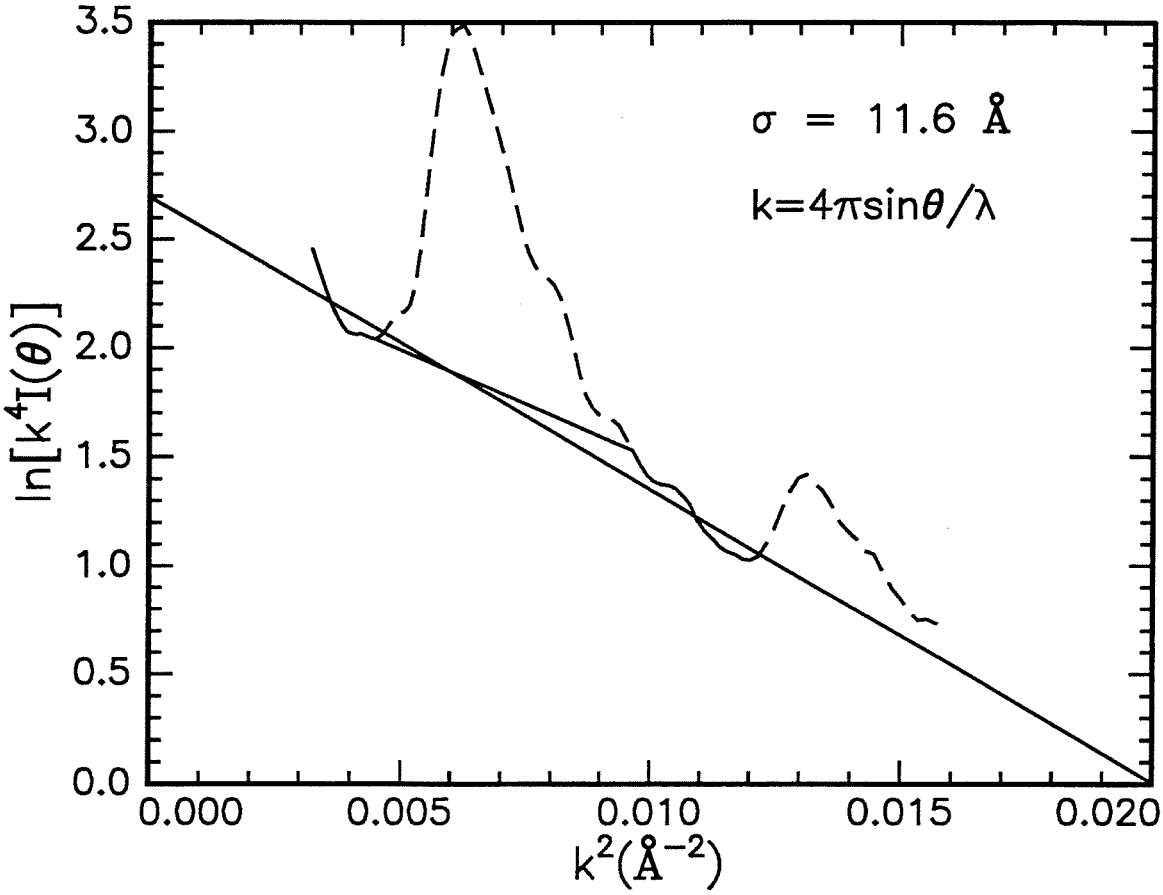

Figure 3.3: Interface roughness calculated from fit to background x-ray reflectivity from $Ta/Ni_{80}Fe_{20}$ multilayer.

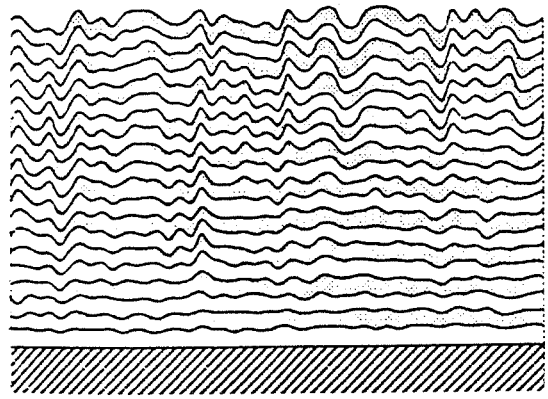

Figure 3.4: Schematic showing the evolution of correlated interface roughness in a short period multilayer.

sition of the above partial differential equation yields:

$$C(z,t) = \sum_{m=0}^{\infty} A_m e^{-k_m^2 Dt} \sin(k_m z + \phi_m), \tag{3.10}$$

Since the electronic density $\rho_e(z,t)$ is linearly proportional to $C(z,t)$, the expression for $\rho_e(z,t)$ would also be of the same form as Eq. (3.10). By the kinematic theory of diffraction, the intensity of the mth satellite $I_m(t)$ in the SAXD spectrum will be proportional to the square of the mth Fourier component of $\rho_e(z,t)$ which can be expressed mathematically as:

$$I_m(t) \propto A_m^2 e^{-2k_m^2 Dt}. \tag{3.11}$$

Thus, the rate of decay of the log of satellite intensities with annealing time would be given by:

$$\frac{\partial \ln I_m}{\partial t} = -\frac{8\pi^2 m^2}{d^2} D. \tag{3.12}$$

Analysis leading to Eq. (3.12) assumes Fickian diffusion which does not include contributions to free energy from the concentration gradients at the interface. If the period of the multilayer is small enough[21], the diffusion constant for the multilayer may not necessarily be the same as the bulk diffusion constant. When gradient energy contributions are important, it is wavelength dependent as given by[21]:

$$D_{\lambda,m} = D\left(1 + \frac{2\kappa}{g''}k_m^2\right), \tag{3.13}$$

where κ is the gradient energy coefficient, g'' is the second spatial derivative of the free energy per unit volume, and D is the bulk diffusion constant. Both κ and g'' can be estimated using the regular solution model[21]. Using the heat of mixing for the Ni/Ta and Fe/Ta systems, as calculated by Miedema *et al.*[22], we found that $D_{\lambda,1} = 0.995D$ for $d = 100$ Å. Thus, Fickian diffusion is a good approximation for the $Ni_{80}Fe_{20}$/Ta system for multilayers with periods $d > 100$ Å.

3.3 Concurrent Grain Growth and Grain Boundary Diffusion

The standard analysis for interdiffusion in multilayers as discussed in the previous section is appropriate when the diffusion mechanism is dominated by bulk lattice diffusion. However, in polycrystalline films, grain boundary diffusion is generally the dominant diffusion mechanism at lower temperatures. Consider a thin film of composition A with a columnar-grained microstructure, which is modeled for simplicity as an array of close-packed hexagons so that the hexagon extremal cross section is twice the grain radius r and height

equal to film thickness d, as shown in Fig. 3.5. If the grain-boundary width is δ, and the film of composition A has interfaces to films of composition B on top and bottom, then the grain-boundary area in the plane of the film per grain, defined as the grain-boundary density, to first order is $6r\delta/3r^2$. If temperature is low enough such that lattice diffusion is negligible compared to grain-boundary diffusion, then the appropriate diffusion constant D of Eq. (3.12) is the grain-boundary diffusion constant D_{gb}, weighted by the grain-boundary density:

$$D = D_{gb}\frac{2\delta}{r}. \tag{3.14}$$

However, the analysis is further complicated by the possibility of concurrent grain growth which decreases the grain-boundary density. Grain growth kinetics in thin films typically obey the semiempirical relationship[11]:

$$r^n(t) - r^n(0) = \alpha e^{-Q_{gbm}/kT}t \equiv A(T)t, \tag{3.15}$$

where $r(t)$ is the mean grain size at time t, $r(0)$ is the initial mean grain size, α is a weakly temperature-dependent constant, n is typically in the range of 2-4, and Q_{gbm} is the activation energy for grain boundary migration. The kinetic models for grain growth typically imply a value of 2 for the exponent n in the case of two-dimensional normal grain growth. However, in thin films, grain growth is typically saturated, i.e., undergoes a rapid reduction in growth rate as the grain size approaches the layer thickness[11]. The specific causes for this saturation are complex and are often material-dependent but may be significantly related to grain-boundary grooves in the columnar structure. As a consequence, the experimental data fits better to an exponent in the

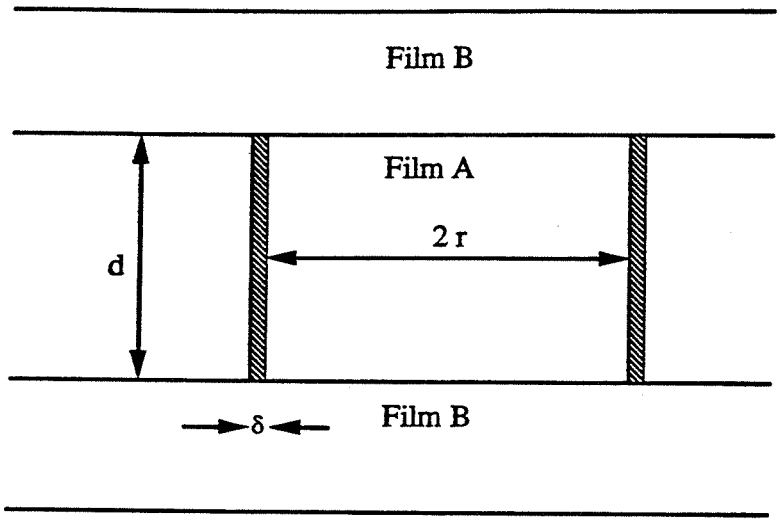

(a)

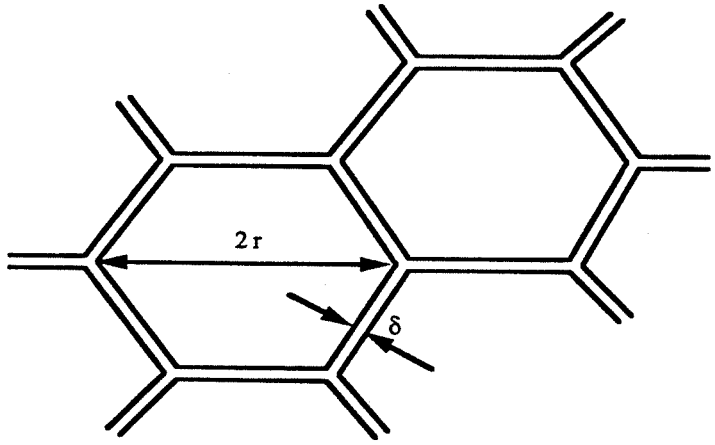

(b)

Figure 3.5: Schematic of a columnar-grained thin film shown in (a) cross section and (b) plan view for modelling of grain-boundary diffusion concurrent with grain growth.

range of n =3-4 at later times. Assuming that the grain-boundary density decreases due to grain growth as given by Eq. (3.15), the appropriate diffusion equation for this problem is:

$$\frac{[r^n(0)+A(T)t]^{1/n}}{2\delta}\frac{\partial C(z,t)}{\partial t}=D_{gb}\frac{\partial^2 C(z,t)}{\partial z^2}. \tag{3.16}$$

Equation (3.16) can be solved using separation of variables and Fourier decomposition in the spatial variable z, analogously to Eq. (3.9). The solution can be written as:

$$C(z,t)=\sum_{m=0}^{\infty}A_m\exp\left[-(\frac{n}{n-1})k_m^2\frac{2D_{gb}\delta}{A(T)}(r^n(0)+A(T)t)^{1-\frac{1}{n}}\right]\cos(k_m z+\phi_m). \tag{3.17}$$

The time dependence of the resulting mth satellite intensity I_m will then be:

$$I_m(t)\propto\exp\left[-2k_m^2\frac{n}{n-1}\frac{2D_{gb}\delta}{A(T)}(r^n(0)+A(T)t)^{1-\frac{1}{n}}\right]. \tag{3.18}$$

Hence, the rate of decay of $\ln I_m(t)$ becomes:

$$\frac{\partial \ln I_m}{\partial t}=-\frac{16\pi^2 m^2}{d^2}\frac{D_{gb}\delta}{r(t)}. \tag{3.19}$$

Comparing Eq. (3.19) with Eq. (3.12), note that D has been replaced by $2D_{gb}\delta/r(t)$ which is a time-dependent diffusion constant.

3.4 Interdiffusion Kinetics of Polycrystalline $Ni_{80}Fe_{20}$/Ta Multilayers

Small angle x-ray diffraction was used to study interdiffusion in multilayers which were annealed at various temperatures in the range $300-600°C$. As

the decay rate of the log of satellite intensity is proportional to m^2, as given by Eq. (3.12), the higher satellites are more sensitive to interdiffusion at lower temperatures. The decay of higher satellites for short period multilayers can be used to measure interdiffusion lengths of a few angstroms. Figure 3.6 shows the integrated first satellite intensity versus cumulative annealing time at various temperatures. No change in any of the satellite intensities was observed at 300°C. As shown in Fig. 3.6, there was no significant change in the first satellite intensity also at 375°C. However, we were able to characterize interdiffusion at this temperature from the decay of the higher order satellites (see Fig. 3.7). As can be seen from Fig. 3.6, the satellite intensities do not have a constant decay rate, as predicted by analysis of Ref.[7]. A better fit to the data, superposed as dashed lines in Fig. 3.6, was obtained using the model described above for concurrent grain growth and grain boundary diffusion. Quantative analysis of grain growth in polycrystalline multilayer films is complicated by the superposition of the microstructure of the individual layers when imaged in plan view or cross-section electron microscopy. As a result, evidence for grain growth in the temperature range $300 - 600$°C was also obtained from investigation of single layer $Ni_{80}Fe_{20}$ thin films which were annealed in high vacuum and analyzed by plan view TEM. The mean grain size in these studies was calculated by averaging over up to 100 grains contained in bright field TEM micrographs. Although this type of grain growth analysis is not as desirable as analysis of the multilayers themselves, the results for grain growth in single layer films are qualitatively consistent with observations of increased grain size in the thin regions of multilayer cross sections as well as the grain size analysis being significantly more straight-

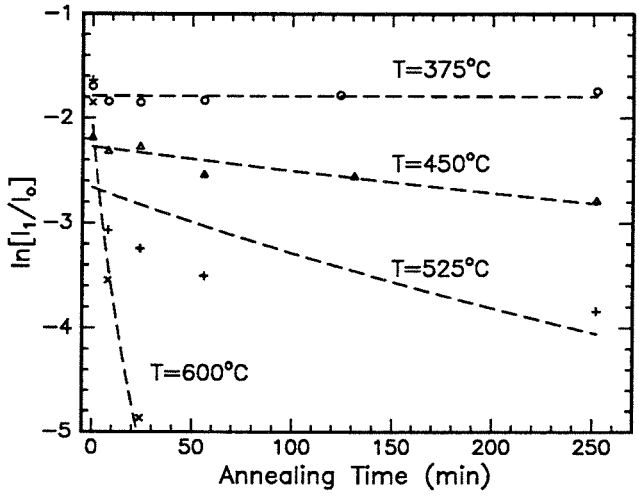

Figure 3.6: Variation of first satellite intensity with cumulative annealing time at various temperatures and fit to decay of satellite intensities using model for concurrent grain growth and grain-boundary diffusion.

forward in single layer than in multilayered thin films.

Assuming parabolic grain growth kinetics (n=2), Eq. (3.18) becomes

$$\ln\frac{I_m(t)}{I_o} = -\frac{16\pi^2 m^2}{d^2} D \frac{r^2(0)}{A(T)} \left[1 + \frac{A(T)t}{r^2(0)}\right]^{1/2}, \tag{3.20}$$

where I_o is the constant of integration chosen so that $I_m(t = 0)$ computed from the above equation matches the experimentally observed mth satellite intensity at t=0. Using Eq. (3.20), a fit was done to the decay of observed satellite intensities, as shown in Fig. 3.6, to calculate D. The initial grain size $r(0)$ and α were calculated from grain growth analysis of single layer $Ni_{80}Fe_{20}$ films and were found to be 60.37 Å and 5.24×10^{-15} cm^2/s, respectively. Based on this analysis, the activation energy for grain boundary migration, Q_{gbm}, for single layer $Ni_{80}Fe_{20}$ films was found to be 0.55 ± 0.11

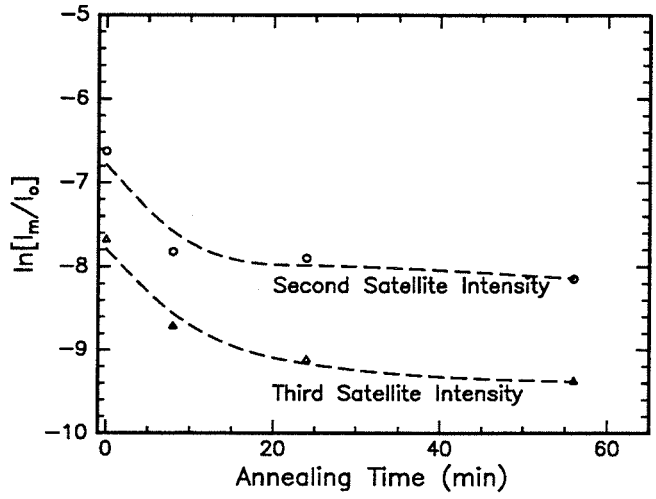

Figure 3.7: Variation of second and third satellite intensities vs. cumulative annealing time at 375°C. Dashed lines are guides to the eye.

eV. An Arrhenius plot of D, shown in Fig. 3.8, yielded the following diffusion coefficient and activation energy:

$$D_o = 1.70 \times 10^{-9} \text{ cm}^2/\text{s} \qquad Q = 1.28 \pm 0.26 \text{ eV}.$$

No information on Ta lattice diffusion in $Ni_{80}Fe_{20}$ or vice versa was available. However, the following diffusion constants for lattice self-diffusion in Ni[18] and Ta[19] are known from previous studies:

$$\text{Ni:} \qquad D_o = 1.30 \text{ cm}^2/\text{s}, \quad Q_l = 2.27 \text{ eV},$$

$$\text{Ta:} \qquad D_o = 0.124 \text{ cm}^2/\text{s}, \quad Q_l = 4.2 \text{ eV}.$$

Typically, the activation energy for grain boundary diffusion is significantly less than that for lattice diffusion ($Q_{gb} \approx 0.4 - 0.7 Q_l$ for most metals[20]).

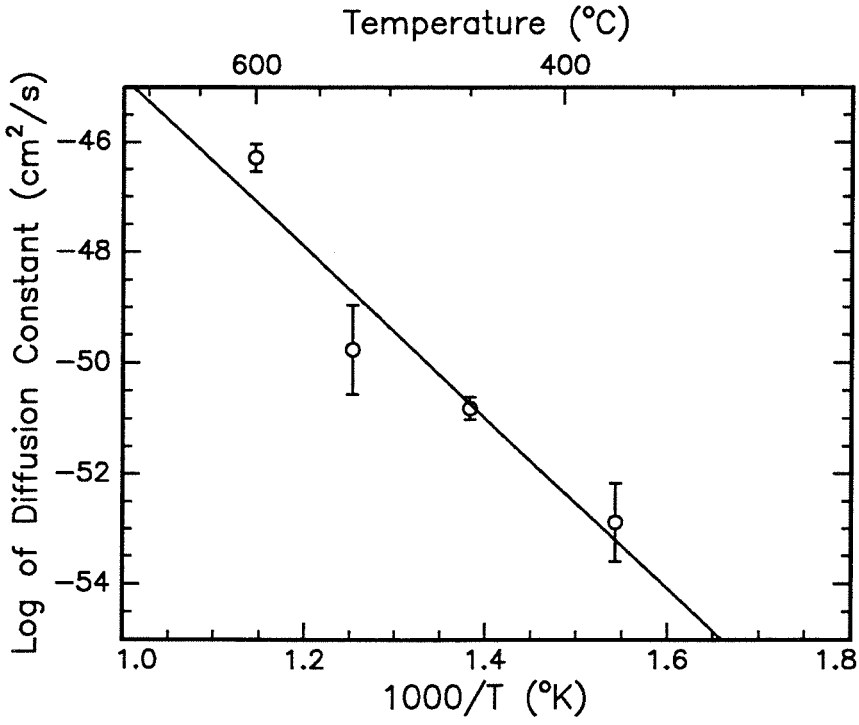

Figure 3.8: Arrhenius plot of D with temperature to estimate activation energy and preexponential for interdiffusion.

Comparing activation energies for lattice diffusion to the experimentally observed activation energy agrees with our assumption that the interdiffusion mechanism is grain-boundary diffusion. The relatively small value of the pre-exponential found experimentally can be explained by the fact that D has been weighted by the grain-boundary density.

Depending upon deposition conditions, different investigators have reported the as-deposited Ta film to be amorphous, *bcc* (α) or metastable tetragonal (β) phase. TEM analysis of the as-deposited Ta/$Ni_{80}Fe_{20}$ multilayers by us suggested that the Ta film was nanocrystalline with possibly some amorphous regions (see Fig. 3.9(a) and 3.10). However, presence of many *bcc* Ta crystalline peaks in the high angle x-ray diffraction spectrum shown in Fig. 3.11(a) suggests that the Ta film is not amorphous.

Comparison of high angle x-ray diffraction spectra of as-deposited and annealed multilayers, shown in Fig. 3.11, indicate that the *bcc* Ta crystalline peaks were broadened after a 4 h anneal at 525°C, which might suggest a diminishing crystal size due to grain boundary mediated solid-state amorphization. However, the persistence of *bcc* Ta crystalline peaks in the x-ray spectrum and the polycrystalline nature of the $Ni_{80}Fe_{20}$ film, as evidenced by the micrograph of Fig. 3.9, suggest that a solid-state amorphization reaction may have begun but has not resulted in transformation of a significant fraction of the Ta film. In this temperature regime, a solid-state amorphization reaction (SSAR) between Ni and β-Ta multilayers was indeed reported by Hollanders *et al.*[23] for Ni/Ta multilayered films. However, in case of their multilayers, the Ta layer had a greater thickness than the Ni layer. It is plausible that led to a faster SSAR than in case of our Ta/$Ni_{80}Fe_{20}$ multilay-

ers. Solid-state amorphization typically precedes nucleation of a crystalline intermetallic compound phase[9] whose presence was not observed in high angle x-ray diffraction spectra after annealing the Ta/$Ni_{80}Fe_{20}$ multilayers at 525°C. It is possible that some regions in the $Ni_{80}Fe_{20}$ film have begun to be amorphized due to Ta accumulation at the grain-boundaries and at higher temperatures would have been replaced by the intermetallic compound Ni_3Ta whose presence was reported by Hollanders *et al.*[23].

Comparison of the bright field micrographs of an as-deposited multilayer and another after annealing at 525°C for 4 h, as shown in Fig. 3.9, indicates that the $Ni_{80}Fe_{20}$-Ta interface is roughened and more diffuse after annealing at 525°C. No quantitative information about the diffusion constants for the different constituents could be obtained from just this analysis. However, evolution of magnetic properties, as discussed below, suggests that there is accumulation of Ta at $Ni_{80}Fe_{20}$ grain boundaries. This is consistent with our diffusion kinetics analysis which suggests grain boundary diffusion as the mechanism for interdiffusion. The enhanced contrast at $Ni_{80}Fe_{20}$ grain boundaries in the bright field micrographs of multilayer annealed at 525°C, might suggest that $Ni_{80}Fe_{20}$ grain boundaries are Ta rich. As the magnetic properties of the multilayer may not be as sensitive to outdiffusion of Ni and Fe into Ta as to Ta diffusion into Ni-Fe, that possibility cannot be ruled out. However, interdiffusion studies of Ta/Ni bilayers using Rutherford backscattering (RBS) by Kellock *et al.*[24] also lends supports to the grain boundary diffusion of Ta into Ni. In particular, they observed a Ta surface peak in the RBS spectrum after an anneal at 350° for 32 hours, when the Ta layer was located beneath 100 nm of Ni. This was not observed to be the case

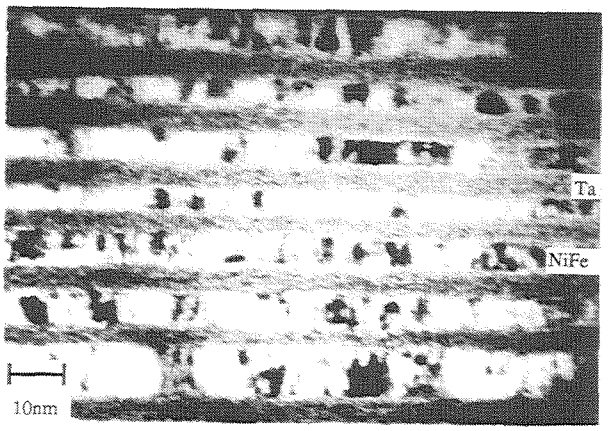

(a)

(b)

Figure 3.9: (a) Bright field cross-sectional transmission electron micrograph of as-deposited multilayer (15×128 Å) and (b) after annealing at 525°C for 4 h.

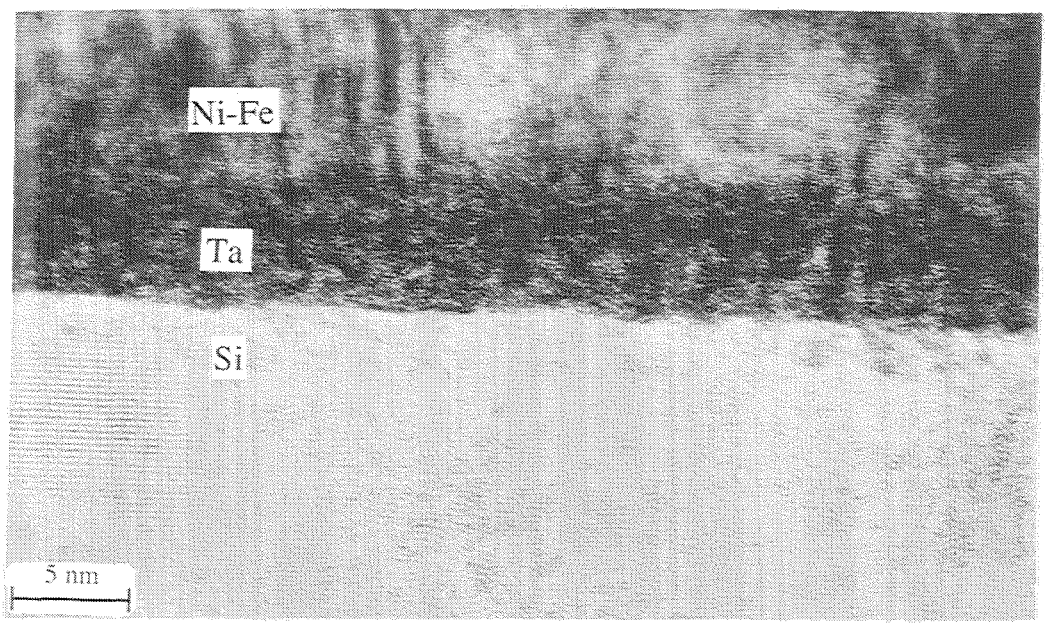

Figure 3.10: High resolution cross-sectional transmission electron micrograph of $Ni_{80}Fe_{20}$/Ta multilayer as deposited on Si(111).

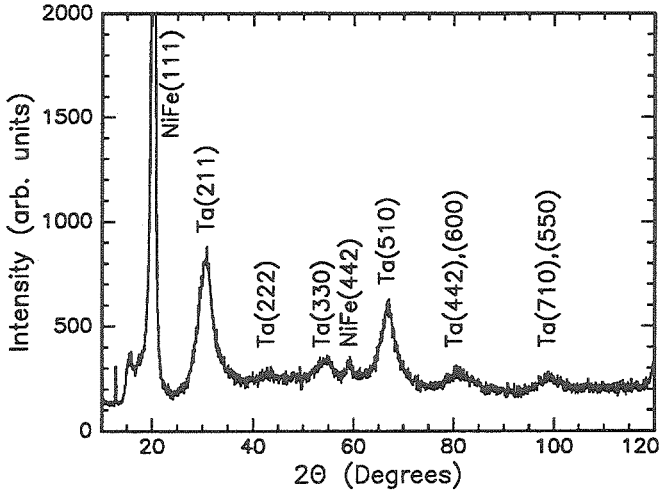

(a)

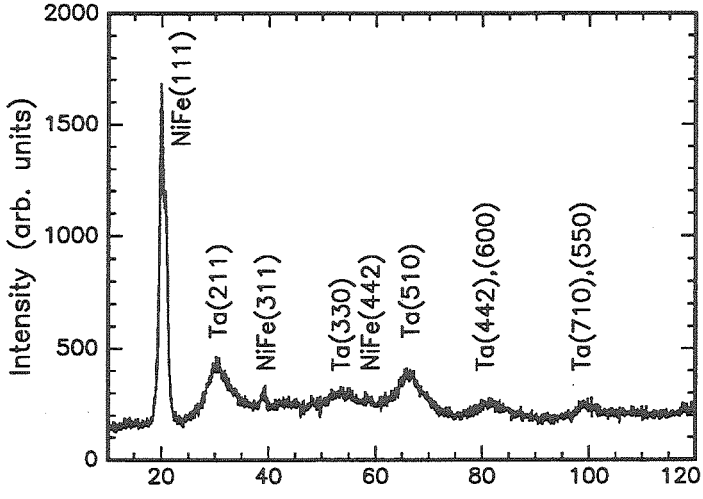

(b)

Figure 3.11: (a) High angle x-ray diffraction spectra using Mo K_α radiation of as-deposited $Ta/Ni_{80}Fe_{20}$ multilayer and (b) after annealing at 525°C for 4 h.

for the Ni peak when 100 nm of Ta was located on top, indicating that at lower temperatures Ta diffusion (presumably due to grain-boundaries) was higher than that of Ni.

3.5 Evolution of Magnetic Properties

B-H loop measurements were made for the as-deposited Ta/$Ni_{80}Fe_{20}$ multilayer after thermal annealing at 300, 375, 450 and 525°C for 4 h. The coercivity of the as-deposited multilayer was 0.5 Oe, and increased to 6.5 Oe after annealing at 525°C. The coercivity is plotted vs interdiffusion length, which is calculated directly from the decay of the first satellite with annealing, in Fig. 3.12(a). The $4\pi M_s$ measurement of the as-deposited multilayer indicated an average magnetic thickness of 53.9 Å/period, implying that 30.1 Å/period was nonmagnetic. This suggests the presence of a nonmagnetic $Ni_{80}Fe_{20}$ with an average thickness of 15 Å at each interface possibly due to intermixing with Ta during the deposition process. The B-H loops for the as-deposited multilayer were found to be isotropic, so H_k could not be measured. However, single layer $Ni_{80}Fe_{20}$ films with thicknesses equal to or greater than 100 Å, under the same deposition conditions, were found to have well-defined easy and hard axes. The disappearance of induced uniaxial anisotropy for ultrathin $Ni_{80}Fe_{20}$ films has also been reported elsewhere[25].

After annealing at 300°C, the change in $4\pi M_s$ of the multilayer was less than 0.5%. This is consistent with the interdiffusion data, as no change in satellite intensities was observed at 300°C. At higher temperatures, $4\pi M_s$ dropped sharply, as shown in Fig. 3.12(b). For multilayers annealed at 450°C

and higher temperatures, the field required to saturate the magnetization increased dramatically. A field greater than 100 Oe was required to saturate the multilayer annealed at 525°C. This is also illustrated by the variation of B_r/B_s with interdiffusion length in Fig. 3.12(c). The transition from soft to hard magnetic properties can also be understood in terms of our analysis of interdiffusion data, if it is assumed that accumulation of Ta at $Ni_{80}Fe_{20}$ grain boundaries results in a microstructure consisting of ferromagnetic $Ni_{80}Fe_{20}$ particles embedded in a nonmagnetic Ta-$Ni_{80}Fe_{20}$ matrix. As the thickness of this nonmagnetic matrix increases, the coupling between the magnetic particles decreases, thus requiring higher saturating fields. Thus the magnetic microstructure evolves from soft, magnetically continuous layers of $Ni_{80}Fe_{20}$ to isolated $Ni_{80}Fe_{20}$ nanometer-scale particles. It is interesting to note that similar B-H loop characteristics have been reported in work on a photolithographically defined array of micron-sized $Ni_{80}Fe_{20}$ particles as the interparticle spacing increases [26], although it should be pointed out that the magnetic length scales in these two experiments are quite different. More recently, short period Ag/NiFe multilayers were annealed to prepare granular films of Ag with embedded $Ni_{80}Fe_{20}$ particles, for magnetoresistive applications[27]. Silver, having a positive heat of mixing with both Ni and Fe[22], accumulated along the $Ni_{80}Fe_{20}$ grain-boundaries after annealing but did not diffuse farther into the $Ni_{80}Fe_{20}$ grains unlike the case of Ta/$Ni_{80}Fe_{20}$ multilayers. As a consequence, the magnetic moment of $Ni_{80}Fe_{20}$ was not reduced drastically and the magnetic properties remained relatively soft. The above work and our investigations illustrate that the evolution of film microstructure can be used to modify magnetic properties at the scale of the

grain size in $Ni_{80}Fe_{20}$ films.

3.6 Conclusions

Using small angle x-ray diffraction, interdiffusion lengths ranging from 5 to 40 Å were measured for $Ta/Ni_{80}Fe_{20}$ multilayers in the temperature range $300-600°C$. The interdiffusion kinetics suggest grain boundary interdiffusion concurrent with grain growth in $Ni_{80}Fe_{20}$. Evolution of soft magnetic properties is consistent with accumulation of Ta at the grain-boundaries of $Ni_{80}Fe_{20}$. Since soft magnetic properties of $Ni_{80}Fe_{20}$ are not as sensitive to outdiffusion of Ni or Fe into Ta, that possibility cannot be excluded. Significantly, the change in saturation magnetization of the $Ta/Ni_{80}Fe_{20}$ multilayer upon annealing at 300°C for 4 h was less than 0.5%. However, at temperatures higher than 375°C, the saturation field H_{sat} increased dramatically whereas $4\pi M_s$ decreased due to interdiffusion of Ta in $Ni_{80}Fe_{20}$. Grain-boundary diffusion of Ta into $Ni_{80}Fe_{20}$ possibly led to a microstructure consisting of isolated $Ni_{80}Fe_{20}$ particles embedded in a nonmagnetic matrix, thus increasing the field required to saturate the multilayer. The above hypothesis might be confirmed by high resolution analytical electron microscopy techniques in cross-section such as scanning transmission electron microscopy or electron energy loss spectroscopy work.

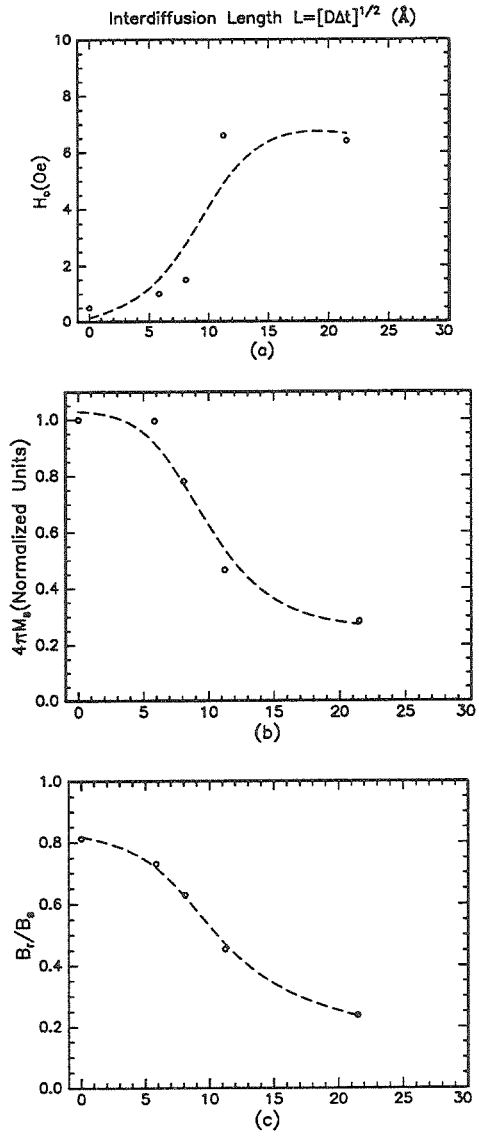

Figure 3.12: Variation of (a) H_c, (b) normalized $4\pi M_s$, and (c) B_r/B_s for $Ta/Ni_{80}Fe_{20}$ multilayer with interdiffusion lengths corresponding to 4 h anneals at 300, 375, 450, and 525°C. The dashed lines are guides to the eye.

Bibliography

[1] A.F. Mayadas and M. Shatzkes, Phys. Rev. B **1**, 1382 (1970).

[2] S. Krongelb, A. Gangulee, and G. Das, IEEE Trans. Magn. **9**, 568 (1973).

[3] R.L. Anderson, A. Gangulee, and L.T. Romankiw, J. Electron. Mater. **2**, 161 (1973).

[4] W.W. Mullins, J. Appl. Phys. **28**, 333 (1957).

[5] D.J. Srolovitz and C.V. Thompson, Thin Solid Films **139**, 133 (1986).

[6] L.G. Chow, S.K. Decker, D.J. Pocker, G.C. Pendley, and J. Papadopoulos, IEEE Trans. Magn. **15**, 1833 (1979).

[7] F. Spaepen, Mater. Res. Soc. Symp. Proc. **37**, 207 (1985).

[8] P. Hansen, *Constitution of Binary Alloys*, (McGraw-Hill, New York, 1958), p. 1045.

[9] R.W. Johnson, C.C. Ahn, and E.R. Ratner, Phys. Rev. B **40**, 8139 (1989).

[10] R.M. Bozorth, *Ferromagnetism*, (Van Nostrand, Amsterdam, 1957), p. 823.

[11] C.V. Thompson, Annu. Rev. Mater. Sci. **20**, 245 (1990).

[12] L.M. Goldman, H.A. Atwater, and F. Spaepen, Proc. Mater. Res. Soc. **160**, 571 (1990).

[13] B.E. Warren, *X-ray Diffraction*, (Dover Publications, New York, 1990) p. 372.

[14] J.H. Underwood and T.W. Barbee, Jr., Applied Optics **20**, 3027 (1981).

[15] L.M. Goldman, Ph.D. Thesis, Harvard University, 1990.

[16] D.G. Stearns, J. Appl. Phys. **65**, 491 (1989).

[17] A.P. Payne and B.M. Clemens, Phys. Rev. B **47**, 2289 (1993).

[18] R. Hoffman, F. Pickus, and R. Wood, Trans. AIME **206**, 483 (1956).

[19] N.L. Peterson, in *Solid State Physics*, edited by F. Seitz, D. Turnbull, and H. Ehrenreich, (Academic, New York, 1968), Vol. 22.

[20] P.G. Shewmon, *Diffusion in Solids*, (J. Williams Book Company, Jenks, 1983), pp. 164-175.

[21] J.W. Cahn and J.E. Hilliard, J. Chem. Phys. **28**, 258 (1958)

[22] A.R. Miedema, F.R. de Boer, and R. Boom, *CALPHAD*, (Permagon, New York, 1977), Vol. 1, pp. 341-359.

[23] M.A. Hollanders, C.G. Duterloo, B.J. Thijsse, and E.J. Mittemeijer, J. Mater. Res. **6**, 1862 (1991).

[24] A.J. Kellock, J.E.E. Baglin, K.R. Coffey, J.K. Howard, M.A. Parker, and D.L. Neiman, Mater. Res. Soc. Symp. Proc. Vol. **343**, in press.

[25] M. Goto, H. Tange, and T. Kamimori, J. Magn. Magn. Mater. **62**, 251 (1986).

[26] J.F. Smyth, S. Schutz, D. Kern, H. Schmid, and D.Yee, J. Appl. Phys. **63**, 4237 (1988).

[27] T.L. Hylton, K.R. Coffey, M.A. Parker, and J.K. Howard, Science **261**, 1021 (1993).

æ

Chapter 4

Epitaxial Growth of Cu on Si at Room Temperature

4.1 Introduction and Motivation

The growth of single-crystal copper films on silicon is potentially of great technological interest both as a convenient template for the preparation of other metallic films in magnetic thin film applications, and as an interconnect material for future large-scale integrated circuits[1]. Recently, considerable controversy had surrounded reports of growth of epitaxial Cu films on Si. Successful epitaxy of Cu (001) on Si (001) was reported for growth in vacuum systems with base pressures in the high-vacuum range[2, 3], but the analysis of microstructure was limited to x-ray diffraction in conventional $\theta - 2\theta$ geometry and ion channeling. On the other hand, surface science investigations employing photoelectron holography[4] indicated the absence of (001) epitaxial growth on Si(001) 2×1 structures under ultrahigh vacuum conditions[4]. Furthermore, there were conflicting reports of silicide formation upon deposition of Cu on Si at low temperatures (0-100°C). Walker

et al.[5, 6] reported η-Cu_3Si formation upon deposition at 100°C of Cu on Si(111) which aided the establishment of an epitaxial relationship between Cu and Si. Ichinokawa *et al.*[7] observed an intermixed layer of Cu and Si at room temperature deposition on Si(001) 2×1 surface. Also, Sosnowski *et al.*[8], who used ionized cluster beam deposition at room temperatures, did not find any evidence for an interfacial reaction between Cu and Si. The kinetics of silicide phase formation in Cu-Si diffusion couples in the temperature range 200 – 260°C was investigated by Hong *et al*[9]. Harper *et al.*[10] reported an epitaxial relationship between Cu_3Si and Si(001) which was formed upon deposition of Cu on Si(001) at 200°C by dc magnetron sputtering. This silicide phase catalyzed a remarkably rapid oxidation of Si at room temperature, leading to the formation of over one micron thick buried SiO_2/Si(001). The purpose of this investigation was to resolve some of these controversies, and to show how orientation and microstructure develop during epitaxial growth of Cu on Si (001).

4.2 Substrate Preparation and Deposition Conditions

Prior to sample insertion into the vacuum system, samples were cleaned by sequential chemical oxidation in a 5:1:1 solution of H_2O:HCl:H_2O_2 at 80°C, followed by etching in a buffered HF solution. Upon insertion into the sputtering system chamber, reflection high energy electron diffraction (RHEED) was used to confirm (1 x 1) surface reconstruction of the (001) Si that is commonly observed on HF-dipped Si (001), and which corresponds to

dihydride termination of the surface[11]. This surface is stable in air for up to an hour and for 10 hours or so in vacuum, depending upon the residual gases present in vacuum. Upon heating to $\sim$ 370°C, this surface transforms to a monohydride (2 x 1) surface. Futhermore, the H-terminated Si(1 x 1) surface has the same structure as bulk Si and is different from the (2 x 1) reconstructed Si(001) surface obtained after desorbing the native oxide *in situ* at 1200°C. It is plausible that the different film morphologies obtained for Cu growth on Si by different investigators may be due to different Si surface structure and reconstruction prior to deposition of Cu. The as-inserted Si (001) substrates were heated to T= 200°C for approximately two hours and cooled to room temperature at a cooling rate of 3°C/minute, prior to sputter deposition of Cu. This pre-deposition bake is carried out to desorb any possible residual moisture and hydrocarbons on the surface, the effectiveness of which is supported by reflection electron energy loss spectrometry work done in our group[12]. See Appendix A for more details of the substrate cleaning and deposition conditions which affected the Cu epitaxy.

Films were grown at room temperature in the ultrahigh vacuum ion-beam sputtering system described in Chapter 2. The deposition rate was approximately 0.10 nm/s and the background Ar pressure during sputtering was 2×10^{-4} torr. The film thickness, estimated during growth using an oscillating-crystal thickness monitor, was confirmed afterwards with Rutherford backscattering spectometry. The purity of the Cu film was confirmed using electron microprobe analysis which indicated less than 0.2 at. % Ar and no other metallic impurities.

4.3 *In Situ* Electron Diffraction Analysis

In situ RHEED measurements indicated that the [100] and [110] in-plane azimuths were parallel to [110] and [100] azimuths of Si, respectively, and are shown in Fig. 4.2(b). The lattice mismatch for the orientation Cu[100] || Si[110] is 6% as opposed to 33% when the two unit cells are parallel. Information about the evolution of the film microstructure during growth was obtained using *in situ* RHEED measurements which were recorded on video and later analyzed to calculate the intensity profile across the Bragg rods (see Sec.2.4 for more details of this technique). As indicated by RHEED measurements shown in Fig. 4.3, during growth of the first 2 nm of copper, broad and diffuse Bragg rods corresponding to a nominally (001)-textured Cu film were observed. For thicknesses in the range 5-10 nm, the Bragg rod width gradually decreased whereas its intensity gradually increased with increasing Cu thickness. No significant changes in the RHEED features were observed for thicknesses greater than 20 nm. The change in the relative peak intensities of the 01 and $0\bar{1}$ satellites in Fig. 4.3 for thicknesses greater than 5 nm were due to variations in the sample alignment with respect to the electron beam during growth.

4.4 X-ray Analysis

Crystallographic texture of the Cu films on Si was assessed by the Inel thin film x-ray diffractometer as described in Chapter 2. Measurements were performed with incident beam angles in the range from 5°-45° in 5° intervals, along both the [100] and [110] azimuths of the Si surface. Fig. 4.1 shows

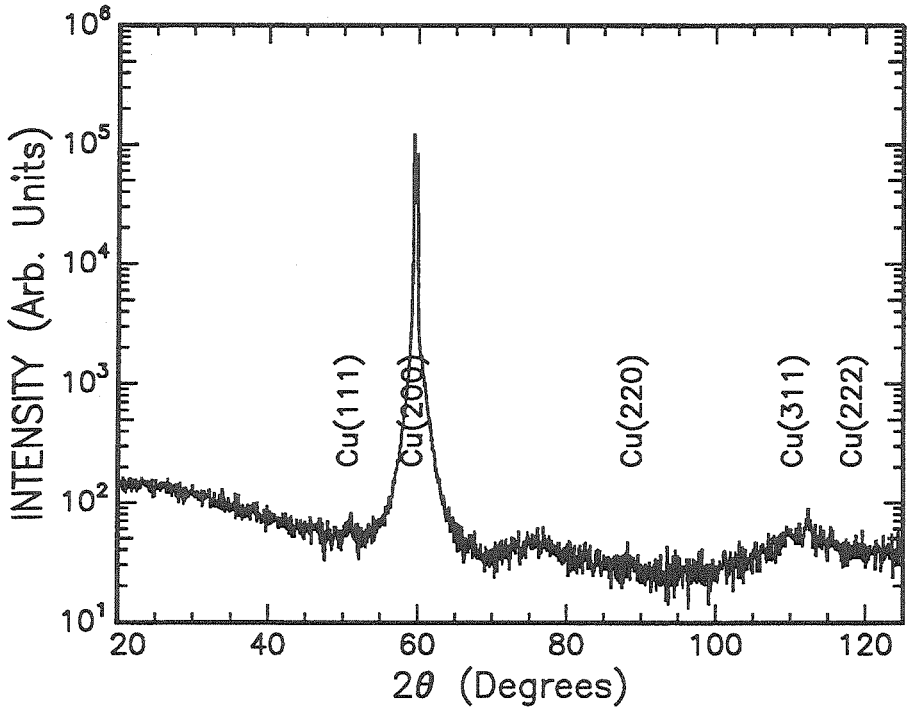

Figure 4.1: X-ray diffraction scan of epitaxial Cu (001) film on Si (001) deposited at room temperature for $\theta_i = 30°$.

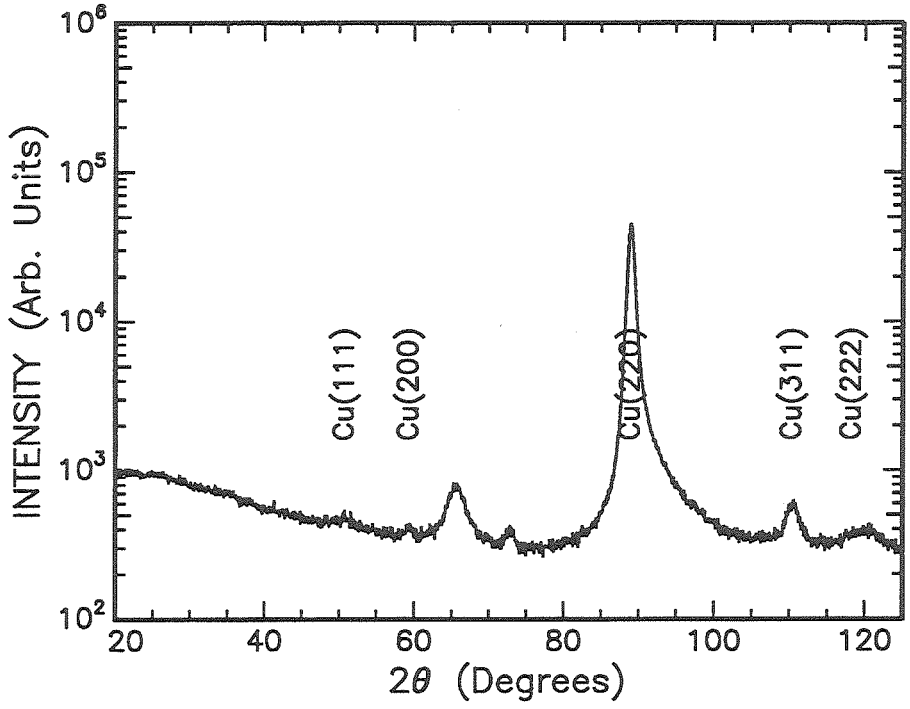

(a)

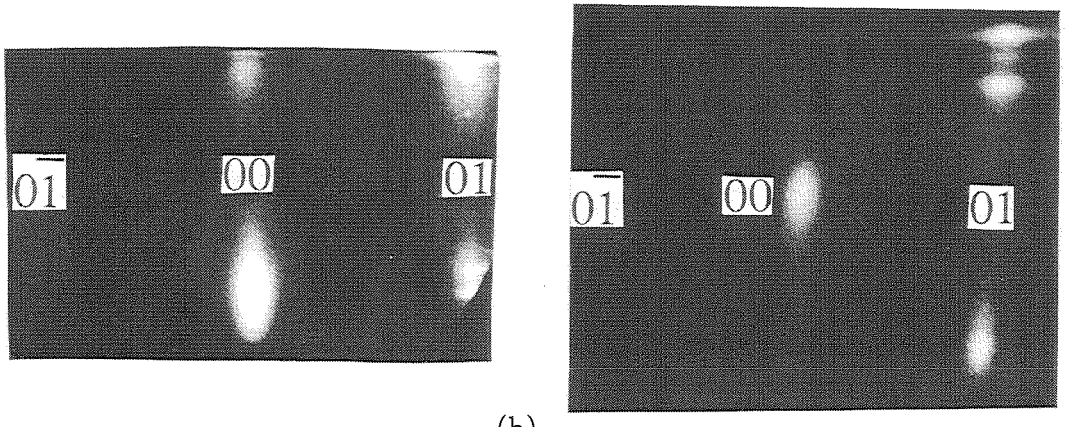

(b)

Figure 4.2: (a) Grazing incidence ($\theta \leq 5°$) x-ray diffraction scan of epitaxial Cu (001) film on Si (001) along [110] Si azimuth and (b) the RHEED patterns during film growth for [100] and [110] Cu azimuths.

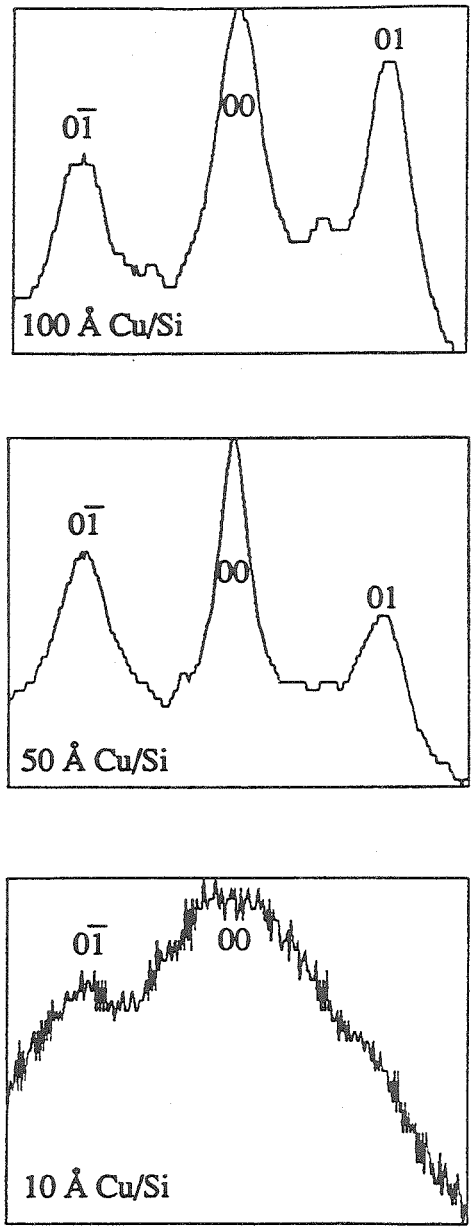

Figure 4.3: The intensity profile across RHEED patterns at various stages of Cu(001) film growth on Si(001).

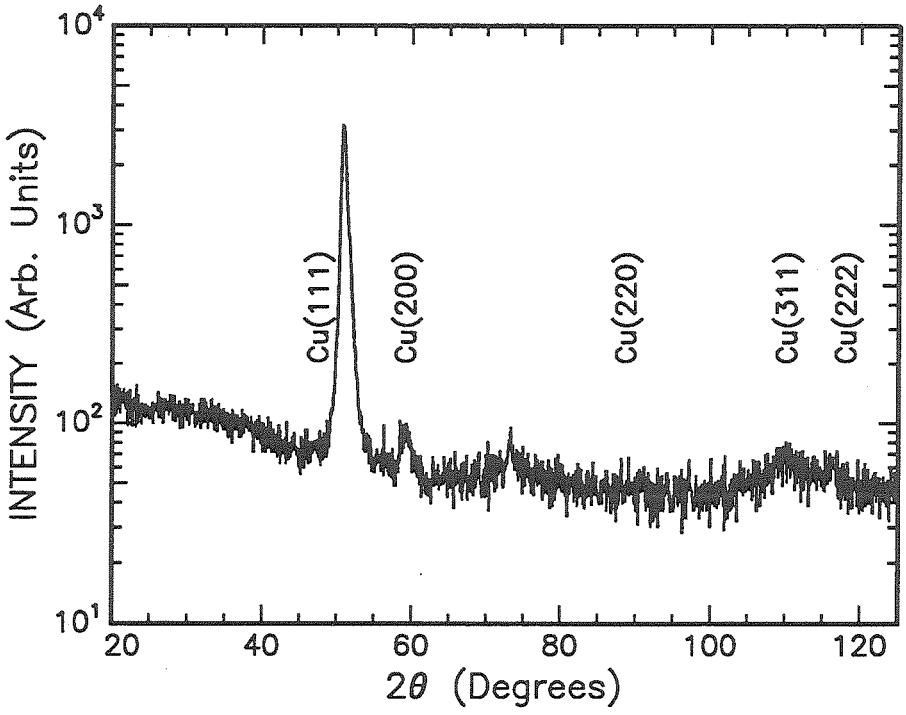

Figure 4.4: X-ray diffraction scan of (111)-textured polycrystalline Cu film on Si (001) for $\theta_i = 20°$.

the x-ray diffraction spectrum for $\theta_i = 30°$ which is equivalent to the more conventional $\theta - 2\theta$ x-ray scattering geometry. For Co K_α, 2θ for Cu(200) reflection is close to 60°. Therefore, this reflection should be much stronger than other reflections of *fcc* Cu, which is indeed the case, as shown in Fig. 4.1 for $\theta_i = 30°$. Other textures of fcc Cu, notably (111), are detectable though their intensity is 2-3 orders of magnitude smaller than (200). Fig. 4.2(a) illustrates a diffraction spectrum for grazing angle incident beam ($\theta_i \leq 5°$) along the [110] and [100] Si azimuths. In this geometry, the x-ray scattering vector is close to being in the plane of the sample, and hence, sensitive to the in-plane orientation of the film texture. For near-zero incident angle and Cu[100] azimuth, a strong Cu(220) reflection should be observed from an epitaxial Cu(001) film for Co-K_α radiation. As shown in Fig. 4.2(a), a strong Cu(220) reflection is indeed observed for this azimuth whereas for Si[100] azimuth, the reflection completely disappears, thus confirming the orientation Cu[100] || Si[110]. No reflections corresponding to copper silicide phases were detected for films deposited at room temperature. Room temperature-deposited Cu(001) films with very strong texture (i.e., competing texture fraction ≤ 0.005) exhibited no silicide formation even after annealing at 120°C for 2 hours. This is in disagreement with the kinetics of silicide formation reported by Hong *et al.*[9], as based on their kinetics for silicide growth, the thickness of the silicide would be 180 nm after annealing at 120°C for 1 hour. However, the kinetics they reported are for polycrystalline Si-Cu thin film couples. It is plausible that a kinetic barrier for silicide nucleation exists in well-oriented Cu(001) films on Si(001). Furthermore, a silicide was formed immediately upon deposition of Cu at 80°C. This was ev-

idenced by the absence of a Cu(001) RHEED pattern, the film being unlike in appearance to that of Cu, and identification of Cu_3Si peaks in its x-ray diffraction spectrum. This further supports the the possibility of a kinetic barrier for well-oriented Cu(001)/Si(001) films and that this barrier is either absent or smaller during the initial stages of film growth. For certain Cu films where trace metallic impurities such as Fe, Cr and Ni were detected by electron microprobe analysis in amounts 0.1-2%, polycrystalline films with strong (111) texture were obtained as indicated by x-ray diffraction spectrum of one such sample for $\theta_i = 20°$ shown in Fig. 4.4. Cross-sectional transmission electron microscopy studies of these films revealed an interfacial silicide less than 1 nm thick separating the columnar grains of (111)-oriented Cu film and Si substrate. In addition, Cu_xNi_{1-x} alloyed films grown directly on Si, with x=0.45 had a similiar (111)-textured columnar microstructure. It is plausible that the presence of impurities such as Ni, Fe and Cr catalyzes a thin interfacial silicide formation, which then promotes (111)-textured polycrystalline film growth. Furthermore, in another experiment a 50 nm thick Cu film was annealed at 230°C until it was completely consumed to form Cu_3Si as evidenced by RHEED. This was followed by deposition of another 50 nm of Cu film at room temperature. The film subsequently deposited was found to be polycrystalline with strong (111) texture. The above investigations suggest that if the Cu film growth proceeds with the formation of an interfacial silicide due to presence of impurities or due to deposition at higher temperatures, then (001) epitaxial growth might be inhibited. It is possible that some of the investigators did not observe Cu epitaxy on Si due to one of the above reasons, in particular, possibly because typically in

vacuum systems, the true substrate temperature is not accurately measured due to bad thermal contact.

4.5 Electron Microscopy Analysis

Transmission electron microscopy was done using a Philips EM430 microscope operating at 300 keV, as described earlier and sample preparation was done using adhesives which did not require any high-temperature curing. The samples were ion-milled using Ar^+ at 77 K, 10 minutes prior to insertion into the microscope. A high resolution cross-sectional transmission electron micrograph of the Cu/Si interface along the [110] zone axis of Si, for room temperature-deposited sample, is shown in Fig. 4.5(a). The inset shows the [110] and [100] selected area diffraction pattern due to Si and Cu, respectively. The spots due to Cu are broader than those due to Si and have a mosaic spread of $\pm 5°$ about Si [110] zone axis. Furthermore, the interface is atomically sharp with no evidence of any interfacial silicide. Interestingly, Fig. 4.5(a) illustrates that grains with orientations other than (001) can be observed within the first 5 nm of Cu film, which is in agreement with x-ray analysis and RHEED observations. These grains are occluded during the early stages of Cu growth by grains of (001) orientation, eventually leading to a single crystal Cu(001) film after about 20 nm. This evolution of microstructure by occlusion is summarized in a schematic diagram (Fig. 4.5(b)) showing the distribution of orientations as obtained from the cross-sectional transmission electron micrograph shown in Fig. 4.5(a).

A nearly periodic strain field can be observed extending into the first 2-3

nm of Cu film as well as the Si substrate, as can be seen in the lower magnification cross-sectional electron micrograph shown in Fig. 4.6. The period of this strain field ($\cong$ 3 nm) agrees well with the periodicity of misfit dislocations corresponding to the 6% mismatch between Cu and Si for Cu[100] || Si[110]. Furthermore, this illustrates that some of the misfit strain is accomodated in the substrate as well, inconsistent with the assumption often made in the coherent thin film growth analysis that the substrate is perfectly rigid[13]. Extension of misfit strain fields into the substrate have also been observed for coherent island growth of Ge on Si[14]. See Chapter 5 for a more elaborate discussion of coherent film growth. It is possible that each strained region near the interface corresponds to a growing Cu island at the early stages of growth and these islands coalesced to form a columnar-grained film. Bright field XTEM analysis indicated a high density of defects in the film, as well as a polycrystalline copper oxide up to 20 nm thick at the Cu film surface, as shown in Fig. 4.7. As a consequence, when the Cu film is viewed in plan view (see Fig. 4.8), it appears polycrystalline due to the copper oxide grains. The faint circular rings due to the polycystalline copper oxide and the diffraction spots due to the Cu film can also be seen in the diffraction pattern shown in the inset of Fig. 4.8.

4.6 Conclusions

In conclusion, we have defined conditions for which Cu(001) epitaxy is possible on H-terminated Si(001) in ultra-high vacuum conditions. The RHEED, x-ray diffraction and electron microscopy results suggest that the mechanism

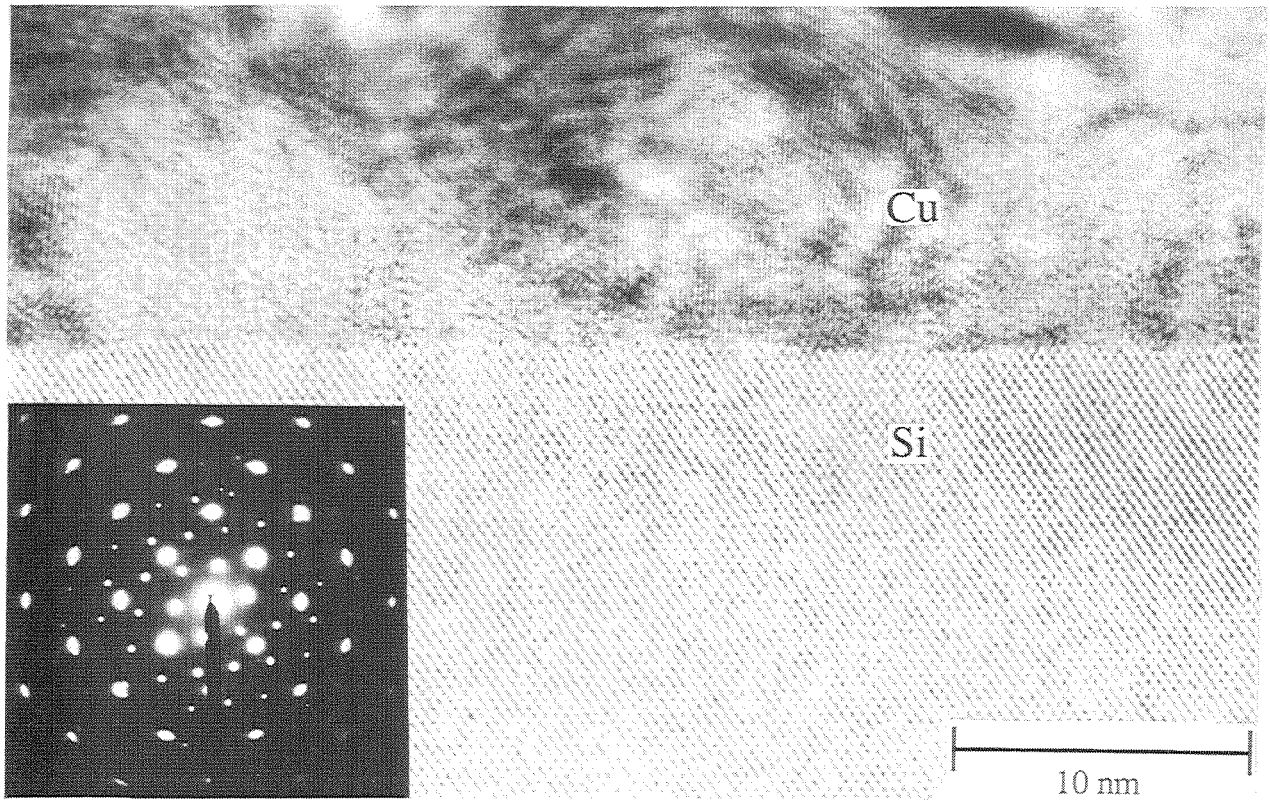

(a)

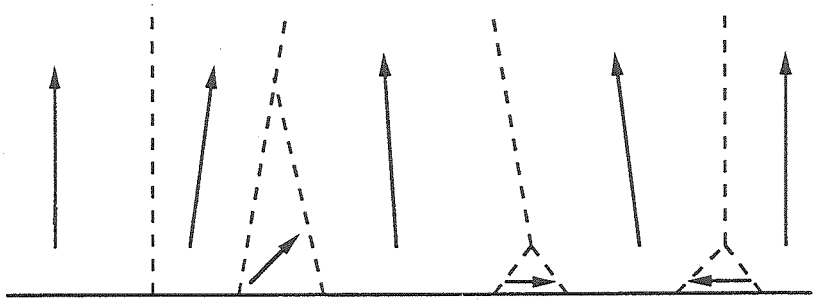

(b)

Figure 4.5: (a) High resolution cross-sectional transmission electron micrograph (XTEM), along [110] Si zone axis, of Cu film on Si. The Si [110] and Cu [100] selected area diffraction pattern is shown as inset. (b) Schematic showing microstructure evolution as obtained from high resolution XTEM image.

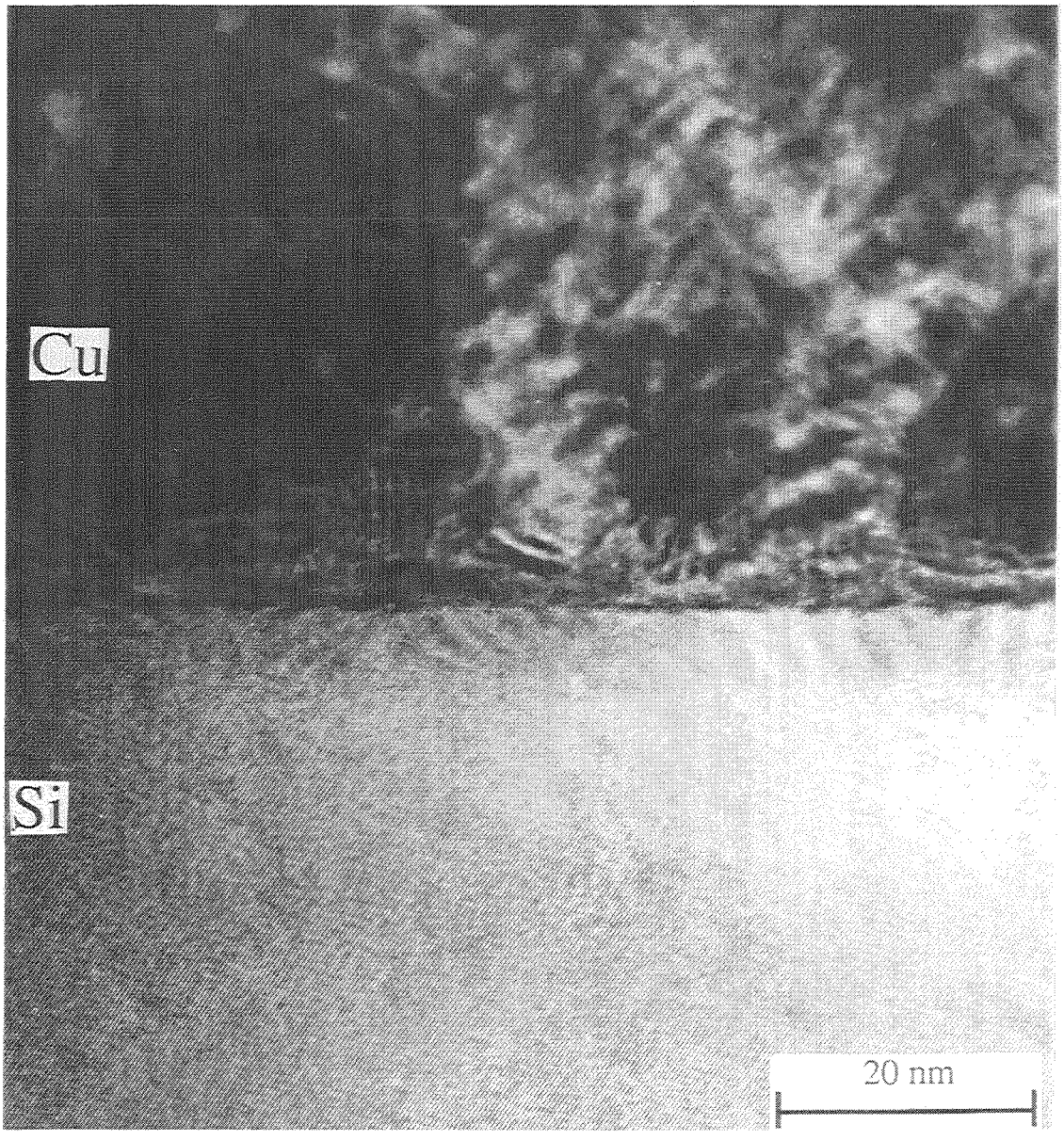

Figure 4.6: Lower magnification high resolution cross-sectional transmission electron micrograph of Cu film illustrating the misfit strain field extending into the Si substrate.

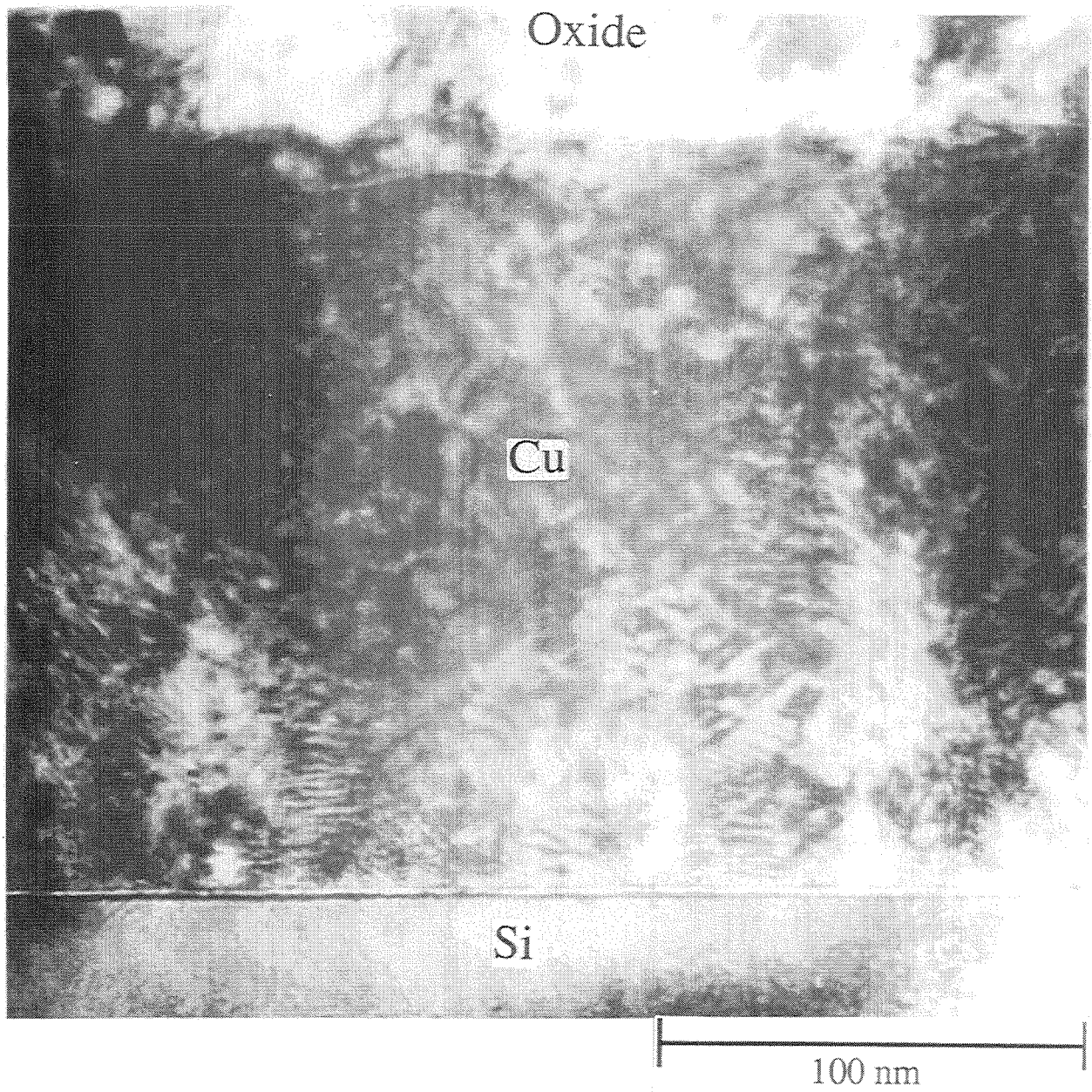

Figure 4.7: Bright field cross-sectional transmission electron micrograph of Cu film on Si, illuminating the defects in the film and the copper oxide.

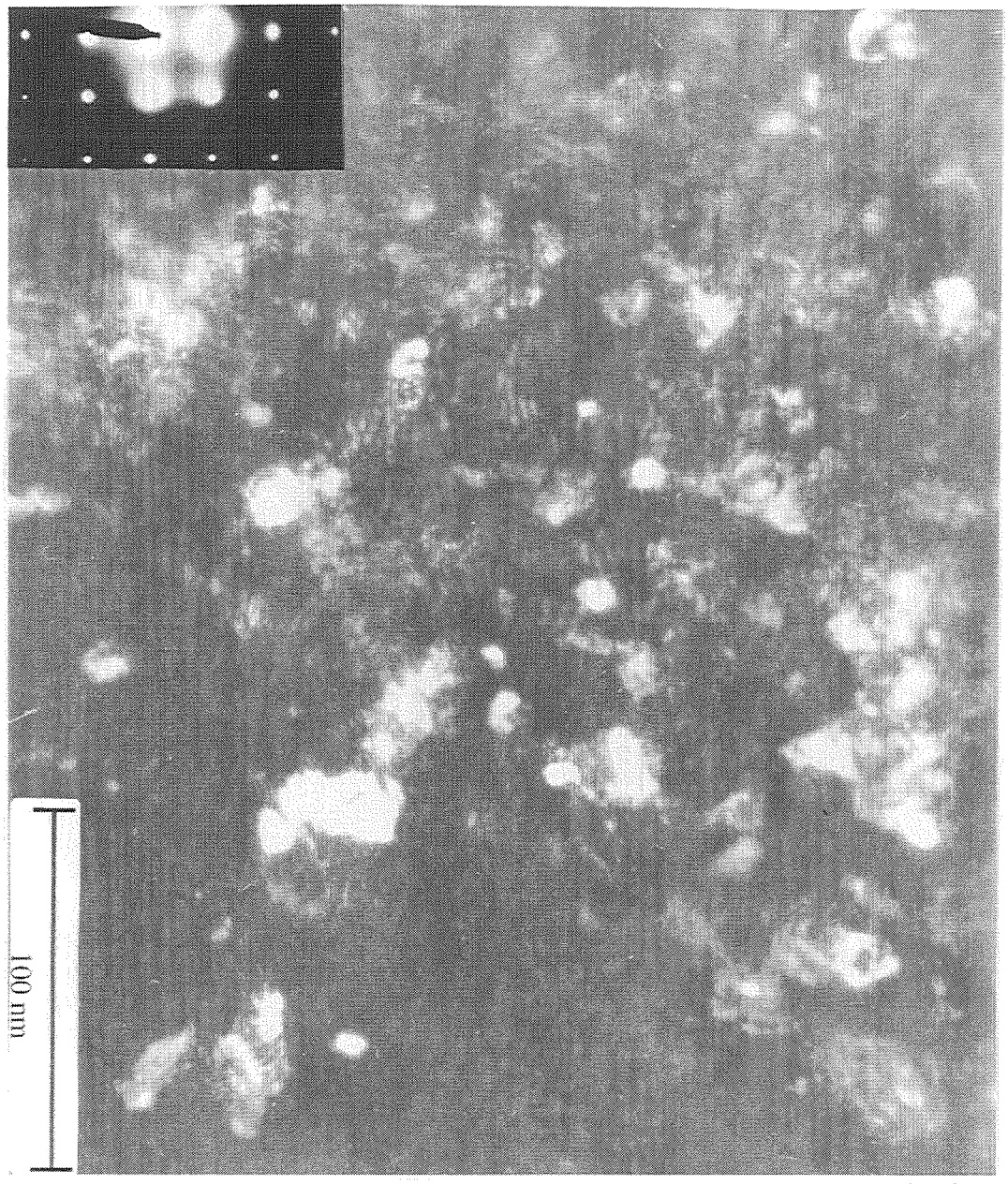

Figure 4.8: Plan view transmission electron micrograph of epitaxial Cu film with the diffraction pattern shown in inset.

for orientation development is an occlusion of grains misoriented with respect to (001) grains, eventually leading to a reduction in the mosiac spread of the columnar-grained structure. No evidence suggesting an interfacial silicide was found for room temperature (001) Cu film growth. However, for (111)-textured polycrystalline Cu films, an interfacial silicide was observed which inhibited Cu(001) epitaxy on Si(001). It is possible that a nucleation barrier for silicide formation exists for Cu(001) films grown epitaxially on Si(001) which might explain the absence of a silicide in these films, contrary to kinetics of silicide formation reported by other investigators[1, 9].

Bibliography

[1] J. Li, Y. Shacham-Diamand and J.W. Mayer, Mater. Sci. Rep. **9**, 1 (1992).

[2] C.A. Chang, Appl. Phys. Lett. **55**, 2754 (1989).

[3] J. Li and Y. Shacham-Diamand, J. Electrochem. Soc. **139**, L37 (1992).

[4] B.P. Tonner, J. Zhang, X. Chen, Z-L. Han, G.R. Harp, and D.K. Saldin, J. Vac. Sci. Technol. **B10**, 2082 (1992).

[5] F.J. Walker, E.D. Specht, and R.A. McKee, Phys. Rev. Lett. **67**, 2818 (1991).

[6] F.J. Walker, J.R. Conner, and R.A. McKee, Mat. Res. Soc. Symp. Proc. **187**, 249 (1990).

[7] T. Ichinokawa, T. Inoue, H. Izumi and Y. Sakai, Surface. Sci. **241** 416 (1991).

[8] M. Sosnowski, H. Usui and I. Yamada, J. Vac. Sci. Technol. **A8**, 1470 (1990).

[9] S.Q. Hong, C.M. Comrie, S.W. Russell and J.W. Mayer, J. Appl. Phys. **70** 3655 (1991).

[10] J.M.E. Harper, A. Charai, L. Stolt, F.M. d'Heurle, and P.M. Fryer, Mat. Res. Soc. Symp. Proc. Vol. **187**, 107 (1990).

[11] J.A. Schaefer, Physica **B170**, 45 (1991).

[12] S. Nikzad, S.S. Wong, C.C. Ahn, A.L. Smith, and H.A. Atwater, Appl. Phys. Lett. **63**, 1414 (1993).

[13] J.W. Matthews and A.E. Blakeslee, J. Cryst. Growth. **27**, 118 (1974).

[14] C.J. Tsai, Ph.D. Thesis, California Institute of Technology, 1992.

Chapter 5

Structural, Magnetic and Magnetotransport Properties of Epitaxial $Ni_{80}Fe_{20}$ Films on Cu/Si

5.1 Introduction

Permalloy ($Ni_{80}Fe_{20}$) heterostructures are of great interest for magnetoresistive devices based on anisotropic magnetoresistance (AMR) and recently discovered "giant" magnetoresistance (GMR) in magnetic multilayers[1, 2]. In particular, all investigations to date of magnetic multilayers which exhibit GMR have employed polycrystalline films with atomically rough interfaces where the interface roughness is of the same order as the nonmagnetic spacer layer thickness[2, 3]. Giant magnetoresistance in magnetic multilayers was first observed for Fe/Cr multilayers for Fe layers $\leq$ 100 Å and Cr layers $\leq$ 50 Å[1]. The Fe layers were antiferromagnetically(AF)-coupled with the coupling strength depending sensitively on the Cr interlayer thickness. As a

function of Cr thickness, this AF-coupling exhibited an oscillatory behaviour. The cause of this anomalous coupling and the oscillations is a source of great interest and debate[4]. Furthermore, when the magnetizations of the AF-coupled Fe layers are made parallel by application of an external field, a significant change in the resistance of the multilayer occurs, which is referred to as GMR. Since then, both AF-coupling and GMR have been observed for many magnetic multilayered systems including Co/Cu[5] and $Ni_{80}Fe_{20}$/Cu[2]. The AF-coupling can neither be explained in terms of exchange interactions, as the exchange interaction length (typically a few Å) is much smaller than the interlayer thicknesses, nor in terms of magnetostatic interactions, as the dipolar coupling is much weaker than that observed experimentally. A complete explanation of AF-coupling remains a challenge to theorists. Currently, the two major contenders are (i) Ruderman-Kittel-Kasuya-Yosida (RKKY) coupling aligning the antiparallel magnetic moments via conduction electrons and (ii) quantum-well states near the fermi level, arising from the periodicity of the multilayer[4]. On the other hand, the most common mechanism for explanation of GMR is a spin-dependent interfacial scattering of conduction electrons in the ferromagnetic layers of the multilayer[6, 7]. These theories assume that nonmagnetic metal atoms dissolved in the ferromagnetic layers near the interfaces act as spin-dependent impurity scatterers which are known to contribute to magnetoresistance of bulk ferromagnetic materials[8]. This suggests that the magnetotransport properties of atomically-abrupt epitaxial grain-boundary free films should more clearly elucidate the underlying physics[9]. Furthermore, with atomically-abrupt film interfaces, it would be possible to fabricate thinner nonmagnetic spacer layers without the interface

roughness being the limiting factor[2]. Growth of epitaxial multilayers of NiFe/Cu as well as other heterostructures such as spin-valves for studying GMR was one of the motivations for work described in this chapter.

Furthermore, in the last decade, a great deal of attention has been directed to the study of coherency strain and its effects on the electronic and mechanical properties of strained multilayers, or *superlattices*. However, the growth of epitaxial magnetic films and the effects of coherency strain on magnetic properties, especially anisotropy and magnetic moment, have only recently attracted attention[10]. In particular, magnetic properties of epitaxial Fe and Ni thin films on Cu(001) have been studied recently[11, 12] whereas heteroepitaxy of metal films has been of interest since 1970 when Matthews and Crawford[13] studied strain relaxation in epitaxial Ni(001) films on Cu(001).

In this chapter, we report structural, magnetic and magnetotransport properties of epitaxial $Ni_{80}Fe_{20}$(001) films grown on Cu(001) as well as on nearly lattice-matched $Cu_{35}Ni_{65}$ films, 10-50 nm thick, oriented epitaxially with respect to Si(001). Permalloy ($Ni_{80}Fe_{20}$) has a *fcc* structure with a lattice parameter of 3.549 Å, which has a misfit of -1.85% with that of Cu and -0.2% with $Cu_{35}Ni_{65}$. This is assuming that Cu and Ni form a solid solution (even though Cu and Ni have a miscibility gap at room temperature[14], it is unlikely that elemental segregation takes place, because film growth by sputtering is a process, which occurs far from thermodynamic equilibrium). The $Ni_{80}Fe_{20}$ as well as the $Cu_{35}Ni_{65}$ films had the same crystallographic orientation as the Cu seed layers, as verified by RHEED and x-ray diffraction. The epitaxy of Cu(001) at room temperature on H-terminated Si(001) is dis-

cussed in Chapter 4. Epitaxial NiFe films have been grown in the past as well by researchers on MgO, NaCl and Cu substrates[15, 16, 17]. However, high quality substrates of Cu, MgO and NaCl are not as cheaply available as high quality Si substrates, and also have higher dislocation densities. This suggests that magnetoresistive Permalloy devices can be integrated with other electronic devices grown on Si. The growth of $Ni_{80}Fe_{20}$ and Ni-rich Cu_xNi_{1-x} films directly on H-terminated Si(001) resulted in highly (111)-textured polycrystalline films. This suggests the possibility of controlling crystallographic texture in these multilayers and studying AF-coupling and GMR in multilayers as a function of texture[18, 19].

Surface lattice constant variations of $Ni_{80}Fe_{20}$ as a function of thickness were also studied during its epitaxial growth using RHEED, as explained in Sec.2.4. See the next two sections for comparison of experimental results with the theory of strain relaxation in epitaxial films[13]. X-ray diffraction, atomic force microscopy (AFM) and transmission electron microscopy (TEM) were also utilized for *ex situ* structural characterization of these films. Magnetostriction measurements were performed to estimate the magnetoelastic anisotropy in these films as a consequence of coherency strain. Magnetic properties of these films were measured *in situ* as a function of film thickness and were correlated with coherency strain. Finally, magnetic and magnetoresistive properties of these epitaxial films were compared with those of polycrystalline films deposited on SiO_2/Si.

5.2 Strain Relaxation during Heteroepitaxial Growth of Thin Films

It is well known that for growth of an overlayer B on substrate A and for small misfit f ($\leq 10\%$) between the lattice constants of A and B, the lattice of B may expand or contract to form a coherent interface with that of A. However, formation of such an interface is associated with strain energy in the overlayer B. Using linear elasticity theory, it follows that the energy per unit area u_{coh} due to coherency strain ϵ in a film of thickness h, is[20, 21]:

$$u_{coh} = 2\mu \left(\frac{1+\nu}{1-\nu}\right) h\epsilon^2 \tag{5.1}$$

where μ and ν are the shear modulus and the Poisson's ratio for the overlayer, respectively. For h greater than a critical thickness h_c, it becomes energetically more favorable to relieve this coherency strain energy by generation of misfit dislocations at the interface. As a result, the misfit is shared between elastic strain ϵ, and misfit dislocations with density ρ_{md} and Burger's vector b. If the dislocation makes an angle α with the plane of the interface, then the component which relieves misfit strain is $b_{||} = b\cos\alpha$, so that

$$f = \epsilon + \rho_{md} b\cos\alpha. \tag{5.2}$$

Using Eq. (5.1) and (5.2), u_{coh} can be expressed in terms of ρ_{md} as

$$u_{coh} = 2\mu \left[\frac{1+\nu}{1-\nu}\right] h(f - \rho_{md} b_{||})^2. \tag{5.3}$$

On the other hand, the energy per unit area u_{disl} required to create misfit dislocations of density ρ_{md}, is given by[22]:

$$u_{disl} = \rho_{md} \frac{\mu b^2}{4\pi} \left[\frac{1-\nu\cos^2\beta}{1+\nu}\right] \ln\left(\frac{4h}{b}\right), \tag{5.4}$$

where β is the angle between the Burger's vector and the dislocation line. The equilibrium misfit dislocation density for $h > h_c$ is found by minimizing the total energy $u_{tot} = u_{coh} + u_{disl}$ with respect to ρ_{md} using Eq. (5.3) and (5.4), i.e., by setting

$$\frac{\partial u_{tot}}{\partial \rho_{md}} = 0. \tag{5.5}$$

This condition yields

$$\rho_{md} = \frac{f}{b\cos\alpha} - \frac{1}{8\pi h\cos^2\alpha}\left[\frac{1-\nu\cos^2\beta}{1+\nu}\right]\ln\left(\frac{4h}{b}\right). \tag{5.6}$$

An expression for elastic strain as a function of film thickness can be obtained as well using Eq. (5.2) and (5.6):

$$\epsilon = \begin{cases} f & h < h_c \\ \frac{b}{8\pi h\cos\alpha}\left[\frac{1-\nu\cos^2\beta}{1+\nu}\right]\ln\left(\frac{4h}{b}\right) & h > h_c \end{cases} \tag{5.7}$$

The variation of misfit dislocation density and elastic strain as given by the above equations is plotted in Fig. (5.1) for epitaxial growth of $Ni_{80}Fe_{20}$ on Cu(001). The critical epitaxial thickness h_c can be obtained by setting $\rho_{md} = 0$ in Eq.(5.6), giving:

$$h_c = \frac{b}{8\pi f\cos\alpha}\left[\frac{1-\nu\cos^2\beta}{1+\nu}\right]\ln(\frac{4h_c}{b}) \tag{5.8}$$

which can be solved transcendentally to calculate h_c for a given misfit f. Substituting the lattice constant of $Ni_{80}Fe_{20}$ for b, $\alpha = \beta = 60^o$ which is often the case for *fcc* crystals, ν of 0.31 for Ni (as elastic properties of $Ni_{80}Fe_{20}$ are very similar to those of Ni[23]) and misfit f for $Ni_{80}Fe_{20}$/Cu, h_c was found to be 4.1 nm by solving Eq. (5.8). On the other hand, for $Ni_{80}Fe_{20}$ growth on $Cu_{35}Ni_{65}$ for which the misfit is -0.2%, Eq. (5.8) yielded a critical thickness of 62.8 nm. As mentioned earlier, the accommodation of misfit for epitaxial

growth of Ni on single crystal Cu(001) substrate was investigated in 1970 by Matthews and Crawford[13], and more recently by Inglefield *et al.*[12]. In both studies, the strain relaxation observed experimentally agreed well with that predicted by the above analysis. Strain relaxation measurements for epitaxial growth of $Ni_{80}Fe_{20}$ on Cu/Si(001) is discussed in next section.

The above analysis assumes that there are no thermodynamic barriers to nucleation of misfit dislocations which is a reasonable assumption for metals[13]. However, if the film has not attained thermal equilibrium, residual strain may persist in the film for thicknesses greater than h_c. In the case of $Ni_{80}Fe_{20}$ growth on Cu/Si(001) films, it is likely that threading dislocations, which can give rise to strain-relieving misfit dislocations at the heterointerface by kink formation, are already present in the Cu film due to the mismatch between Cu and Si.

Furthermore, besides misfit dislocations, other mechanisms for strain relief in epitaxial thin films include formation of inclusions[24] or *coherent islanding*[25]. In particular, the latter mechanism has been observed experimentally in case of epitaxial growth of SiGe alloys on Si[26] and InGaAs on GaAs[27]. XTEM and AFM observations by these investigators clearly show a sinusoidal surface profile along with oscillatory strain contrast in both the film and the substrate. This phenomenon is explained well by a stability analysis of stressed solid surfaces[25]. It is shown that small surface undulations in a band of wavelengths $\lambda_c \leq \lambda \leq \lambda_{max}$ will grow exponentially, where λ_c and λ_{max} are the critical and the maximum wavelengths, respectively for coherent islanding to occur. A crude estimate of the critical wavelength can be made by comparing the change in energy ΔE associated with a transition

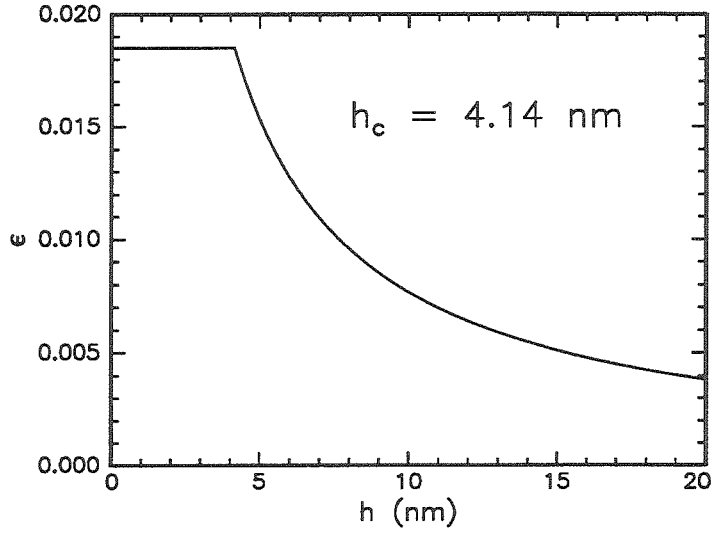

(a)

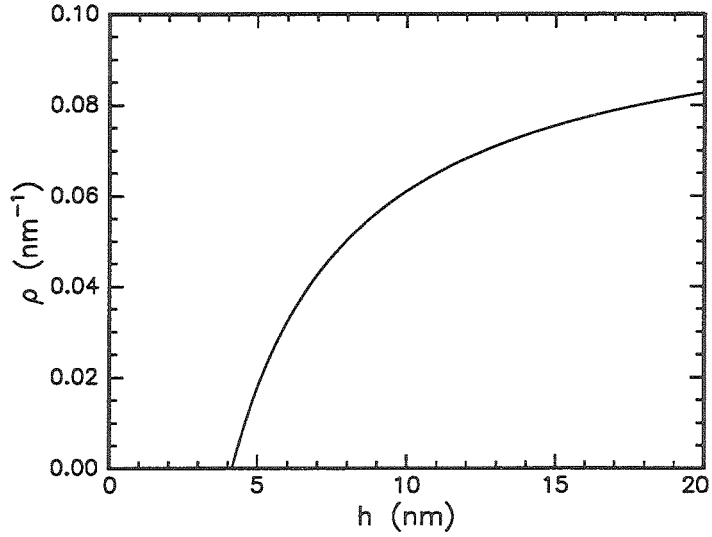

(b)

Figure 5.1: Variation of (a) elastic strain and (b) misfit dislocation density with film thickness as predicted by theory of strain relaxation for $Ni_{80}Fe_{20}$ film growth on Cu(001).

from a flat surface to a rough surface with wavelength λ and amplitude h, as shown in Fig.5.2 assuming that the stress in the interior of the square protrusion is zero[25]. The change in energy would then be the energy associated with the increased surface area minus the strain energy gained i.e.,

$$\Delta E = -\frac{\sigma_{||}^2}{2Y}\frac{h\lambda}{2} + 2\gamma_{surf}c, \tag{5.9}$$

where $\sigma_{||}$ is the elastic stress, γ_{surf} is the surface energy, and Y is the modulus of elasticity. Setting $\Delta E = 0$ in above equation gives an expression for the critical wavelength:

$$\lambda_c = \frac{8\gamma_{surf}Y}{\sigma_{||}^2}. \tag{5.10}$$

Substituting $\gamma_{surf} = 1800$ erg/cm^3 from experimentally reported values[28] and $\sigma_{||}$ corresponding to a fully coherent $Ni_{80}Fe_{20}$ film on Cu, the critical wavelength for this case was estimated to be 93.6 nm. It is plausible that with increasing film thickness, these coherent islands coalesce, giving rise to misfit dislocations at their boundaries, which further relieve coherency strain. This is supported by XTEM analysis of Cu films on Si (see Fig.4.6), which shows periodic strain modulations in the substrate as well as the film.

5.3 Strain Relaxation Measurements using Electron Diffraction

Strain measurements were made using surface lattice constants calculated from electron diffraction patterns as discussed in Sec.2.4. Surface lattice constant measurements using RHEED are shown in Fig. 5.3 for growth of $Ni_{80}Fe_{20}$ films on Cu/Si(001). For these studies, the Cu film was at least

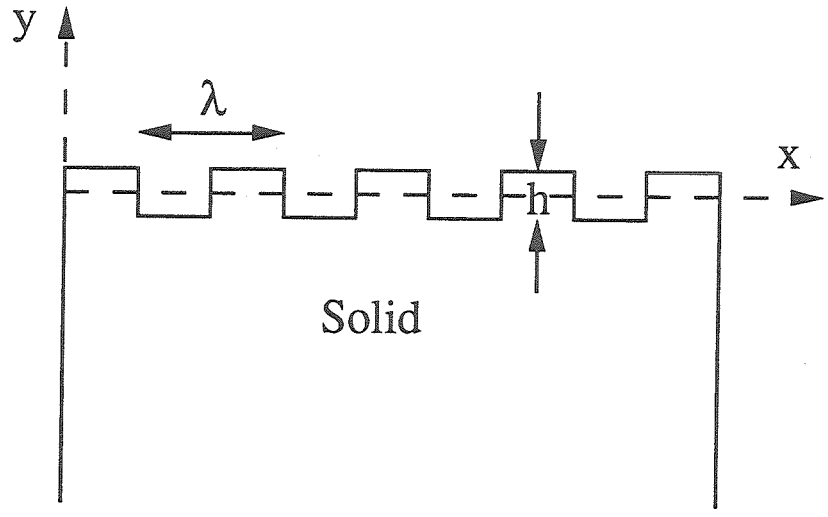

Figure 5.2: A stressed solid with a square wave profile.

50 nm thick to ensure that it had relaxed to its bulk lattice parameter, and did not have any coherency strain present due to its mismatch with Si. The RHEED pattern from the H-terminated Si was used to calibrate the camera length for the RHEED geometry and thus convert the separation between RHEED spots to surface lattice constants for $Ni_{80}Fe_{20}$ and Cu. During the course of film growth, great precautions were taken to ensure that the RHEED beam did not move and thus change the camera constant. The large error bars for these surface lattice constant measurements are mainly due to the limited resolution of the video camera used for recording RHEED patterns. Typically, for an electron energy of 15 keV, the separation between the electron diffraction spots due to an epitaxial Cu(001) film along [100] azimuth was $\cong$ 3 cm. Thus, for $Ni_{80}Fe_{20}$ film growth on Cu which has a mismatch of 1.85%, the change in the spot positions would be 0.05 cm. How-

ever, the resolution of the video camera used for recording RHEED patterns was $\cong$ 10 cm/600 pixels = 0.017 cm/pixel assuming it had 600 pixels over a screen length of 10 cm. As a consequence, it was difficult to accurately calculate the strain in the $Ni_{80}Fe_{20}$ film using this technique. Nevertheless, it can be observed from these studies that the $Ni_{80}Fe_{20}$ is coherent with the Cu film up to 2 nm and the film relaxes to its bulk lattice constant after 4 nm, which is in reasonable agreement with the critical thickness predicted by the strain relaxation theory of Matthews[13] as discussed in the previous section. The resolution of this technique might be improved further by using a higher resolution camera such as a CCD array or a carefully apertured analog photodiode for recording RHEED patterns. The other techniques for measuring the thin film strain are based on wafer curvature and x-ray diffraction. However, it is difficult to implement these techniques for *in situ* measurements. In particular, the latter can be implemented in a practical manner, for *in situ* measurements only if access to synchrotron radiation during thin film growth is possible[29].

5.4 Structural Characterization

The tools employed for structural characterization of these films were *in situ* RHEED and *ex situ* x-ray diffraction and TEM analysis. AFM was also used to study surface roughness of $\leq$ 5 nm epitaxial $Ni_{80}Fe_{20}$ films on Cu/Si. No change in the RHEED intensity profiles was observed during epitaxial growth, suggesting that the $Ni_{80}Fe_{20}$ film had the same crystallographic structure as the Cu film on Si(001). Furthermore, no change in the Bragg rod width

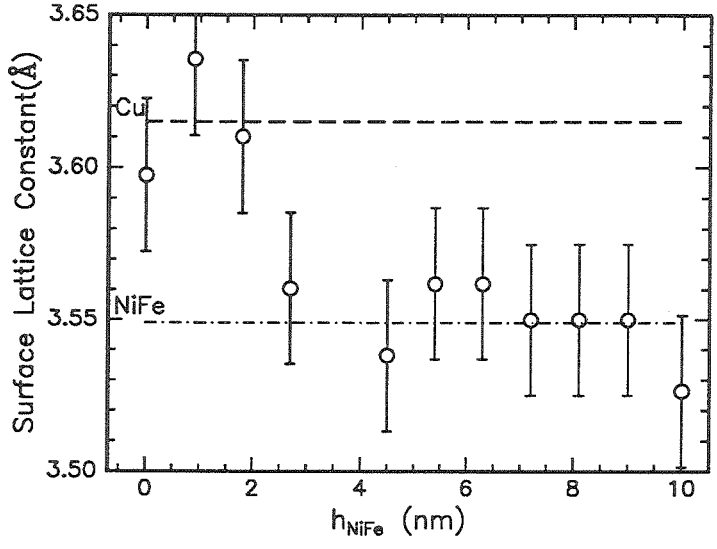

Figure 5.3: Surface lattice constants as calculated from RHEED measurements of (001) $Ni_{80}Fe_{20}$ film grown on Cu/Si(001) as a function of film thickness

was detectable implying that there was not significant roughening during this epitaxial growth. However, for the geometry used, the RHEED beam penetration into the film is about 2.0 nm. Thus, if $Ni_{80}Fe_{20}$ film growth occurs via an islanding mechanism below that thickness, it would not be detectable using the present RHEED configuration.

Large angle x-ray diffraction using the Inel thin film diffractometer described in Sec.2.5.2, was used to confirm the crystallographic orientation of the film just as in the case of Cu films on Si. Figure 5.4 shows a diffraction spectrum for an x-ray beam incidence angle of 30° for a 30 nm thick $Ni_{80}Fe_{20}$ film deposited on Cu(30 nm)/Si(001) which indicates that the (100) texture in the films is 2-3 orders of magnitude more pronounced than other *fcc* textures, notably (111). Furthermore, the lattice constants calculated from the diffraction spectrum confirm that the Cu and $Ni_{80}Fe_{20}$ films are strain-relieved; i.e., have the bulk lattice constants.

TEM studies were employed to obtain further information about the nature of epitaxy and the sharpness of Cu/NiFe interface. Figure 5.5 shows a high resolution XTEM image of a 50 nm thick epitaxial $Ni_{80}Fe_{20}$ film on Cu(50nm)/Si(001), along the [110] Si zone axis. In this image, lattice fringes extending from the Cu/Si interface to the $Ni_{80}Fe_{20}$ film surface can be seen. The inset shows the selected area diffraction pattern due to (001) $Ni_{80}Fe_{20}$/Cu films and the Si substrate. Furthermore, a mosiac spread of up to $\pm$ 6° in the (001) texture can be observed in the lattice fringes as well as the diffraction pattern due to the film just as in the case of epitaxial Cu films on Si, discussed in Chapter 4. The $Ni_{80}Fe_{20}$/Cu interface cannot be clearly seen in Fig. 5.5 due to lack of Z-contrast between $Ni_{80}Fe_{20}$ and Cu. However, it is discernible

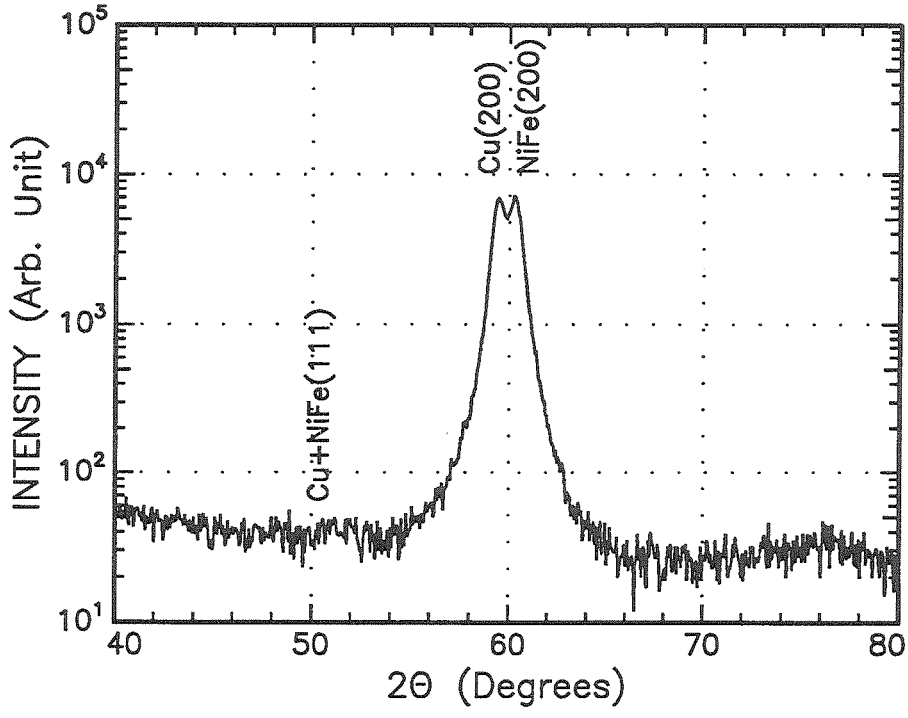

Figure 5.4: CoK_α x-ray diffraction spectrum of 30 nm $Ni_{80}Fe_{20}$ epitaxial film on Cu(30nm)/Si(001).

by the presence of Moiré fringes and misfit dislocations, which indicate a semicoherent interface between Cu and $Ni_{80}Fe_{20}$. From the atomic sharpness of Cu/Si interfaces shown in XTEM pictures in the previous chapter, it might be expected that the NiFe/Cu interface is sharp as well. Furthermore, from XTEM analysis, the surface roughness of the $Ni_{80}Fe_{20}$ films deposited on thin Cu seed layers (10-50 nm) was found to be $\leq$ 1.0 nm whereas for much thicker Cu seed layers (320 nm) the rms roughness was 9.3 nm, with a wavelength of about 200 nm. It is possible that this increased roughness for thicker Cu seed layers is due to the mosiac spread in the epitaxy and the columnar structure of the Cu film, which can give to a microstructure as illustrated in Fig.5.7.

Plan view dark field TEM of the NiFe/Cu film is shown in Fig. 5.6 for which $\vec{g}$ and the zone axis were along $[\bar{1}11]$ and [211], respectively. The diffraction pattern is shown in the inset. The micrograph suggests that the film is polycrystalline; however, slight tilting of the goniometer reveals rectangular domain-like structures which change from strongly diffracting to weakly diffracting and vice versa. This suggests that not all the regions of the film diffract strongly for the same orientation because of the mosiac spread in the (001) epitaxy.

AFM measurements were made of $\leq$ 5.0 nm thick polycrystalline $Ni_{80}Fe_{20}$ films grown on SiO_2/Si and epitaxial films grown on 10-50 nm thick Cu seed layers on Si. A H-terminated Si(001) sample was used to calibrate the instrumental resolution of the AFM and was found to have a rms roughness of less than 0.2 nm. For surface roughness measurements, the scan size was typically 300 nm $\times$ 300 nm and scans were made of many different areas of the

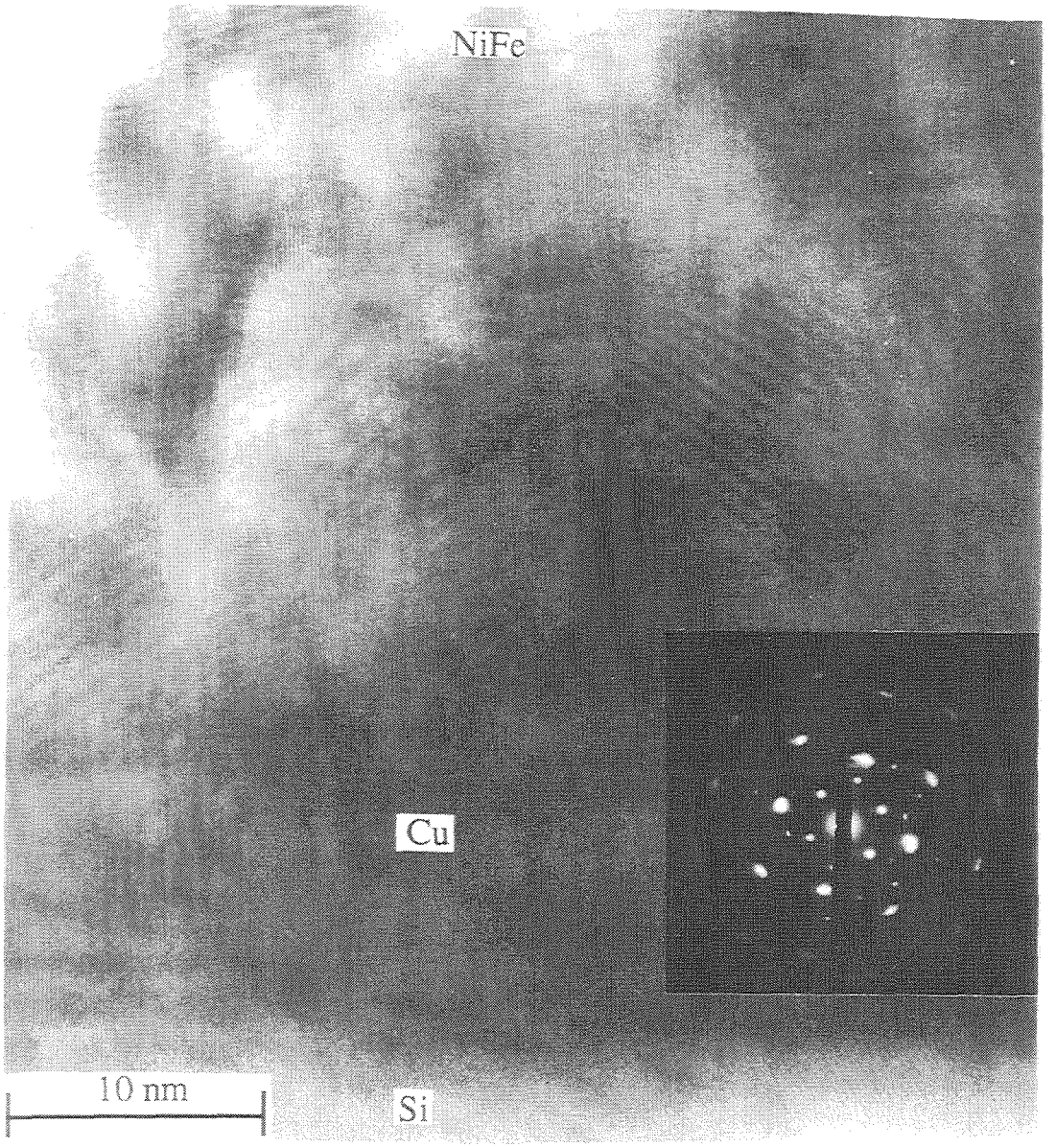

Figure 5.5: High resolution cross-sectional transmission electron micrographs of epitaxial (001) $Ni_{80}Fe_{20}$ film on Cu/Si(001). The inset shows the diffraction pattern of Si substrate and $Ni_{80}Fe_{20}$/Cu films along [110] and [100] zone axes, respectively.

Figure 5.6: Plan view dark field transmission electron micrographs of epitaxial $Ni_{80}Fe_{20}$ film on Cu/Si(001), viewed along [211] zone axis with $\vec{g}$ =[$\bar{1}$11].

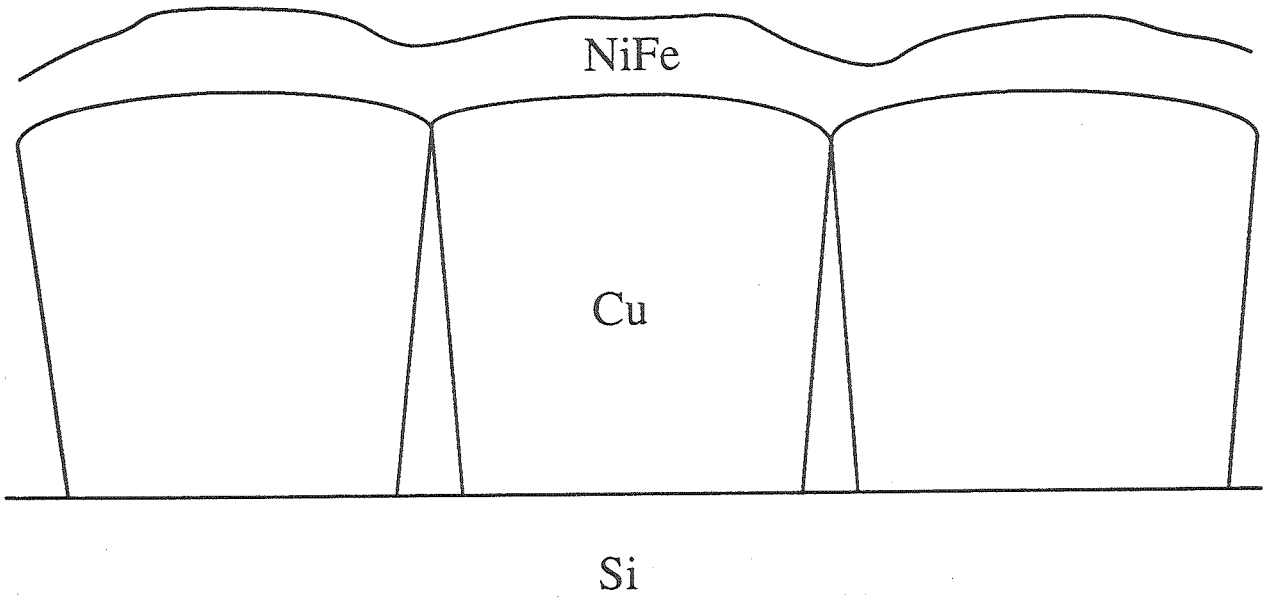

Figure 5.7: Schematic of the microstructure of the Cu film which can cause increasing roughness with increasing thickness.

sample. The rms roughness for the epitaxial films was 0.215 nm and 0.568 nm for Cu underlayers 10 nm and 50 thick. On the other hand, the polycrystalline films of the same thickness had a rms roughness of 0.118 nm (see Fig.5.8). Furthermore, the wavelength of the roughness for the epitaxial films was much larger than that for the polycrystalline films, as can be observed from Fig.5.8. The larger roughness of the epitaxial films may be due to kinetic roughening, which is a consequence of film growth by an island mechanism for Cu on Si and $Ni_{80}Fe_{20}$ on Cu, as discussed in Sec.5.2. This kinetic roughening has been observed for systems with comparable misfit, e.g., growth of SiGe alloys on Si[26]. In particular, the larger surface roughness for thicker Cu underlayers might be a consequence of the columnar structure of the Cu film as discussed earlier and illustrated in Fig.5.7.

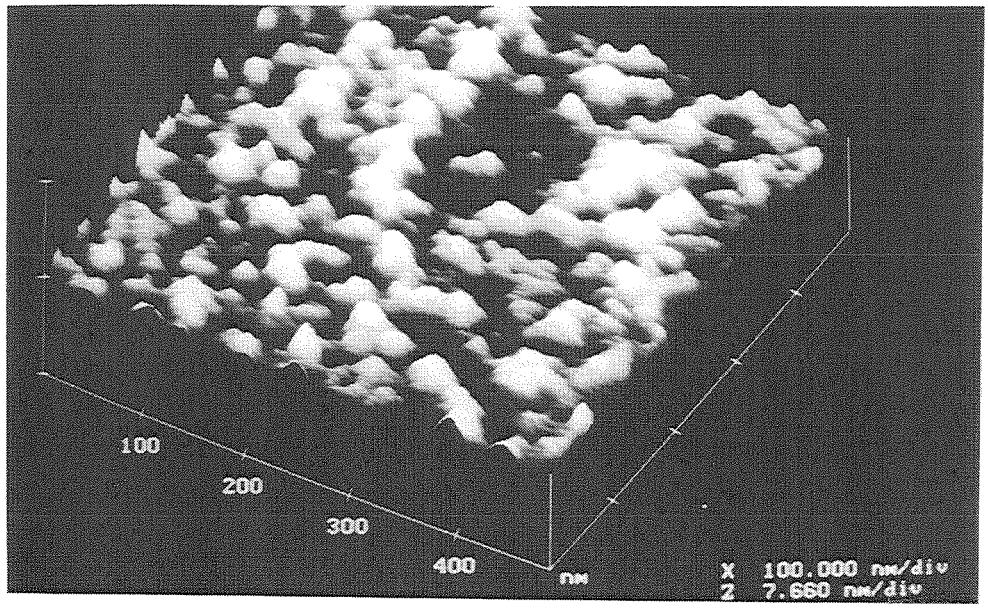

(a)

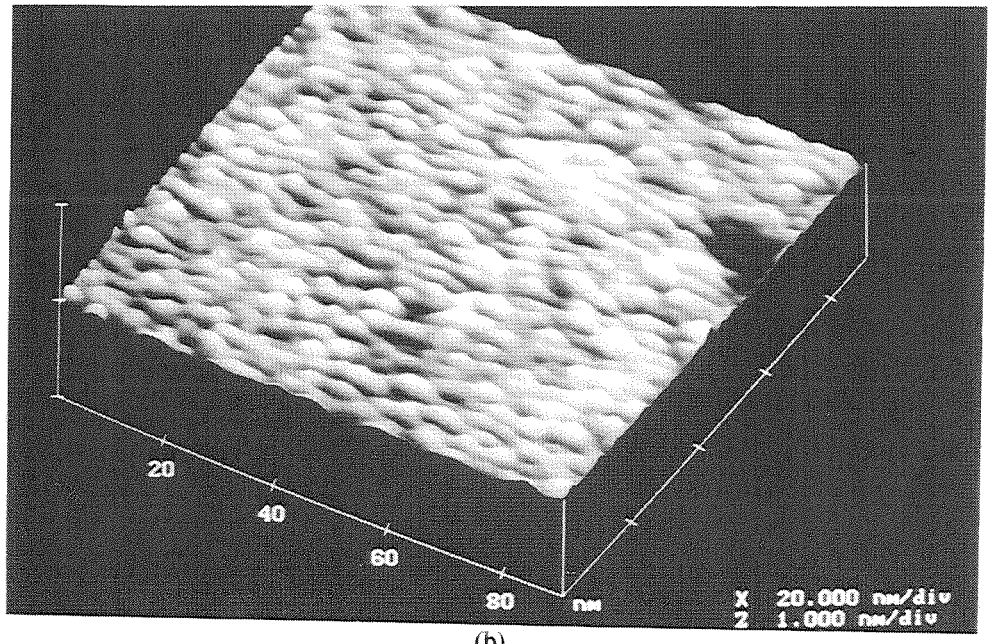

(b)

Figure 5.8: Atomic force microscope images of (a) epitaxial $Ni_{80}Fe_{80}$ film deposited on Cu(50 nm)/Si(001) and (b) polycrystalline $Ni_{80}Fe_{20}$ film deposited on SiO_2/Si.

5.5 Magnetoelastic Energy and Magnetostriction

5.5.1 Theory

Magnetoelastic energy arises from the interaction between the magnetization and the mechanical strain of the lattice. In particular, it is a consequence of magnetocrystalline anisotropy of ferromagnetic materials. When magnetized along a certain crystallographic direction, the crystal lattice will spontaneously deform to lower the magnetic anisotropy energy. The elastic energy associated with this lattice deformation is referred to as magnetoelastic energy. Mathematically, the dependence of the magnetic anisotropy energy K on strain components e_{ij} is expressed in terms of a Taylor expansion[30]:

$$K_{me} = K^{\circ} + \sum_{i \geq j} \frac{\partial K}{\partial e_{ij}} e_{ij} + ... \tag{5.11}$$

where $\frac{\partial K}{\partial e_{ij}}$ are related to magnetoelastic coupling coefficients, denoted by B_{ij}, and the direction cosines α_i of the magnetization vector $\vec{M}$. For cubic lattices, there are only two magnetoelastic constants, B_1 and B_2, such that the above equation becomes:

$$K_{me} = K^{\circ} + B_1 \sum_{i=1}^{3} e_{ii}\alpha_i^2 + \frac{1}{2} B_2 \sum_{i=1}^{3} \sum_{j=1, j \neq i}^{3} e_{ij}\alpha_i\alpha_j + ... \tag{5.12}$$

The magnetoelastic coefficients are often defined in terms of experimentally more accessible saturation *magnetostriction* coefficients, λ_{111} and λ_{100}[30]. While the magnetoelastic coefficients have the dimensions of stress, the magnetostriction coefficients have the dimensions of strain and are related to B_1 and B_2 via the elastic moduli c_{ij}[30]. For single crystal Ni, $\lambda_{111} = -24 \times 10^{-6}$

and $\lambda_{100} = -46 \times 10^{-6}$ whereas for Fe, they are $+21 \times 10^{-6}$ and -21×10^{-6}, respectively. In the case of random polycrystalline samples, the magnetostriction is well represented by a single coefficient λ_s[31]:

$$\lambda_s = \frac{2}{5}\lambda_{100} + \frac{3}{5}\lambda_{111}. \tag{5.13}$$

For $Ni_{80}Fe_{20}$, the magnetostriction is an order of magnitude smaller than that for either Ni or Fe ($\lambda_s \cong 0$ near the composition $Ni_{81}Fe_{19}$), and furthermore, it is isotropic, i.e., $\lambda_{100} \cong \lambda_{111}$. Nevertheless, its exact value is rather sensitive to film composition, crystallographic texture, and method of film preparation[32].

5.5.2 Magnetostriction Measurements

The common techniques employed for measurement of magnetostriction can be divided into two categories, the direct and the indirect methods. The latter involves application of a known stress and measuring the resulting change in the anisotropy field H_k. This change in H_k is related to the change in the applied tensile stress ΔS, by[33]:

$$\Delta H_k = 3\frac{\lambda_s}{M_s}\Delta S. \tag{5.14}$$

The direct method measures the small bending of the thin film upon application of a magnetic field. Assuming that the magnetic film is thin compared to the substrate, the deflection d and the local slope ϕ at the measurement point at a distance l from the origin O (see Fig. 5.9) are given by[33]:

$$\begin{aligned} d &= \frac{3t_f l^2 \xi}{t_s^2}\lambda_s \\ \phi &= \frac{2d}{l} = \frac{6t_f l \xi}{t_s^2} \end{aligned} \tag{5.15}$$

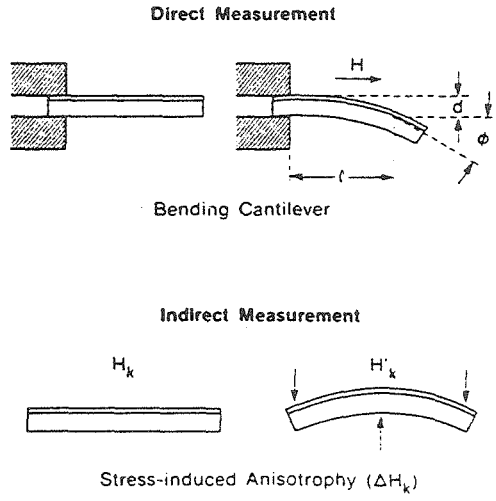

Figure 5.9: Schematic of methods to measure the magnetostriction of a thin film deposited on a nonmagnetic substrate.

Here t_f, t_s are the thicknesses of the film and the substrates, respectively and ξ is defined as:

$$\xi = \frac{Y_f(1-\nu_s)}{Y_s(1+\nu_f)}, \tag{5.16}$$

where Y_f, Y_s, and ν_f, ν_s are Young's modulus and Poisson's ratio of the film and the substrate, respectively.

A magnetostriction measurement tool at IBM Almaden Research Center based on the direct method described above was used to measure λ_s for epitaxial $Ni_{80}Fe_{20}$ films of various thicknesses on Cu/Si. The sample dimensions were 35 x 10 cm and a relatively thin Si wafer of thickness $300 \pm 25\mu$m was used as the substrate. The following elastic constants for Si and $Ni_{80}Fe_{20}$ were substituted in Eq.(5.15) to obtain λ_s:

$$Y_f = 2.14 \times 10^{12} \text{dynes/cm}^2, \quad \nu_f = 0.31,$$

Thin Film Structure	λ_s
NiFe(7.5 nm)/Cu(50nm)/Si(001)	$1.32 \times 10^{-6} \pm 10\%$
NiFe(15 nm)/Cu(50nm)/Si(001)	$0.62 \times 10^{-6} \pm 7\%$
NiFe(20 nm)/Cu(50nm)/Si(001)	$0.72 \times 10^{-6} \pm 7\%$

Table 5.1: Magnetostriction values of epitaxial $Ni_{80}Fe_{20}$ thin films on Cu/Si(001).

$$Y_s = 1.67 \times 10^{12} \text{dynes/cm}^2, \quad \nu_s = 0.25.$$

The values of λ_s thus obtained for NiFe film thicknesses of 7.5, 15.0, and 20.0 nm are listed in Table 5.1. The uncertainty of 1.5×10^{-7} in the measurements results from noise and the ultimate resolution of the tool. These values of λ_s agree well with those reported by Klokholm and Aboaf[32] for NiFe thin films as a function of composition. As mentioned earlier, $\lambda_s = 0$ for composition 81-19 whereas for increasing (decreasing) Fe content, λ_s increases above (decreases below) zero. An increase in λ_s for film thicknesses less than 10.0 nm has been observed by other investigators as well, including O. Song *et al.*[23] and is attributed to an enhanced effect of the interfaces for ultrathin films.

5.6 Magnetic Anisotropy and Strain in Thin Films

Using the definition of magnetostriction introduced in the last section, we evaluate below the effect of strains on magnetic properties, especially magnetic anisotropy of thin films for two important cases: (i) uniaxial strain due

to an applied uniaxial stress, and (ii) biaxial strain in coherent epitaxial thin films. In both cases, we assume that the magnetostriction is isotropic. If an applied uniaxial in-plane stress σ makes an angle θ with the magnetization $\vec{M}$ (also in-plane) then the magnetoelastic contribution follows from Eq. (5.12):

$$K_{me} = Be\cos^2\theta + \text{const} = -\frac{3}{2}\lambda_s\sigma\cos^2\theta + \text{const} \tag{5.17}$$

where the definition $B = -\frac{3}{2}\lambda_s Y$ has been used, with Y and e being the modulus of elasticity and the strain induced due to the applied stress, respectively. From Eq. (5.17), it follows that an applied uniaxial stress can lead to a uniaxial anisotropy similar to the induced uniaxial anisotropy in NiFe alloys.

For biaxial coherency strain $e_{xx} = e_{yy} \equiv e_{||}$, there will be an out-of-plane Poisson's strain due to the distortion of the lattice[21], given by

$$e_{\perp} \equiv e_{zz} = \frac{1+\nu}{1-\nu}e_{||}. \tag{5.18}$$

If $\vec{M}$ makes an angle ϕ with the normal to the film plane, and using the above strain components, Eq. (5.12) becomes

$$K_{me} = Be_{xx}\left[\sin^2\phi - \frac{2\nu}{1-\nu}\cos^2\phi\right]. \tag{5.19}$$

For $Ni_{80}Fe_{20}$ as well as Ni, $\nu = 0.31$, so that $\frac{2\nu}{1-\nu} \cong 1$. Using this approximation, Eq. (5.19) reduces to

$$K_{me} = 2Be_{||}\sin^2\phi \tag{5.20}$$

or in terms of magnetostriction,

$$K_{me} = -3\lambda_s Y e_{||}\sin^2\phi. \tag{5.21}$$

The above equation implies a coherency strain-induced uniaxial anisotropy out of the film plane whereas for in-plane magnetization, there is an isotropic contribution given by $-3\lambda_s Y e_{||}$. Substituting $e_{||} = f$, the misfit for $Ni_{80}Fe_{20}$ between Cu, the elastic modulus of Ni for that of $Ni_{80}Fe_{20}$, and the measured value of λ_s for $Ni_{80}Fe_{20}$, the magnetoelastic energy E_{me} contribution due to coherency strain was estimated to be 5.2×10^4 ergs/cm^3. On the other hand, the magnetoelastic contribution due to coherency strain is reduced to 8.0×10^3 ergs/cm^3 in the case of $Ni_{80}Fe_{20}$ growth on $Cu_{35}Ni_{65}$. This can be compared with other sources of magnetic anisotropy in $Ni_{80}Fe_{20}$, i.e., the induced uniaxial anisotropy energy which for $Ni_{80}Fe_{20}$ is typically 1×10^4 ergs/cm^3 and magnetocrystalline anisotropy which is 2.7×10^3 ergs/cm^3. The fact that the magnetoelastic energy associated with coherency strain is significantly higher than other sources of magnetic anisotropy for coherent films of $Ni_{80}Fe_{20}$, suggests that it would be an important factor in governing magnetic anisotropy. Indeed, it is well known that a perpendicular anisotropy can be induced in ultrathin films due to interaction with strain[34], and this is utilized in magneto-optic media of the future employing Pt/Co multilayers[35].

Besides the magnetoelastic contribution to the perpendicular anisotropy in thin films as discussed above, another contribution comes from the reduced symmetry at the interfaces of a thin film and is known as the surface anisotropy term[34, 36]. This term has the dimensions of energy per unit area, and when multiplied by the film thickness has the same dimensions as the other anisotropy energies. In the following discussion, we will assume that the film is cubic $< 100 >$ so that there is no magnetocrystalline contribution to the perpendicular anisotropy. For magnetization $\vec{M}$ of a thin film

normal to its plane, there is an associated demagnetization energy given by $2\pi M_s^2$, as the magnetostatic energy is much lower if $\vec{M}$ lies in the plane of the film. Based on the above discussion, we can define an effective anisotropy energy E_{eff}:

$$E_{eff} = E_{me} + \frac{2E_{surf}}{t} + E_{demag}, \tag{5.22}$$

or employing Eq.(5.21):

$$E_{eff} = -3\lambda_{ij} e_{||} Y + \frac{2E_{surf}}{t} - 2\pi M_s^2. \tag{5.23}$$

The above equation has been found to be in close agreement with experiments for epitaxially grown ultrathin films of *fcc* Fe[11] and Ni films on Cu(001)[12]. In the case of *fcc* Fe which has a misfit of 0.9% with Cu, the effective anisotropy switched from out-of-plane to in-plane at a thickness of 1.2 nm[11] whereas in the case of Ni growth on Cu which has a misfit of 2.6%, this transition occurred at a thickness of 6.0 nm[12]. The higher transition thickness for Ni is probably due to the combination of demagnetization energy for Ni, being 10 times smaller than that for Fe, and the magnetoelastic contribution for Ni being positive (because of λ_{100} being negative), thus favoring out-of-plane magnetization. Using Eq. (5.23), the thickness below which the magnetization would be out-of-plane for $Ni_{80}Fe_{20}$ was estimated to be 1.0 nm. As this thickness was beyond the resolution of 2.0 nm for our Kerr system, this could not be verified. However, a polar Kerr loop in which the sample is magnetized normal to its plane, for 5.0 nm thickness, is shown in Fig. 5.10. The linear shape of the loop suggests that the magnetization $\vec{M}$ for the 5.0 nm film was in-plane and rotated to out-of-plane upon application of a large magnetic field. On the other hand, the longitudinal Kerr loops

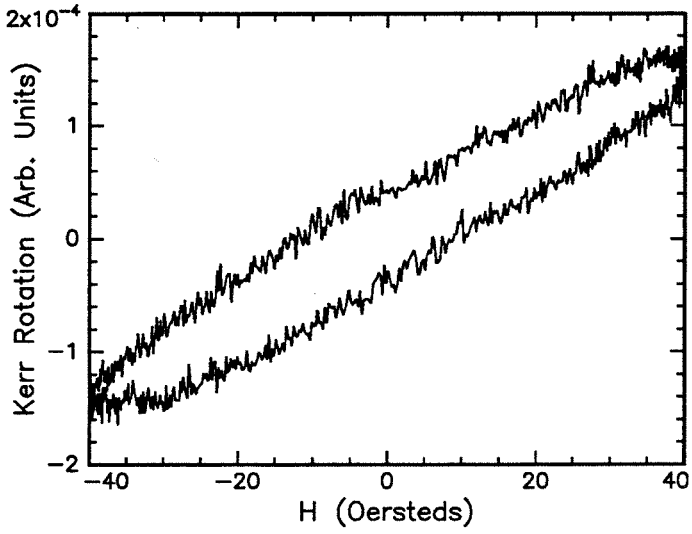

Figure 5.10: Polar Kerr loop for an epitaxial $Ni_{80}Fe_{20}$ film 5.0 nm thick grown on Cu/Si(001).

for in-plane application of a magnetic field were square along the easy axes for all thicknesses greater than 2.0 nm. This suggests that if perpendicular magnetization for thin $Ni_{80}Fe_{20}$ films on Cu does occur, it must for less than 2.0 nm. The magnetic properties reported in the following section are those observed using the longitudinal Kerr effect for in-plane magnetization.

5.7 Variation of Magnetic Properties with Coherency Strain

5.7.1 Experiment

In this section, we report magnetic properties of 2.0-20 nm thick epitaxial and polycrystalline $Ni_{80}Fe_{20}$ films, measured using *in situ* MOKE magne-

tometry. Most of these films were deposited in the presence of an external magnetic field, and thus had a uniaxial anisotropy as a consequence. The magnetic properties measured were the coercivity along easy and hard axes H_{ce} and H_{ch}, respectively, and the uniaxial anisotropy field H_k. In particular, the variation of H_{ce} with epitaxial film thickness was studied. Magnetization along this axis takes place by domain wall motion and hence, is sensitive to defects in the film which can act as pinning sites for domain walls. The coercivity for films $\leq$ 10 nm was found to be as high as 15 Oersteds whereas for greater thicknesess, it decreased to less than 2 Oersteds (see Fig. 5.11). This coercivity is unusually high for $Ni_{80}Fe_{20}$, since for random polycrystalline films deposited under the same conditions on SiO_2/Si, H_{ce} was between 1-2 Oersteds. However, the thicker epitaxial films on Cu/Si, had relatively soft magnetic properties (H_{ce}=2.04 Oe, H_{ch}=0.22 Oe, and H_k=12.3 Oe for 20 nm thick film), which were comparable to those of random polycrystalline $Ni_{80}Fe_{20}$ films of the same thickness. The higher H_c for the thinner films suggests the domain wall motion is impeded, possibly due to coherency strain-related defects in the film. Theoretical models for interaction of domain wall motion with defects in the film are discussed in the next section.

To further investigate the dependence of magnetic properties on coherency strain, $Ni_{80}Fe_{20}$ was grown on nearly lattice matched alloys of Cu_xNi_{1-x}. For the composition 35% Cu (65% Ni), CuNi is nonmagnetic and has a lattice mismatch of only 0.2% with $Ni_{80}Fe_{20}$. The coercivity for these $Ni_{80}Fe_{20}$ films was much smaller than the ones grown directly on Cu, as shown in Fig. 5.11. This further suggests that coherency strain-related defects may be responsible for the higher coercivity in epitaxial films deposited on Cu/Si.

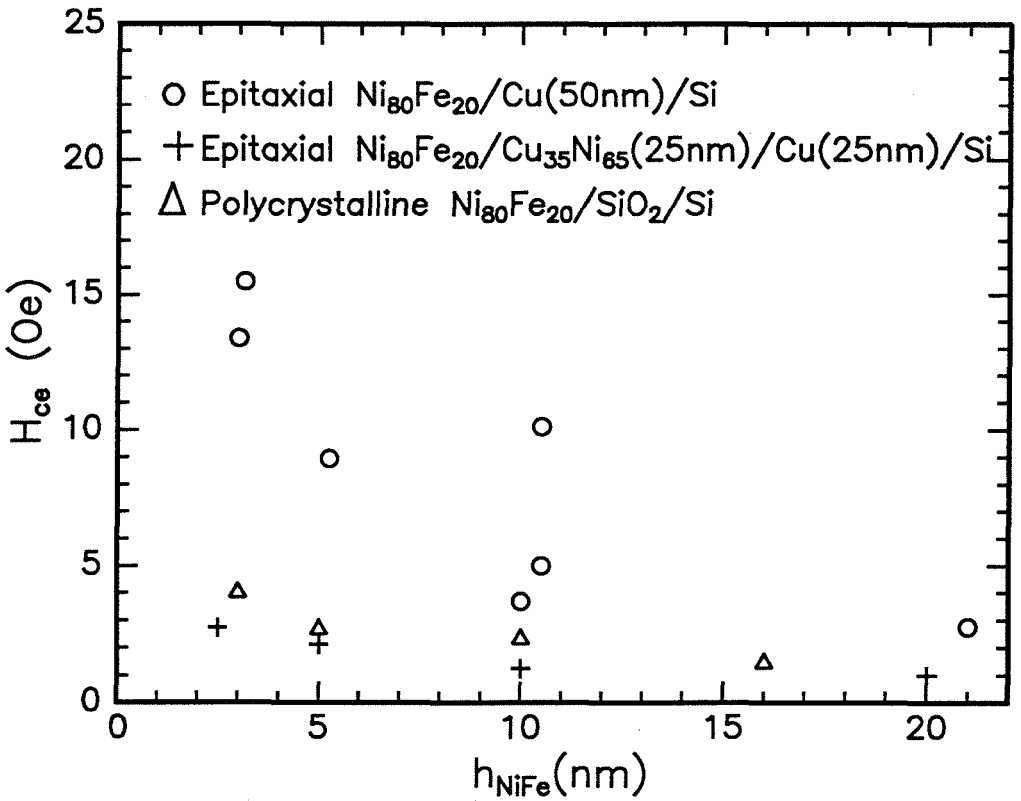

Figure 5.11: Variation of H_{ce} with film thickness for $Ni_{80}Fe_{20}$ deposited on epitaxial Cu and Cu_xNi_{1-x} seed layers, and SiO_2/Si.

Furthermore, H_{ce} was also found to be correlated with the thickness of the Cu seed layer. Figure 5.12 shows H_{ce} for various Cu seed layer thicknesses. As can be seen from this figure, H_{ce} was higher for 50 and 310 nm thick Cu underlayers whereas it was lower for 10 nm thick underlayer. This is consistent with an increasing surface roughness of Cu film with thickness as suggested by by AFM and XTEM analysis discussed in Sec. 5.4. The cause of this increasing surface roughness is probably due to the mosaic spread in the Cu grains and the subsequent columnar structure of these grains as illustrated by the schematic shown in Fig. 5.7 . This suggests that surface roughness can also impede domain wall motion and hence increase H_{ce}.

For some thinner films for which no external magnetic field was used during deposition, a biaxial anisotropy of $\cong$ 7 Oe was observed, and confirmed by vibrating sample magnetometer measurements. For the biaxial anisotropy, the easy axis was along the [110] crystallographic direction of $Ni_{80}Fe_{20}$ whereas the hard axis was parallel to the [100] direction. At first, it might seem plausible that this biaxial anisotropy is due to crystalline anisotropy of $Ni_{80}Fe_{20}$, as K_1 is zero only for the composition 73-27[31]. Dispersion in induced uniaxial anisotropy of epitaxial NiFe films due to its crystallographic orientation with NaCl substrates was observed by investigators at Caltech as early as 1967[37]. Furthermore, K_1 has a negative value for greater Fe contents which would lead to magnetically hard behaviour along [100] crystallographic directions. However, for 80-20 composition, $K_1 = 2.7 \times 10^3$, implying an anisotropy field of 1.65 Oe which is four times smaller than that experimentally observed. This biaxial anisotropy was not observed when an external field was used during deposition and was

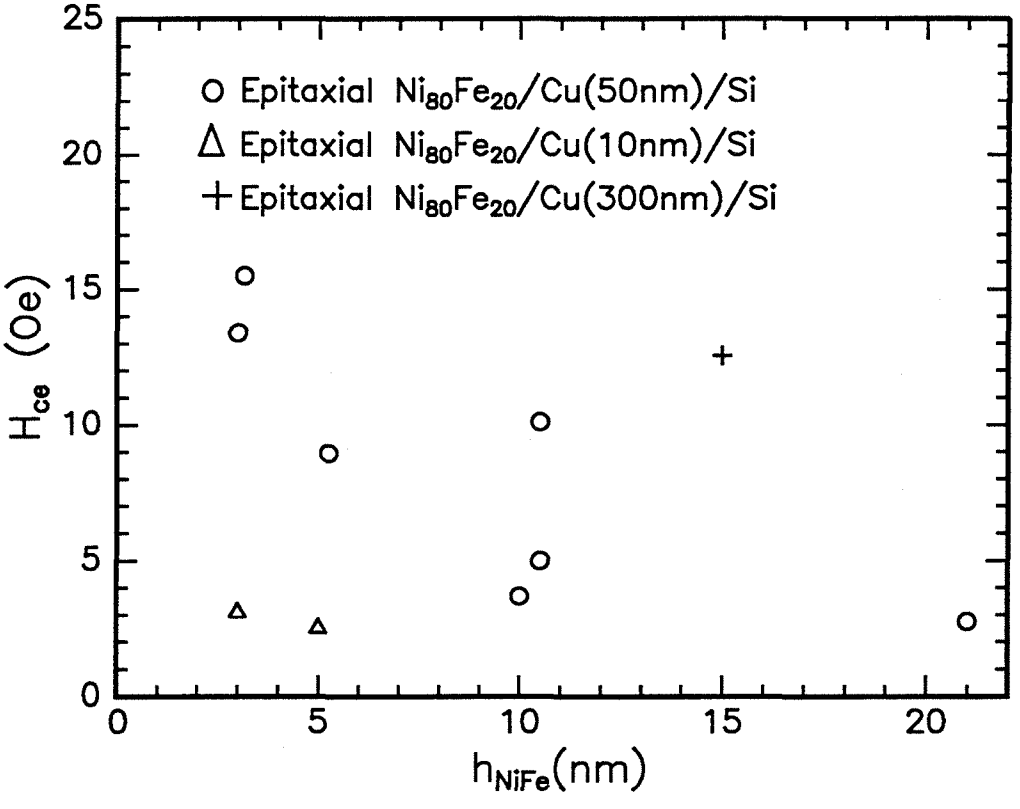

Figure 5.12: Variation of H_{ce} with thickness for $Ni_{80}Fe_{20}$ films deposited on epitaxial Cu seed layers of different thicknesses.

replaced by a uniaxial anisotropy. It is possible that an anisotropic growth morphology during the early stages of epitaxial film growth led to an enhancement of the magnetocrystalline anisotropy as also observed by some other investigators[38].

5.7.2 Theory

Coercivity in magnetic films results from the interaction of domain walls with defects and variations in anisotropy and exchange constants in a soft magnetic thin film. Vast quantities of experimental data for variation of H_c for NiFe films with thickness and deposition parameters exist[38]. Some of the earlier theoretical models to explain the experimentally observed behaviour were made by Néel[39] and Middelhoek[40]. In this section, we extend these models to explain effects of coherency strain on H_c. We start with a domain wall of length l separating two domains in a film of thickness h, as shown in Fig.5.13. If under the action of an applied field H, the domain wall moves by distance dx, then the work done by the field is $2HM_slhdx$. If γ is the domain wall surface energy, the change in energy due to inhomogeneities in the film would be $d(\gamma hl)$. Now, wall motion occurs when the applied field equals H_c, in accordance with definition of coercivity. Energy balance then implies that

$$2H_cM_slhdx = d(\gamma hl) \tag{5.24}$$

or

$$H_c = \frac{1}{2M_slh}\frac{d(\gamma hl)}{dx}$$

$$= \frac{1}{2M_s}\left[\frac{d\gamma}{dx} + \frac{\gamma}{h}\frac{dh}{dx} + \frac{\gamma}{l}\frac{dl}{dx}\right]. \tag{5.25}$$

The three terms on the right-hand side of the above equation correspond to variation of coercivity due to changes in wall energy possibly caused by anisotropy energy variations, film thickness variations possibly due to surface roughness, and domain wall length variations, e.g., due to pinholes in the film, respectively. The spatial derivative of the wall energy can be expressed in terms of spatial variations of anisotropy K as follows:

$$\frac{d\gamma}{dx} = \frac{d\gamma}{dK}\frac{dK}{dx}. \tag{5.26}$$

The dependence of domain wall energy γ as well as of domain wall thickness δ on anisotropy K is discussed in Appendix B. Using Eq.(B.6), it can be shown that

$$\frac{d\gamma}{dK} = \frac{1}{2}\delta. \tag{5.27}$$

Now, as discussed in Sec.5.5, the magnetoelastic anisotropy contribution for epitaxial $Ni_{80}Fe_{20}$ films is much higher than other anisotropy contributions. Hence, we can assume that the anisotropy variations are due to the strain fluctuations in an epitaxial film caused by coherent islanding and/or misfit dislocation arrays as discussed in Sec.5.2. As these fluctuations are periodic, we can write:

$$K_{me} = K^{\circ}_{me}(1 + \epsilon_i \sin\frac{2\pi x}{\lambda_i} + ...) \tag{5.28}$$

where $\epsilon_i (\ll 1)$ and λ_i are the amplitudes and wavelengths of the various perturbations in anisotropy, respectively. Considering only the first harmonic

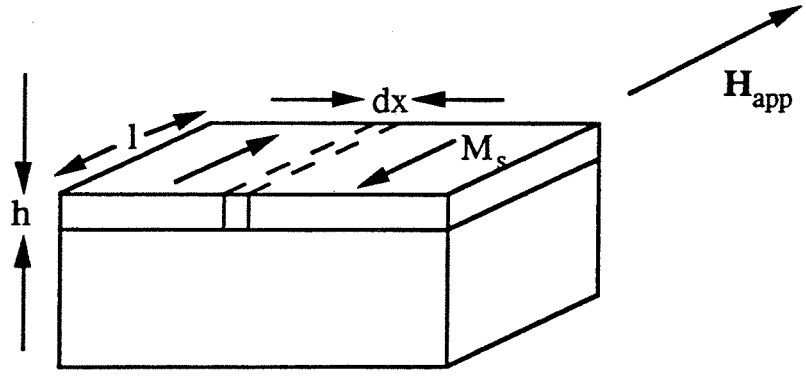

Figure 5.13: Schematic of domain wall separating two domains in a magnetic thin film.

at this point, Eq.(5.26) can be written as:

$$\frac{d\gamma}{dx} = \frac{1}{2}\epsilon_1 \delta K^{\circ}_{me} \frac{2\pi}{\lambda_1} \cos\left(\frac{2\pi x}{\lambda_1}\right). \tag{5.29}$$

Thus, the barrier due to strain fluctuations which the applied field will have to overcome, can be written as:

$$H_c^{strain} = \frac{3}{2}\epsilon_1 \frac{\delta}{M_s} \lambda_s Y e_{\|} \left(\frac{2\pi}{\lambda_1}\right) \tag{5.30}$$

where Eq.(5.21) has been utilized to express K°_{me} in terms of λ_s, Y and $e_{\|}$. If these strain fluctuations are caused by the presence of misfit dislocations to relieve misfit strain, then we can substitute $\lambda_1 = 1/\rho_{md}$ where ρ_{md} is the misfit dislocation density calculated and plotted in Fig.5.1 for epitaxial growth of $Ni_{80}Fe_{20}$ on Cu. Assuming that the strain fluctuations are due to the strain fields of the misfit dislocations and are small except near the core

of the dislocations, we choose $\epsilon_1 = 0.1\%$ somewhat arbitrarily. Substituting the values of λ_s, Y and M_s for $Ni_{80}Fe_{20}$, $e_{||}$ and ρ_{md} as predicted by theory of strain relaxation, and the variation of wall thickness δ as calculated in Appendix B, we obtain the dependence of H_c on film thickness as plotted in Fig.5.14(a). The coercivity in that plot initially increases to a maximum with the nucleation of misfit dislocations after the critical thickness is exceeded to a maximum value of 16 Oersteds. However, even though the misfit dislocation density keeps increasing with thickness, the coercivity decreases after reaching the maximum because of its dependence on the elastic strain and the domain wall thickness, both of which decrease with increasing film thickness. No such increase in coercivity for $Ni_{80}Fe_{20}$ for growth on Cu/Si, due to nucleation of misfit dislocations was observed. One possible reason may be that the domain wall thickness is much greater than misfit dislocation period in the film thickness range 1-20 nm. As shown in Appendix B, the domain wall thickness varies from 1.4 μm to 0.6 μm whereas misfit dislocation density ρ_{md} as calculated in Fig.5.1 implies a misfit dislocation period of $\sim$ 5 nm after the initial stages of strain relaxation. This suggests that the domain wall motion may not be sensitive to the strain fluctuations due to misfit dislocations.

Next, we evaluate the effect of surface roughness on coercivity. There are many factors which can lead to surface roughness in thin films. Here we examine effects of surface roughness caused by coherent island formation to relieve the misfit strain in thin epitaxial films. Even though we have not directly observed the presence of coherent islands using RHEED for epitaxial growth of $Ni_{80}Fe_{20}$ on Cu, AFM measurements -indicating greater surface

roughness of thinner epitaxial $Ni_{80}Fe_{20}$ films than polycrystalline ones- suggest that islanding occurs in the early stages of film growth. Furthermore, it has been shown to occur in systems with comparable misfit in the initial stages of epitaxial growth[26, 27]. Assuming that, coherent islanding leads to a sinusoidal surface profile $h(x)$ defined by

$$h(x) = h_o + \Delta \sin\left(\frac{2\pi x}{\lambda}\right), \tag{5.31}$$

where Δ and λ are the amplitude and wavelength of the fluctuations in the thickness of the film due to islanding, respectively, and h_o is the average thickness of the film. As demonstrated in Eq. (5.25), H_c depends on the spatial derivative of the film thickness fluctuations, i.e., it depends on the wavelength of these fluctuations as well. Hence, from the above equation, it follows that:

$$\frac{dh}{dx} = \frac{2\pi}{\lambda}\Delta \cos\left(\frac{2\pi x}{\lambda}\right). \tag{5.32}$$

The relevant macroscopic quantity in esitmating H_c corresponding to these microscopic variations, would be the rms spatial average of the above equation, i.e.,

$$\left\langle \frac{dh}{dx} \right\rangle = \frac{\Delta}{\sqrt{2}} \frac{2\pi}{\lambda}. \tag{5.33}$$

Substituting this expression for $< dh/dx >$ in Eq. (5.25), we obtain:

$$H_c^{rough} = \frac{\gamma}{2M_s h} \frac{\Delta}{\sqrt{2}} \frac{2\pi}{\lambda}. \tag{5.34}$$

The dependence of Néel wall energy γ on film thickness is calculated in Appendix B, whereas the wavelength λ of coherent islanding was shown to scale as $8E\gamma_{surf}/\sigma_{||}^2$ as shown in Sec. 5.2. For film thickness in the range

of $0 < h < 20$ nm, the Néel wall energy increases almost linearly with film thickness and can be approximated as $\pi h M_s^2$ as shown in Appendix B (also see Fig. B.3). With this approximation, Eq. (5.34) becomes:

$$H_c^{rough} \cong \frac{\pi^2}{8\sqrt{2}} \frac{M_s \Delta \sigma_{\|}^2}{\gamma_{surf} Y} = \frac{\pi^2}{8\sqrt{2}} \frac{M_s \Delta e_{\|}^2 Y}{\gamma_{surf}(1-\nu)^2}, \tag{5.35}$$

where use has been made of the relation $\sigma_{\|} = \frac{Y}{1-\nu} e_{\|}$ from linear elasticity theory. Substituting $\Delta = 0.5$ nm as typically indicated by AFM measurements, $M_s = 800$ emu/cm^3 and $\lambda = 100$ nm as the coherent islanding wavelength for $Ni_{80}Fe_{20}$ film growth on Cu, in Eq. (5.35), the contribution to H_c due to surface roughening was estimated to be:

$$H_c^{rough} \cong \frac{\pi^2}{\sqrt{2}} \frac{0.5 \times 800}{100} \cong 28 \text{ Oe}. \tag{5.36}$$

A more accurate estimate of H_c^{rough} was made, taking into account the exact value of γ as calculated in Appendix B and is plotted in Fig. 5.14(b) along with the experimentally observed coercivity. The reasonably good agreement between experiment and theory suggests that this mechanism is more likely to be responsible for the higher H_c observed experimentally. This roughening due to coherent islanding might be suppressed by decreasing the misfit between $Ni_{80}Fe_{20}$ and the underlayer such as $Cu_{35}Ni_{65}$, as discussed in the last section. Figure 5.15 shows the variation of H_c^{rough} as calculated for misfit between $Cu_{35}Ni_{65}$ and $Ni_{80}Fe_{20}$ with experimentally observed values superimposed.

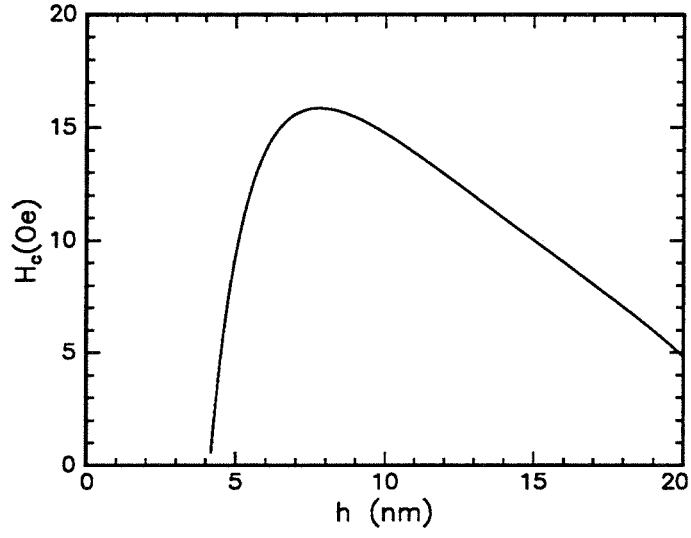

(a)

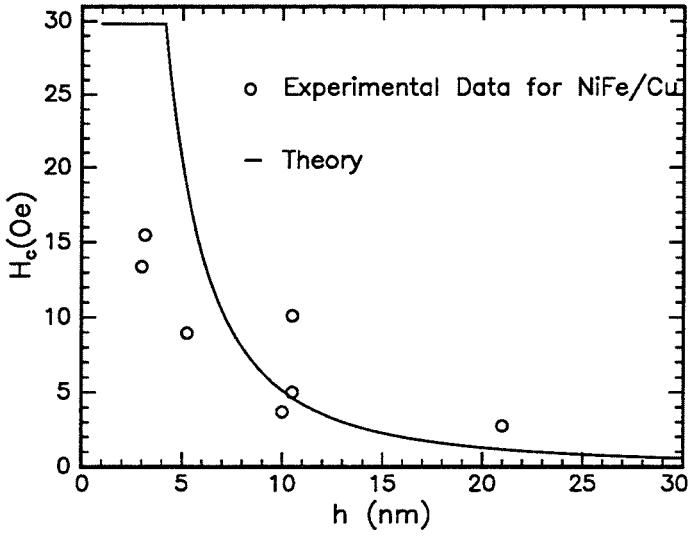

(b)

Figure 5.14: Film thickness dependence of H_c computed by assuming that strain fluctuations are caused by (a) misfit dislocations and (b) coherent islanding. Experimentally observed H_c is superimposed on the plot in (b).

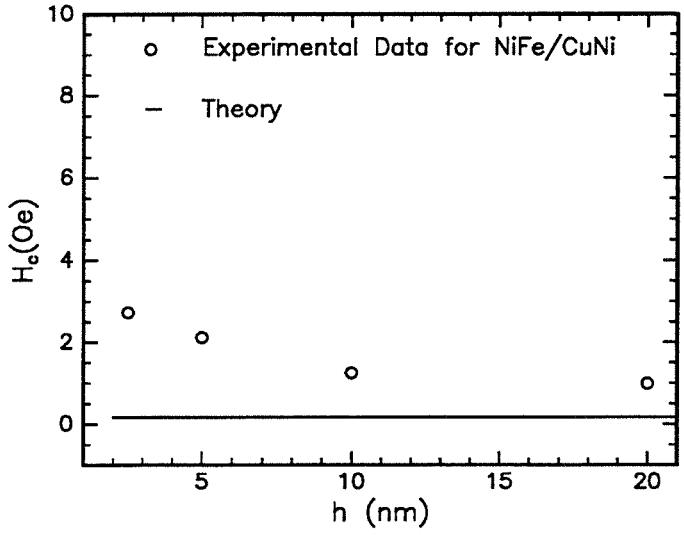

Figure 5.15: Variation of H_c due to coherency strain-induced islanding with $Ni_{80}Fe_{20}$ film thickness for epitaxial growth on $Cu_{35}Ni_{65}$. Experimentally observed data is superimposed.

5.8 Magnetotransport Properties of Epitaxial and Polycrystalline $Ni_{80}Fe_{20}$ Films

5.8.1 Instrumentation

The sheet resistance as well as magnetoresistance measurements were made at room temperature using a four point probe geometry. This setup was assembled by Dr. Hyun Sung Joo and its schematic is shown in Fig. 5.16. The probe spacing was 1/16 inch and corrections were made to account for the finite sample size in calculating the sheet resistance. These measurements were calibrated using a 250 nm thick Pt film deposited on SiO_2/Si whose sheet resistance was independently measured with a microprobe. The current source consisted of a 25 V/1 A power supply with a current stability of $\sim$ 10 nA. The voltage was measured using the data acquisition board installed in a model 386 personal computer which was also used for MOKE data acquisition. For magnetoresistance measurements, a Helmholtz coil pair consisting of 250 turns and coil separation of 12 cm was utilized to generate a magnetic field up to 100 Oe at the sample. Precautions were taken to ensure that there were no components of the four point probe which were magnetic. The power supply used for MOKE Helmholtz coils was used for sweeping the magnetic field for magnetoresistance measurements as well. The sweeping frequency was kept below 0.1 Hz to ensure that there were no eddy currents in the sample. Magnetoresistance measurements were typically made parallel, perpendicular and at 45° to the easy axis of the sample. Data acquisition software similar to the one used for MOKE measurements was used to measure the voltage drop across the sample as a function of magnetic field.

Figure 1.2 shows a plot of the magnetoresistance measurements made with this tool for a $Ni_{80}Fe_{20}$ film deposited on SiO_2/Si(001). Magnetoresistance of some samples was also measured at IBM Almaden using a similar setup.

5.8.2 Results

Analogously to the resistivity of thin films, the magnetoresistance of thin films is very sensitive to structural properties as well as purity of the film. Furthermore, $Ni_{80}Fe_{20}$ gets oxidized readily upon exposure to air. To prevent that, the $Ni_{80}Fe_{20}$ films for magnetoresistance measurements were capped with 2 nm of Ta or 1 nm of Cu. The resistivity of the as-deposited polycrystalline capped $Ni_{80}Fe_{20}$ films with thickness $\geq$ 10-100 nm was typically 25-40 $\mu\Omega$-cm whereas the magnetoresistance ratio (MR=$\Delta R/R$) varied from 0.5-1.5%. The resistivity and MR of bulk $Ni_{80}Fe_{20}$ are 14 $\mu\Omega$-cm and 2.1%, respectively. The higher resistivity and lower MR for the polycrystalline films may be due to the incorporation of Ar in the film as a consequence of the sputtering process. Annealing of these films can lower the resistivity and enhance the MR[9, 41].

The epitaxial $Ni_{80}Fe_{20}$ films were deposited on 10-50 nm thick Cu seed layers. The resistivity of the Cu films ranged from 2.5-9.5 $\mu\Omega$-cm, depending on thickness and deposition parameters (the resistivity of bulk Cu is 1.8 $\mu\Omega$-cm). As a result, it was difficult to extract the resistivity and magnetoresistance of $Ni_{80}Fe_{20}$ overlayers due to some of the current shunting through the Cu film. However, in this section, we compare the resistivity and magnetoresistance of a 100 nm thick epitaxial $Ni_{80}Fe_{20}$ film on a 10 nm Cu underlayer of known resistivity with those of a polycrystalline film of the same thickness. The

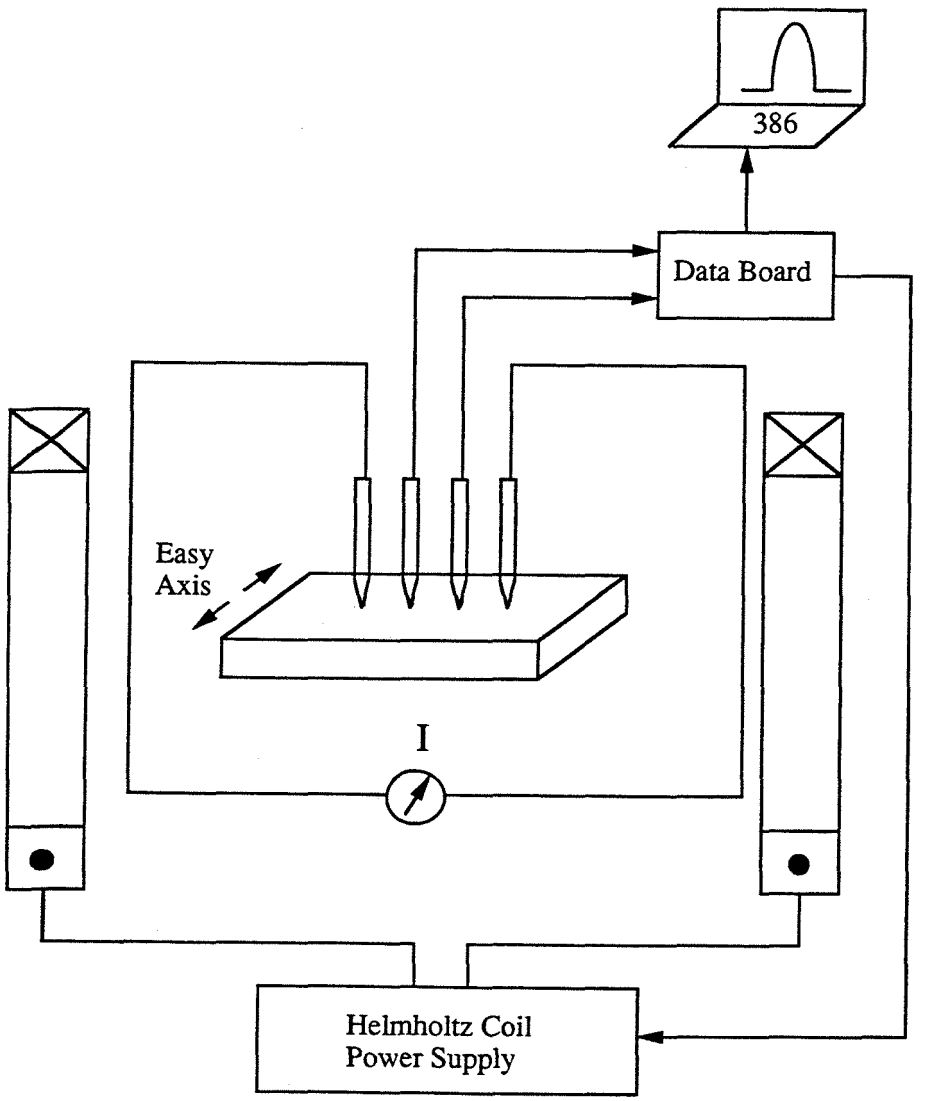

Figure 5.16: Schematic of the setup used for magnetoresistance measurements.

resistivity of the 10 nm thick Cu underlayer was measured using a different sample and was found to be 9.5 $\mu\Omega$-cm. Taking the resistance of the Cu underlayer into account, the resistivity of the epitaxial film was estimated to be 25.1 $\mu\Omega$-cm which is significantly lower than that of the polycrystalline film (31.7 $\mu\Omega$-cm). On the other hand, the magnetoresistance of the epitaxial and the polycrystalline films were 0.49% and 0.48%, respectively. Thus, the magnetoresistance of these films is relatively insensitive to the microstructure of these films. The cause of lower MR in these films than bulk $Ni_{80}Fe_{20}$ is probably due to the presence of Ar and other defects incorporated in these films during film growth. Figure 5.17 shows the magnetoresistance and resistivity of a polycrystalline $Ni_{80}Fe_{20}$ film as a function of annealing temperature. The lowering of the resistivity and increase in magnetoresistance with annealing supports the above hypothesis. The annealing of the epitaxial $Ni_{80}Fe_{20}$ film at 200°C for 1-hour also led to an increase in the magnetoresistance from 0.49% to 0.89%. X-ray diffraction of the annealed sample indicated lowering of the Cu(200) peak intensity compared with the unannealed sample whereas the NiFe(200) peak intensity was unaffected. This suggests partial consumption of the Cu underlayer to form a silicide without any effect on the crystallographic structure of the overlying $Ni_{80}Fe_{20}$ film. However, Cu and Ni as well as Cu and Fe, form a solid solution and interdiffuse at relatively low temperatures[42]. Significant lattice diffusion starts at 400°C and it is likely that grain boundary-mediated interdiffusion occurs at even lower temperatures. Thus, there may be undesirable interdiffusion during annealing of $Cu/Ni_{80}Fe_{20}$ bilayers as well as multilayers.

To reduce the shunting current due to the Cu underlayer in epitaxial

$Ni_{80}Fe_{20}$ films, underlayers as thin as 5.0 nm might be used. Furthermore, as discussed in Sec. 5.7.1, Cu_xNi_{1-x} alloyed films may be used in conjuntion with a Cu underlayer even thinner than 5.0 nm. The Cu_xNi_{1-x} films, besides providing a better lattice match to $Ni_{80}Fe_{20}$, also have higher resistivity than $Ni_{80}Fe_{20}$, as Cu and Ni do not form a common d-band[8]. This would reduce the shunting current in the epitaxial $Ni_{80}Fe_{20}$ films on Si, and result in lower resistivity as well as higher MR.

5.9 Conclusions

Epitaxial (001) $Ni_{80}Fe_{20}$ films with atomically-abrupt interfaces were grown on Si(001) utilizing epitaxial growth of Cu on Si. Magnetic properties of these films were investigated *in situ* and were found to be sensitive to the misfit strain between the $Ni_{80}Fe_{20}$ film and the Cu seed layer. H_c was observed to be significantly higher for < 10 nm thick epitaxial $Ni_{80}Fe_{20}(001)$ films deposited on a 50 nm thick Cu seed layer on Si, as compared with polycrystalline films of the same thickness. However, relatively thicker (≥ 20 nm) epitaxial $Ni_{80}Fe_{20}$ films or those grown on lattice matched Cu_xNi_{1-x} alloys had soft magnetic properties comparable to those of polycrystalline films. This suggests that the reduction of coherency strain due to the mismatch between $Ni_{80}Fe_{20}$ and Cu improves its soft magnetic properties. Theoretical models to explain the variation of H_c with thickness suggest that the higher H_c is more likely to be caused by coherency strain-induced surface roughness rather than misfit dislocations. Finally, the magnetoresistances of the polycrystalline and the epitaxial films were comparable and lower than that for

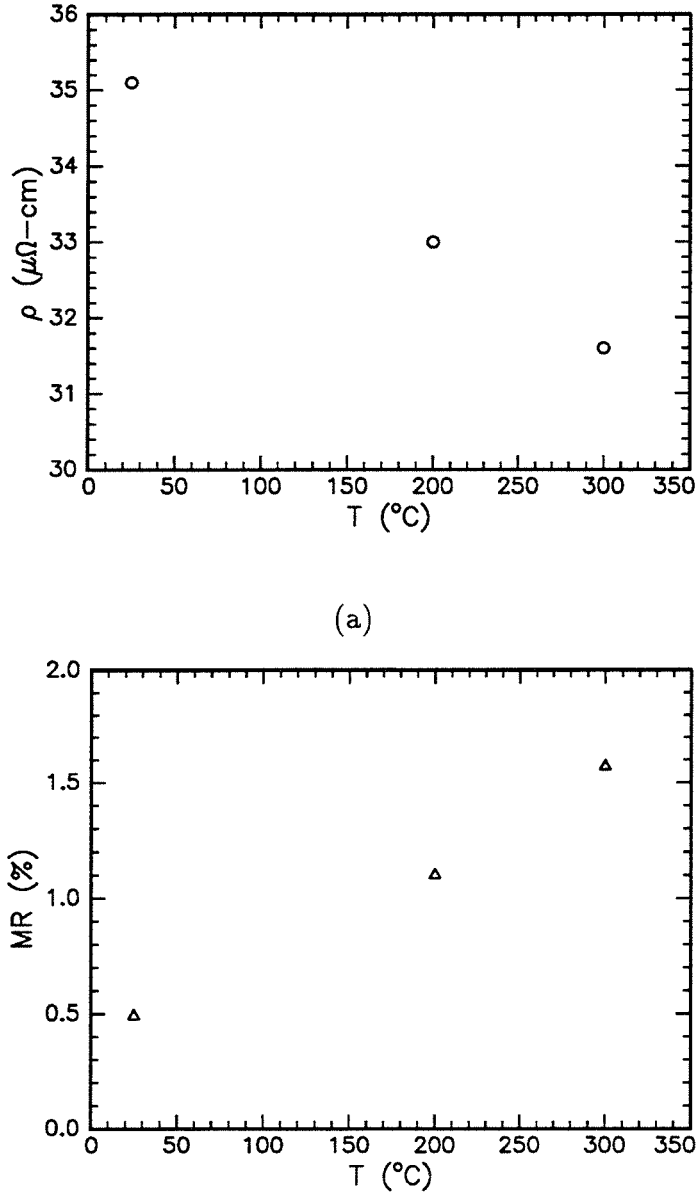

Figure 5.17: Variation of (a) resistivity and (b) magnetoresistance of polycrystalline $Ni_{80}Fe_{20}$ film as a function of temperature for 1 hour anneals.

bulk $Ni_{80}Fe_{20}$ possibly due to Ar incorporated during film growth. However, annealing of these films at relatively low temperatures (200-300°C) can enhance the MR to its bulk value. Furthermore, the resistivity of the epitaxial films was significantly lower than that for the polycrystalline films, suggesting that the epitaxial films had lower grain-boundary density which might be an important consideration for magnetoresistive devices applications.

Bibliography

[1] P. Grunberg, A. Schreiber, Y. Pang, M.B. Brodsky, and H. Sowers, Phys. Rev. Lett. **57**, 2442 (1986).

[2] S.S.P. Parkin, Appl. Phys. Lett. **60**, 512 (1992).

[3] B. Dieny, V.S. Speriosu, B.A. Gurney, S.S.P. Parkin, D.R. Wilhoit, K.P. Roche, S. Metin, D.T. Peterson, and S. Nadimi, J. of Magn. and Magn. Mater. **93**, 101 (1991).

[4] M. van Schilfgaarde and W.A. Harrison, Phys. Rev. Lett. **71**, 3870 (1993).

[5] M.T. Johnson, R. Coehoorn, J.J. de Vries, N.W.E. McGee, J. aan de Stegge, and P.J.H. Bloemen, Phys. Rev. Lett. **69**, 969 (1992).

[6] P.M. Levy, S. Zhang, and A. Fert, Phys. Rev. Lett. **65**, 1643 (1990).

[7] B. Dieny, Europh. Lett. **17**, 261 (1992).

[8] I.A. Campbell and A. Fert, "Transport Properties of Ferromagnets," in *Ferromagnetic Materials*, ed. by E.P. Wohlfarth,

[9] A.F. Mayadas and M. Shatzkes, Phys. Rev. B **1**, 1382 (1970).

[10] R.F.C. Farrow, S.S.P. Parkin, and V.S. Speriosu, J. Appl. Phys. **64**, 5315 (1988).

[11] J. Thomassen, F. May, B. Feldman, M. Wuttig, and H. Ibach, Phys. Rev. Lett. **69**, 3831 (1992).

[12] H.E. Inglefield, C.A. Ballentine, G. Bochi, S.S. Bogomolov, R.C. O'Handley, and C.V. Thompson, Mater. Res. Soc. Proc. Vol. **308**, (1993).

[13] J.W. Matthews and J.L. Crawford, Thin Solid Films **5**, 187 (1970).

[14] P. Hansen, *Constitution of Binary Alloys*, (McGraw-Hill, New York, 1958), p. 1045.

[15] M.H. Kryder and F.B. Humphrey, J. Appl. Phys. **42**, 1808 (1971).

[16] R.D. Burbank and R.D. Heidenreich, Phil. Mag. **5**, 373 (1960).

[17] U. Gradmann and J. Muller, J. Appl. Phys. **39**, 1379 (1968).

[18] W.F. Egelhoff, Jr. and M.T. Kief, IEEE Trans. Mag. **28**, 2742 (1992).

[19] H.S. Joo, I. Hashim, and H.A. Atwater, work in progress.

[20] J.W. Matthews and A.E. Blakeslee, J. Cryst. Growth. **27**, 118 (1974).

[21] J.Y. Tsao, *Materials Fundamentals of Molecular Beam Epitaxy* (Academic Press, San Diego, 1993), Ch.5.

[22] D. Hull and D.J. Bacon, *Introduction to Dislocations*, 3rd Ed., (Permagon Press, Oxford, U.K., 1984).

[23] R.C. O'Handley and Ohsung Song, submitted to J. Appl. Phys., Nov. 1993.

[24] J.D. Eshelby, Proc. R. Soc. **A241**, 376 (1957); **A252**, 561 (1959).

[25] D.J. Srolovitz, Acta. Metall. **37**, 621 (1989).

[26] A.G. Cullis, D.J. Robbins, A.J. Pidduck, and P.W. Smith, Mat. Res. Soc. Symp. Vol. **280**, 383 (1993).

[27] P.R. Berger, K. Chang, P. Bhattacharya, J. Singh, and K.K. Bajaj, Appl. Phys. Lett. **53**, 684 (1988).

[28] A. Zangwill, *Physics at Surfaces*, (Cambridge University Press, Cambridge, U.K., 1988).

[29] A.P. Payne, B.M. Clemens, and S. Brennan, Rev. Sci. Instrum. **63**, 1147 (1992).

[30] C. Kittel, Rev. Mod. Phys. **21**, 541, 1949.

[31] B.D. Cullity, *Introduction to Magnetic Materials*, (Addison-Wesley, Philippines, 1972), Ch.8.

[32] E. Klokholm and J.A. Aboaf, J. Appl. Phys. **52**, 2474 (1981).

[33] A.C. Tam and H. Schroeder, IEEE Trans. Mag. **25**, 2629 (1989).

[34] J.G. Gay and Roy Richter, Phys. Rev. Lett. **56**, 2278 (1986).

[35] D. Weller, W. Reim, K. Sporl, and H. Brandle, J. Magn. Magn. Mater. **93**, 183 (1991).

[36] P. Bruno and J.-P. Renard, Appl. Phys. A **49**, 499 (1989).

[37] T. Suzuki and C.H. Wilts, J. Appl. Phys. **38**, 1356 (1967).

[38] M. Prutton in *Thin Ferromagnetic Films*, Butterworth & Co., England, 1964.

[39] L. Néel, J. Phys. Radium **17**, 250 (1956).

[40] S. Middelhoek, Ph.D. Thesis, Amsterdam, 1961.

[41] S. Krongelb, A. Gangulee, and G. Das, IEEE Trans. Magn. **9**, 568 (1973).

[42] C.A. Mackliet, Phys. Rev. **109**, 1964 (1958).

Appendix A

More Details of the Instrumentation

A.1 Design and Operation of the MOKE system

A.1.1 Hardware

As soft magnetic materials like Permalloy require only a few Oersteds to magnetize, great care was taken to isolate the MOKE quartz tube from stray magnetic fields due to magnets in the ion gun and the rest of the sputtering system. In particular, the glass-to-metal seals utilized to interface the quartz tube to the sputtering system contain paramagnetic impurities which can contribute to the depolarization of the light. Furthermore, they are magnetostrictive, i.e., magnetic fields can lead to development of stresses in them. At least 4" of quartz separated these seals on all sides from the center of the tube where the MOKE analysis was done.

A Helmholtz coil pair was used to magnetize the sample. The radius of the coils and their separation was chosen to be sufficiently larger than the

sample size so that the field over the sample surface was fairly uniform. Two hundred turns of 18 AWG magnet wire from MWS Industries were wound around two hollow cylinders made of phenolic. The cylinders had a 10 cm outer diameter and were 2" long. The magnetic field H in Oersteds at the center of an ideal Helmholtz coil pair with separation $2R$ is given by[1]:

$$H = \frac{2\pi NI}{10R} \tag{A.1}$$

where N is the number of turns, I is the current in amperes, and R is also the radius of the coils in cm. In reality, the wires have a finite thickness, and not all the turns are located at the same radius. To account for these nonidealities, Eq. (A.1) is replaced by more sophisticated versions which typically require calculations on a computer. Furthermore, the separation of our Helmholtz coils was 20% greater than the ideal separation due to constraints imposed by the quartz tube thickness. As a result, the actual field was smaller than that predicted by Eq. (A.1). However, a sensitive Hall probe was used to calibrate the actual magnetic field obtained. For a current of 5 amperes, a field of 75 Oersteds was obtained, which is 50% less than the field predicted by Eq. (A.1).

On the other hand, the self-inductance L of the coils is given by

$$L = \frac{N\phi}{i} \tag{A.2}$$

where $\phi = \int B \cdot dA = B\pi R^2$ is the magnetic flux passing through the coils. For a current of 5 amperes, Eq. (A.2) implies a self-inductance of 0.025 Henry and hence a reactance (ωL) of 0.78 Ω at a frequency of 10 Hz. Now, the DC resistance of the two hundred turns of magnet wire is 2.64 Ω so that for a

frequency of 10 Hz, the impedance of the coils is 2.75 Ω which implies a voltage drop of $5 \times 2.75 = 13.75$ volts. The Kepco power supply used was rated at 20V/10A so that it was adequate for these loads. However, at a frequency of 100 Hz, the impedance of the coils would be 8.2 Ω implying a voltage drop of 41 volts at 5 amperes. Thus, it would not be possible to use this power supply at frequencies higher than 50 Hz. Furthermore, the maximum current that can be passed through the #18 wire is about 5 amperes so that the maximum field that can be obtained with these coils is about 75 Oersteds.

In Kerr magnetometry, H_c is obtained by converting the coil current to an applied field H. Thus, it is extremely important that the coil current is in phase with the magnetic flux measurements, i.e., Kerr rotation measurements. In particular, phase difference between current and voltage due to the inductance of the coils can give rise to as much as 50% error in H_c. This phase error was compensated in the software by taking into account the inductance of the coils as calculated above. An alternate method to take care of that would be having a resistor in series with the coils and using the current in the resistor to calculate the applied field. Vibrating sample magnetometry (VSM) was employed to confirm the H_c measurements made using our Kerr system. In particular, H_c was measured along at least three crystallographic directions for (100) $Ni_{80}Fe_{20}$ films on Cu/Si (along [100], [110] and [010]) using both VSM and MOKE for up to three samples. The MOKE H_c measurements were thus found to be accurate to within 10%.

The resolution of our *in situ* MOKE system was limited by noise arising from lack of proper vibration isolation of the system. In particular, low fre-

quency building noise (at a few Hz) was noticeable. It might be eliminated by installing the sputtering system on a proper vibration-isolated table. The noise due to mechanical pumps was reduced significantly by physically separating the pumps from the rest of the system and using vibration isolators for mechanical pumps. Some of the vibration noise was eliminated by signal averaging in the software which is discussed in the next section. Another source of noise was the ubiquitous 60 Hz noise coming mainly from the fluoroscent lights in the room. This noise was reduced by switching off most of these lights during data acquisition and might be further reduced by building a light-tight enclosure for the photodetectors. A slightly different configuration for making MOKE measurements involving a photoelastic modulator and a lock-in amplifier, might have less noise and better resolution[2]. However, the cost of that MOKE configuration may be significantly higher due to the additional cost of the photoelastic modulator and the lock-in amplifier.

Finally, the laser, photodetectors and the circuitry for their amplifiers can also be a source of noise in the MOKE system. The 670 nm 10 mW semiconductor diode laser used was found to be sufficiently stable and to have enough power. However, the semiconductor laser beam has some inherent astigmatism and divergence due to the geometry of the edge-emitting lasers. This astigmatism was reduced by adjusting the lens already packaged with the laser and installing another cylindrical lens after the reflected beam. Planar diffused silicon photodiodes packaged with a built-in amplifier and an active area of 20 mm^2 (model UDT-020D) from United Detector Technology were used for detection of the rotation in polarization after reflection. These photodetectors are typically operated in two modes, photovoltaic (PV)

and photoconductive (PC). In the latter mode, the photodetector is reverse-biased, resulting in smaller junction capacitance and hence faster response time ($\sim \mu s$). However, this results in increased noise level due to the higher leakage current in reverse bias. In PV mode, no external bias is applied to the photodetector so that noise level is lower at the expense of slower response time. Since our application required operation at relatively low frequencies and lower noise levels, PV mode was used instead of PC (see Fig. A.1 which shows the electical schematic of the photodetector and the amplifier circuitry). The amplifier consisted of an op-amp which required a DC voltage supply of $\pm$15 V. The gain of the amplifier was controlled by a feedback resistor R_f and a feedback capacitor C_f connected externally. An appropriate value of 250 nF was chosen for C_f to allow operation at $\leq$ 100 Hz whereas a 1-10 kΩ variable resistor was used as the gain resistor. This gave a voltage signal of 1-10 V corresponding to the maximum input laser power of 10 mW. A variable resistor of 100 kΩ was connected externally to adjust the null offset of the photodetector (typically 0.5 mV with a maximum of 3 mV) to zero. The 0.1 μF capacitors connected in parallel to the $\pm$ 15 V dc power supply were for shunting any ac noise in the dc power supply from the op-amp.

The output from the photodetectors was directly connected to two of the eight analog input channels of the DT2821 board, each with 12 bit resolution (see Fig. A.2 for a schematic of the board). The voltage range that is measured by the board with the highest programmable gain, is $\pm$ 1.25 V. Thus, the smallest voltage signal that can be resolved by the board is $2.5V/2^{12} = 0.6$ mV. The board also had a digital-to-analog converter (DAC)

which provided an analog output used as the input control signal to the coil power supply. The control signal from the DAC to the power supply consisted of a sinusoidal signal of appropriate amplitude and frequency. This configuration worked out better than controlling the IEEE-488 board installed in the power supply, via the 16 digital I/O lines also available on the board. That would have involved installation and programming of another board IEEE-488 board in the computer to allow communication/handshaking between the power supply and the computer.

Furthermore, the board also had a programmable gain amplifier for analog inputs which can be chosen to have gains of 1, 2, 4 or 8. This allowed the amplifier gain to be changed in the software rather than in the photodetector gain circuit, for different sample reflectivities and hence different photodetector outputs. The maximum throughput of this board was 50 kHz; hence, it would not be feasible for higher data acquisition frequencies. Another limitation of this board is that the analog inputs were not read simultaneously into the computer. In other words, the time elapsed between the two input signals being read into the board, was 1/50 kHz = 20 μs. Hence, this board might not be appropriate for data acquisition at frequencies higher than 1 kHz. A better board choice for faster data acquisition would be model DT2831 which simultaneously "grabs" signals from all the 8 input data channels. However, the highest frequency for data acquisition was limited by the coil inductance or the voltage-limitations of the coil power supply, as discussed above. Furthermore, the response time of the power supply is 0.01 ms. Thus, if there were 100 points in one loop, this would imply a maximum data acquisition frequency of 1 kHz. Due to reasons mentioned above, the MOKE data was

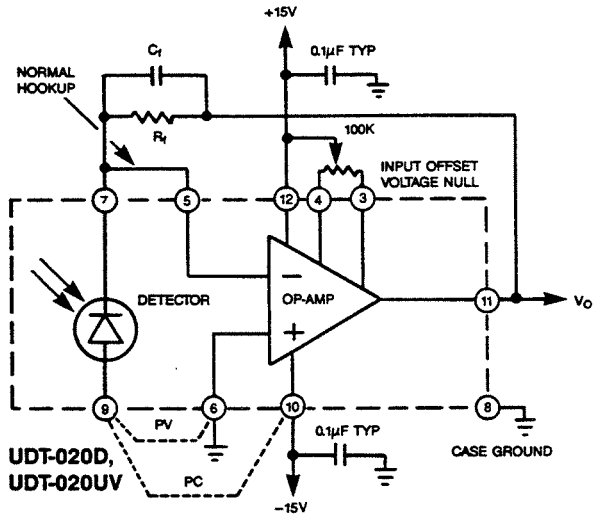

Figure A.1: Electrical schematic of the photodetector and the amplifier. The dashed rectangle represents the packaged photodetector and the op-map whereas the encircled numbers represent external pin connections to the photodetector.

acquired at $\leq$ 10 Hz.

A.1.2 Software

The software for data acquisition was written in C, Version 6.0. It consisted of three subprograms, the main program *am.c*, *dt*2821.*c* which controlled the DT2821 board, and *amgraph.c* which contained the graphic routines for the program. Originally, we thought that ATLAB Software, purchased from Data Translation along with the board, might save us trouble because it contained routines which can perform lower-level functions on the board and can be directly accessed from a higher level language such as C, Pascal or Fortran. However, the routines available were not specific enough for our

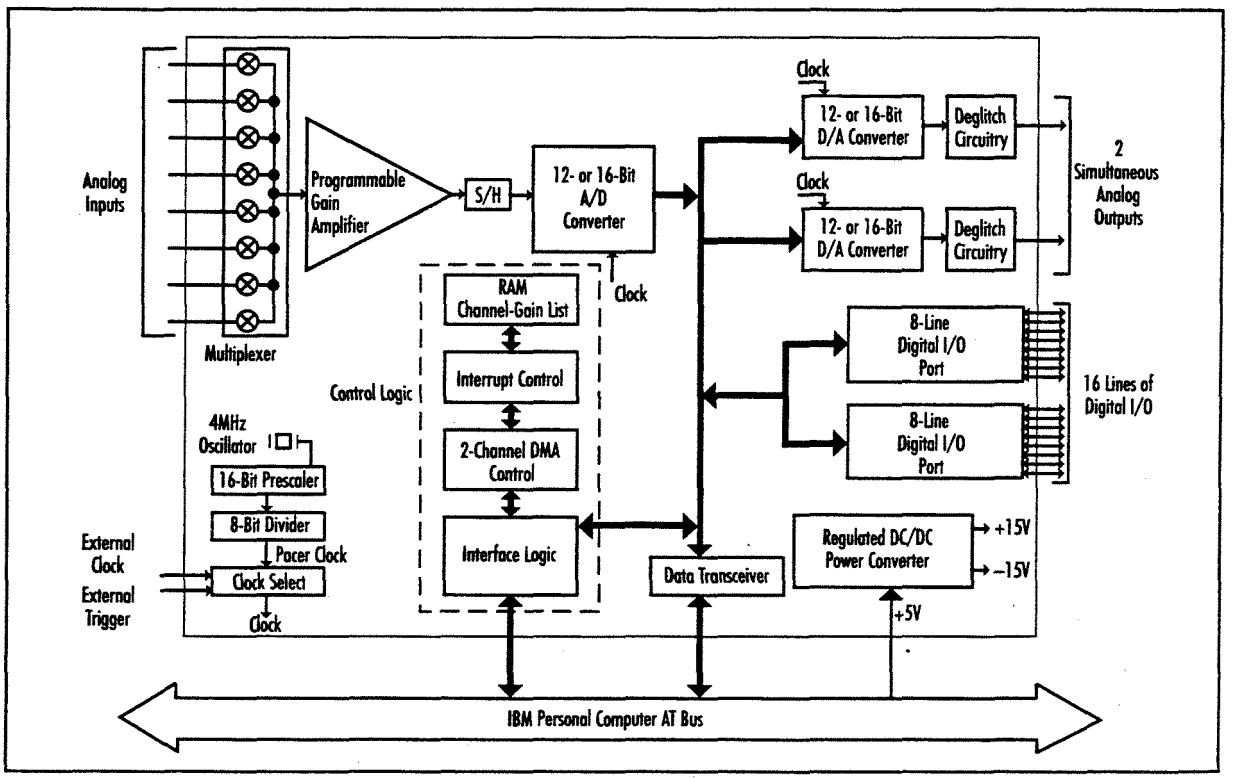

Figure A.2: Block diagram of the DT2821 board used for MOKE experiment's data acquisition.

application so we ended up writing our own routines for data manipulation on the board. Interrupts generated by the computer signalled the board to transfer the data from the I/O channels to the buffer on the board and then to the computer memory. These interrupts were spaced as closely as possible (i.e., within 1 clock cycle) to read the analog signals from the two photodetectors. The board then waited for the next input signal until the current in the coil power supply was changed to its next value. There were typically 1000 points in a B-H loop, and the data acquisition frequency was 0.1-1 Hz in order to avoid the higher frequency noise.

The graphics routines used were those of DOS to minimize the time required for plotting the data. In fact for $f \leq 10$ Hz, real time display of the hysteresis loop was possible. However, the raw data for less than 10 nm thick films typically did not have a very high signal-to-noise ratio but that noise was reduced considerably by averaging over up to 100 loops. At a frequency of 1 Hz, this would imply acquiring data for 100 s. Some efforts were made to eliminate the flickering of the screen as it was cleared after each hysteresis loop cycle. However, this "bug" still remains undebugged.

The main program *am.c* was responsible for controlling the interactive menu for the program as well as the data acquisition parameters which included the data acquisition frequency, coil current amplitude, and the programmable gain. As mentioned earlier, the phase error due to the inductance of the coils was calculated using expressions analogous to Eq. (A.1) and (A.2) and compensated for during hysteresis loop plotting. Finally, as pointed out in Sec.2.3, the hysteresis loop obtained using MOKE is actually a Kerr loop rather than a B-H loop, as the Kerr rotation is only quasilinear with the mag-

netization of the sample. It might not be too difficult to implement a routine which could convert the Kerr rotation to the actual magnetization. However, the relationship between the two is fairly complex and requires lengthy matrix calculations on Mathematica. Therefore, in order to cut down computation during data acquisition, it might be easier to implement a lookup table with values of the Kerr rotation and actual magnetization for every 10 nm of the film thickness and interpolating for intermediate values.

The software also had a routine which displayed the output of the two photodetectors as bars. This allowed adjustment of the quarter-wave plate to get the desired polarization of the reflected light (see next section for more details).

A.1.3 Operation and Suggestions for Improvement

For reasons mentioned in Sec.2.3, the incident polarization of the light was chosen to be s. After reflection, a quarter-wave plate was used to split the light into equal amounts of s and p polarizations, making use of the MOKE software routine which displays the detector output as bars. Furthermore, the quarter-wave plate allowed elimination of the Kerr ellipticity and enhancement of the Kerr rotation for this orientation, as discussed in Sec.2.3. However, due to the divergence of the laser beam, the beam spot on the detector was almost the same size as the active area of the detector. This led to somewhat noisier Kerr loops when the sum-and-difference signal of the two photodetectors, i.e., $\frac{A-B}{A+B}$ was plotted. Less noisy loops were obtained when output from only one photodetector was plotted while keeping the intensity of the light on that photodetector relatively small. When the output of only

one photodetector is used to obtain the Kerr loop, care should be taken to convert the Kerr rotation to magnetization as it will be dependent on the gain of the pre-amp as well as the incident laser power. Using photodetectors with larger active area may make it feasible to use the sum-and-difference signal from both the detectors. As some of the divergence of the laser beam is a consequence of scattering from the quartz tube, it may not be easy to compensate for that divergence using simple lenses.

For a typical Kerr measurement, the coil current amplitude and frequency were 3 A and 0.1 Hz, respectively, with signal averaging over 100 loops. Kerr loops were obtained for both easy and hard axes of the NiFe films. In the case of epitaxial (100) films, Kerr loops were measured along the [100], [110] and [010] crystallographic directions.

A.2 SAXD system: Operation and Current Status

A.2.1 Operation

As mentioned in Sec. 2.5.1, the higher satellites in the small angle x-ray spectrum were quite sensitive to the alignment of the sample and the diffractometer with respect to the main x-ray beam. To align the sample accurately, the following procedure was used:

1. The goniometer was set to 0° and the x-ray power supply was set to the lowest voltage and current levels for which x-ray emission could be obtained. This was done to prevent the x-ray detector from damage due to an excessively strong x-ray beam.

2. Using the high resolution translation stage, the sample was translated forward until the x-ray beam was partially blocked by the sample.
3. The high resolution rotation stage was adjusted to maximize the x-ray intensity.
4. Steps (2) and (3) were iterated until the x-ray intensity could not be maximized any further.
5. The sample was translated forward until the main beam was reduced to half its intensity.
6. Finally, a quick scan (with a short counting time of 3 s and a larger step size of 0.1°) was made to compare the SAXD satellite positions with those expected from OM simulations. If at least three SAXD satellites could be observed in such a scan, a longer scan with a smaller step size was made to obtain the final SAXD spectrum.

A.2.2 Current Status

As the age of the GE x-ray power supply exceeded the age of the untenured faculty members in the materials science department, it was thought best to replace it with a solid-state power supply from Inel. Furthermore, the tube tower was also replaced by one from Inel which had a graphite monochromator. Figure A.3 shows the schematic of the tube tower, monochromator, the sample holder, the diffractometer and the x-ray detector. The graphite monochromator can be adjusted with respect to the tube tower for the ap-

propriate x-ray radiation (typically Mo, Co or Cr). Highest x-ray intensity was obtained with the Mo tube whereas the Cr intensity was the lowest. The tube tower was mounted on translation stages and a lab jack which allowed accurate alignment of the main beam with respect to the goniometer. A x-ray fluorescent screen was used to ensure that the x-ray optics was properly aligned. Only with the Mo tube, strong fluorescence could be observed on the fluorescent screen as well as diffraction peaks from a powdered Si sample. It is possible that the diffraction peak intensities were low because the tube tower was not located at the diffractometer circle[3]. However, a SAXD spectrum could be obtained with all the radiation sources as SAXD does not require very high intensity levels.

A.3 Cu Epitaxy: What Worked and What Didn't

It would be unfair not to mention that obtaining Cu epitaxy on Si reproducibly from run to run was not easy. There was certainly an element of *luck* involved, as we were able to achieve epitaxial growth of Cu on Si on our first attempt but thereafter we were not able to reproduce it for up to 6 attempts. However, since then, we have acquired expertise in what deposition parameters the epitaxy is most sensitive to.

Residual moisture or hydrocarbons on the Si surface were definitely a factor, as the success rate for achieving Cu epitaxy was improved after installing a substrate heater in the sputtering chamber. A pre-deposition bake at 200° for 2 hours allowed the residual moisture and hydrocarbons to be desorbed

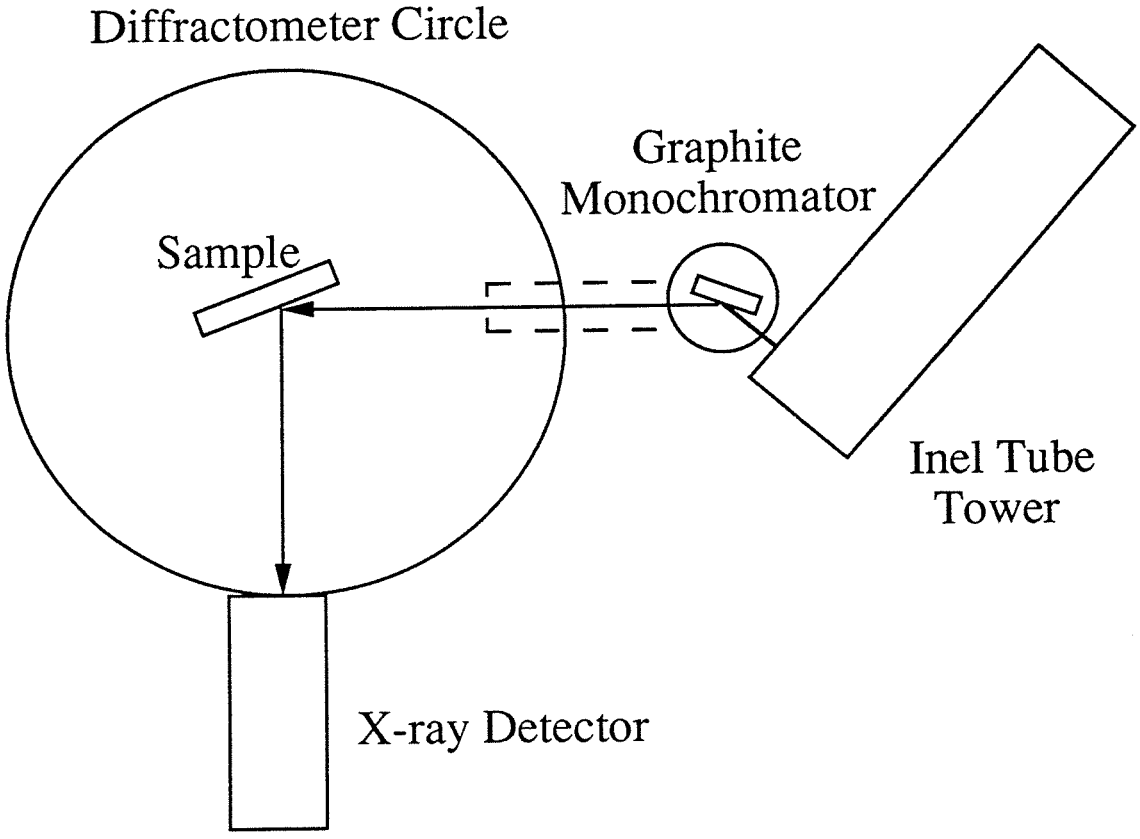

Figure A.3: Schematic of the Inel tube tower and the GE diffractometer for small angle x-ray diffraction measurements.

from the substrate. However, baking the sample at higher temperatures was sometimes deleterious as that led to outgassing from parts of the heater and the substrate holder. Ensuring that all parts of heater and the substrate holder are made from Mo or ceramic rather than stainless steel might solve the above problem. Furthermore, particulates on the Si surface were also a factor as the substrate cleaning was not carried in a clean room environment by any standards. Pieces of Si (usually 1" x 0.5") cut from Si(100) wafers were inspected under an optical microscope for particulates and only the relatively particulate-free ones were used.

The purity of the Cu film was also very crucial to achieving epitaxial growth on Si. Presence of $\leq 1\%$ Fe and/or C disrupted the epitaxy leading to (111)-textured polycrystalline film growth. The Fe impurities entered the Cu film when the ion gun was moved farther away from the sputtering system in an effort to isolate the RHEED beam from the magnets in the ion gun. As discussed in Sec.2.1, the ion beam expands into a Gaussian profile with distance due to charge repulsion. Thus, a fraction of the ion beam was possibly sputtering the walls of the chamber behind the target. This problem was solved by replacing the original 3 cm grid with a customized 2 cm ion-beam grid pattern, thus reducing the beam size. At another stage, the graphite grids in the ion gun were misaligned due to a crack in the screen grid which is the grid closer to the ion source than the accelerator grid. This resulted in erosion of the accelerator grid near the crack in the screen grid, leading to incorporation of C in the film and disruption of epitaxy.

Furthermore, the epitaxy was also very sensitive to the deposition temperature. For deposition at $T \geq 80°C$, a Cu_3Si film was obtained immediately

upon deposition, as indicated by absence of the RHEED pattern observed for an epitaxial Cu film. This suggests that it is vital for the sample to be cooled to room temperature after the pre-deposition bake, and the temperature to be measured accurately. Typically, in vacuum systems, cooling rates are very slow owing to poor thermal contacts and lack of cooling by convection. In order to increase the cooling rate, a LN_2 finger was added to the substrate holder. This consisted of a Cu braid wrapped around the sample holder and connected via an electrical feedthrough to a Cu braid outside vacuum dipped in LN_2.

Finally, at this point, we cannot clearly establish any correlation between Cu epitaxy and the chemical cleaning procedures for obtaining a H-terminated Si surface. However, it is possible that the concentration of hydroflouric acid used may also be a factor, as higher concentrations than 10% may contribute to greater etching of the Si, resulting in a rough surface.

Bibliography

[1] B.D. Cullity, *Introduction to Magnetic Materials*, (Addison-Wesley, Philippines, 1972), Ch.1.

[2] J.F. Dillon, Jr., E.M. Gyorgy, F. Hellman, L.R. Walker, and R.C. Fulton, J. Appl. Phys. **64**, 6098 (1988).

[3] B.D. Cullity, *Elements of X-ray Diffraction*, (Addison-Wesley, Philippines, 1978), Ch.6.

Appendix B

Domain Walls in Thin Films

The domain wall energy and thickness in bulk magnetic materials are governed mainly by exchange and anisotropy energy contributions. However, for thin films ($\leq$ 50 nm for NiFe), the rotation of magnetic moments in the domain wall takes place in the plane of the film as opposed to out of the film plane. The former type of domain wall, known as Néel wall, has lower magnetostatic energy than the latter type, known as Bloch wall. In the absence of magnetostatic contributions, the domain wall thickness is found by minimizing the exchange and anisotropy contributions to the total energy of the domain wall. Assuming that ϕ, the angle between neighboring spins in the domain wall, rotates linearly through 180°, we have

$$\phi = \pi \frac{x}{\delta} \quad \text{for } \frac{-\pi}{2} \leq \phi \leq \frac{\pi}{2} \tag{B.1}$$

where δ is the domain wall width. Assuming that the exchange energy exists only between neighboring spins, the exchange contribution becomes:

$$E_{ex} = J \left(\frac{d\phi}{dx} \right)^2 = J \left(\frac{\pi}{\delta} \right)^2, \tag{B.2}$$

where J is the exchange stiffness constant. On the other hand, contribution due to uniaxial anisotropy is given by:

$$E_K = K_u \cos^2\phi. \tag{B.3}$$

To get the total energy of the domain wall, the exchange and anisotropy energy contributions are integrated over the domain wall width, i.e.,

$$E_{tot} = \int_0^{\delta} (E_{ex} + E_K) dx. \tag{B.4}$$

Making use of Eq. (B.1), (B.2) and (B.3), the above equation can be written as:

$$E_{tot} = \int_0^{\delta} J \left(\frac{\pi}{\delta}\right)^2 dx + \int_{-\pi/2}^{\pi/2} \left(\frac{\delta}{\pi}\right) K_u \cos^2\phi d\phi = \frac{J\pi^2}{\delta} + \frac{\delta K_u}{2\pi}. \tag{B.5}$$

Minimizing the above expression with respect to δ yields the following expressions for the equilibrium domain wall width and domain wall energy, respectively:

$$\begin{aligned} \gamma &= \pi\sqrt{2}\sqrt{JK} \\ \delta &= \pi\sqrt{2}\sqrt{\frac{J}{K}}. \end{aligned} \tag{B.6}$$

For a thin film of thickness h, the magnetostatic contribution to a domain wall energy can be estimated by modeling the domain wall as an elliptic cylinder as shown in Fig.B.1[1]. The magnetostatic energy is then evaluated using the expression:

$$E_{ms} = -\frac{1}{2} H_d M_s = -\frac{1}{2} N_d M_s^2, \tag{B.7}$$

where H_d is the self-demagnetizing field and is related to the demagnetization factor N_d according to $H_d = N_d M_s$. For this elliptical geometry, it can be exactly evaluated using[2]

$$N_d = \frac{2\pi\delta}{\delta + h} \tag{B.8}$$

so that the surface energy of a Néel wall is given by:

$$\gamma_N = \frac{J\pi^2}{\delta} + \frac{1}{2}\delta K_u + \frac{\pi\delta h}{\delta + h} M_s^2. \tag{B.9}$$

Minimizing with respect to δ yields

$$\frac{d\gamma_N}{d\delta} = -\frac{J\pi^2}{\delta^2} + \frac{1}{2}K_u + \frac{\pi\delta h^2}{(\delta + h)^2} M_s^2 \equiv 0, \tag{B.10}$$

which has been solved numerically by Middelhoek[3] to find the domain wall thickness δ as a function of film thickness h. For the film thicknesses of interest here, $h \sim 10$ nm and $\delta \sim 100$ nm so that the magnetostatic contribution in Eq. (B.10) can be approximated as $\frac{\pi h^2}{\delta}$. Using this approximation, Eq. (B.10) can be solved analytically for δ as a function of h and its solution is plotted in Fig.B.2. Substituting the domain wall width thus calculated into Eq. (B.10) yields the equilibrium Néel wall energy γ_N, which is plotted as function of film thickness for $0 \leq h \leq 20$ nm in Fig.B.3.

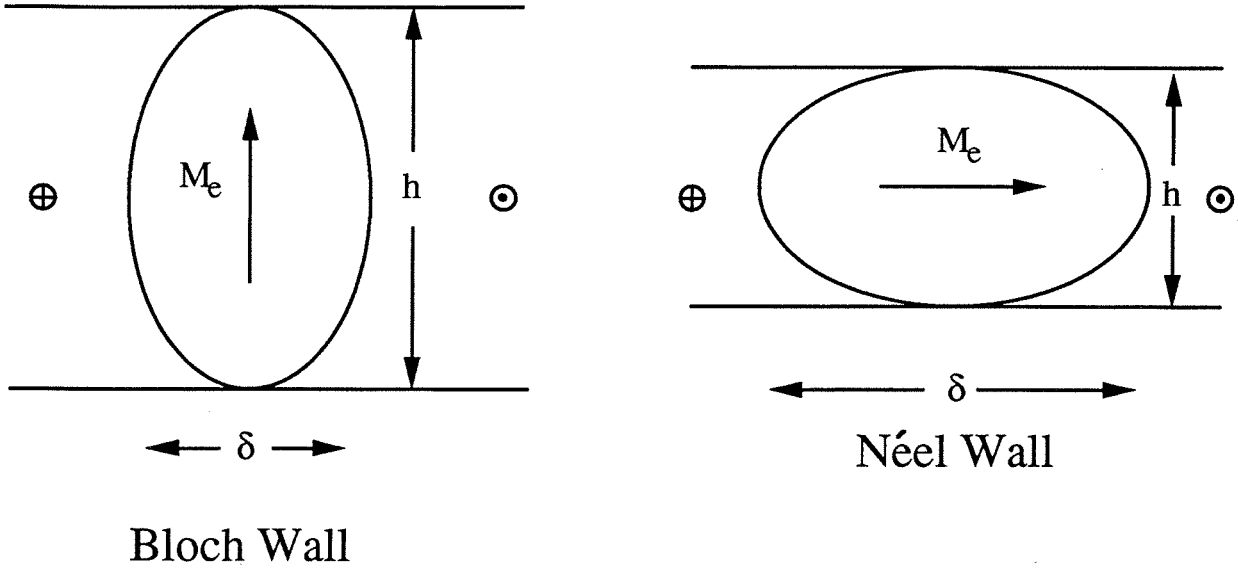

Figure B.1: Cross-section of Bloch and Néel walls according to the approximation of Néel.

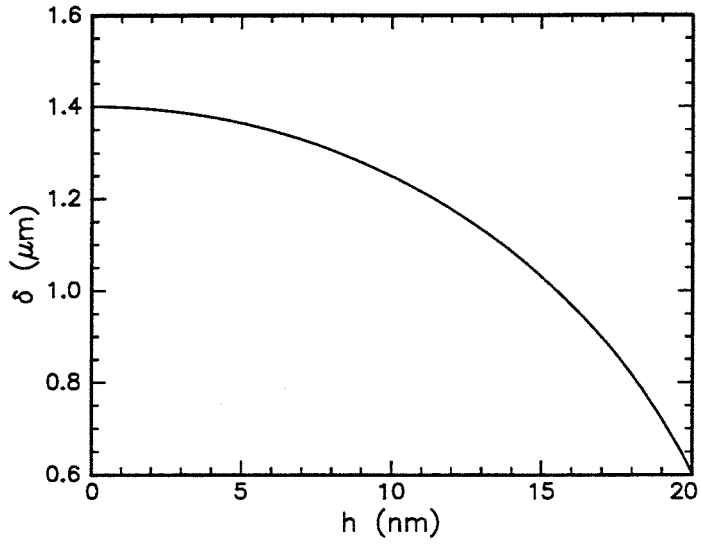

Figure B.2: Néel wall thickness vs. film thickness for $\leq$ 20.0 nm thick films.

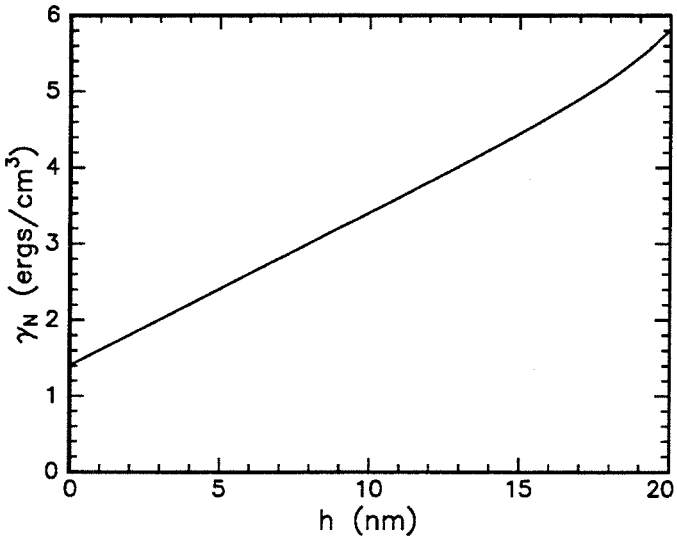

Figure B.3: Néel wall energy vs. film thickness for ≤ 20.0 nm thick films.

Bibliography

[1] L. Néel, J. Phys. Radium **17**, 250 (1956).

[2] B.D. Cullity, *Introduction to Magnetic Materials*, (Addison-Wesley, Philippines, 1972), Ch.2.

[3] S. Middelhoek, Ph.D. Thesis, Amsterdam, 1961.